Strongly Correlated Electrons at High Pressure:An Approach by Inelastic X-ray Scattering

Jean-Pascal Rueff

Université Pierre et Marie Curie - Paris 6

Habilitation à Diriger des Recherches

Spécialité : Sciences Physiques

Jean-Pascal Rueff

***Strongly Correlated Electrons at High Pressure**:*
An Approach by Inelastic X-ray Scattering.

Soutenue le 27 juin 2007 devant la commission d'examen

M. :	A.	Georges	Président
MM. :	G.	Lander	Rapporteurs
	J.-P.	Sanchez	
	L. H.	Tjeng	
MM. :	A.	Shukla	Examinateurs
	C. F.	Hague	

Contents

Part I

Mémoire

Chapter 1

Electronic behavior at high pressure

"It takes all the running you can do just to keep in the same place", Lewis Carroll

1.1 Introduction

1.1.1 Why this work

Pressure is an effective means to alter electronic density, and thereby the localization of electrons, their hybridization and their magnetic properties. Applying pressure therefore may lead to phenomena of importance from the physical point of view such as magnetic collapse, metal-insulator transitions (MIT), valence changes, or the emergence of superconducting phases.

Probing the electronic properties of materials under high pressure conditions, however, remains a formidable task, for the constrained sample environment prevents an easy access to the embedded material. With the exception of optical absorption which provides elements of information about low energy excitations, the experimental difficulties explain that high-pressure studies have been mostly restricted so far to structural refinement, to study of the Raman modes or to the characterization of transport properties.

The advent of extremely intense and focused x-ray sources which are the latest generation of synchrotrons has open new perspective for spectroscopic studies at high pressure. Nuclear forward scattering for instance, the Mössbauer synchrotron-based equivalent, is an excellent tool to investigate magnetism in selected elements. Inelastic x-ray scattering (IXS) and associated methods has turn out to be a powerful alternative for high-pressure physics. It is an all-photon technique fully compatible with high-pressure environments and applicable to a vast range of materials. In the resonant regime, its ensures that the electronic properties of the material under scrutiny is selectively observed. Standard focalization of x-ray in the range of 100 microns is typical of the sample size in the pressure cell. This also corresponds approximatively to the scattering volume in the hard x-ray region. In these conditions, we expect maximum throughput to be obtained using IXS-derived techniques.

Our main aim in this manuscript is to provide an overview of experimental results obtained by inelastic x-ray scattering under high pressure in two classes of materials which, arguably, have been at the origin of the renewal of "condensed matter" physics: strongly correlated transition metal oxides and rare-earth compounds. These materials are found in many technologically advanced products, such as in recording media based on GMR (Giant Magneto Resistance), spintronics or magnetic structures, and as such have been widely studied. Pressure, in line with other external parameters, can help to complete the

description of strong correlation, and better define the notion of electron localization.

Giving an extensive theoretical description of the d and f electrons goes far beyond the scope of this work. In particular, magnetic structure and interactions will not be discussed, except in close connection with the electronic properties. In the introduction, we restrict ourselves to useful concepts for understanding the nature of these electronic states, and more specifically their behavior under high pressure regime. Because it is a recent technique with which the reader might not be very familiar, theoretical and experimental basics of inelastic x-ray scattering will be discussed in some details in a second part. The last section is finally devoted to experimental results under high pressure, before conclusions are drawn.

1.1.2 Thermodynamics considerations

Exploring the phase (structural, magnetic or electronic) diagram of materials requires tuning some external key-parameters. Among them temperature and pressure are equally important to explore the landscape of the system free energy. A temperature (T) induced phase transition is driven by entropy. More simply, the temperature effects in terms of energy scale can be expressed by considering electronic excitations from the ground state via the Boltzman constant and the approximate relationship 1000 K $\cong$ 86.17 meV.

On the other hand, pressure-energy conversion can be obtained through the Gibbs free energy for a closed system, defined as $dG = -SdT + VdP$ with obvious notation. At constant temperature, the expression of the total energy change (for a given pressure variation ΔP) reduces to a simple integration of the VdP term. Although solid are not easily compressible, the volume variation at very high pressure regime, as envisaged in this study, is far from being negligible. Using the compressibility $\kappa = -1/V\,(\partial V/\partial P)_T$, one can estimate the energy variation from Eq. 1.1.

$$\Delta G = \frac{V_0}{\kappa}\left(1 - e^{-\kappa \Delta P}\right) \tag{1.1}$$

with V_0, the molar volume at ambient pressure. At low pressure, this expression can be approximated by $\Delta G \sim V_0 \Delta P$, which can be derived directly from the Gibbs free energy supposing V independent of P.

Let's estimate the internal energy change in a system for a ΔP of 100 GPa ($\equiv$ 1 Mbar) in the two classes of materials of main interest here: transition metals and rare earths. Transition metals are poorly compressible metals. Their isothermal bulk modulus ($K_T = 1/\kappa$) falls within the megabar range. Application of Eq. 1.1 to Fe ($K_T = 170$ GPa) yields a variation $\Delta G \sim 3.3$ eV for the considered ΔP. Rare earths on the contrary have lower K by about one order of magnitude. In Ce for instance ($K_T = 22$ GPa), it implies a far greater $\Delta G \sim 21.2$ eV for ΔP=100 GPa. The higher compressibility also means that rare-earth ions are more sensitive to smaller variation of pressure. Electronic transitions in rare-earth based materials are indeed usually observed at lower pressure compared to transition metal compounds.

Independently of the materials under consideration, T and P therefore probe the system free energy on totally different energy scales. Temperatures of several thousands K are commonly achievable with conventional heaters (such as resistive or laser-assisted setups), which nevertheless corresponds to a modest amount on an energy scale. At minimum, one order of magnitude is gained in energy using pressure as parameter since pressure apparatus permit application of megabars onto the sample. Pressure induced phase transition may also lead to new types of ordering, since entropy is not involved. The formation of a

quantum critical point (QCP) in strongly correlated materials is the manifestation of such a new state of matter.

1.2 Strongly correlated Transition metals

The general behavior of d electron indicates a delocalized character. In transition metal, they form a band of large width when compared to the other characteristic energy scales (cf. Fig. 1.1), which is located in the vicinity of the Fermi energy. Yet, many aspects of transition metals question this point of view. The localized or itinerant features of d electron has in fact been the subject of a long standing controversy, which originally goes back to Van Vleck and Slater's study of magnetism. An emblematic example of the apparent dual behavior of d electrons is Fe. The metallic character of Fe indicates itinerant d electron, while its magnetic properties are well described by an assembly of localized spins. Another striking contradiction appears in transition metal oxides, such as NiO, as revealed in the early work of de Boer and Verwey. NiO has a partially filled d band and should be metallic. Instead, NiO is a wide gap insulator, similarly to most of the transition metal oxides.

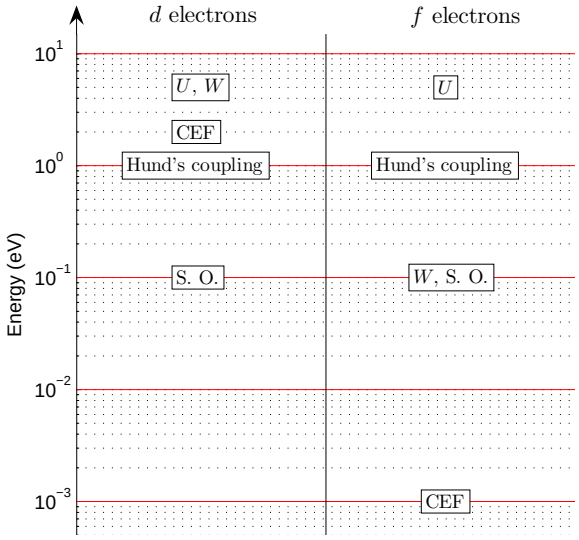

Figure 1.1: Schematic energy scale in $3d$ and $4f$-electron systems: S.O. is the spin orbit coupling, W the bandwidth, U the electron repulsion, CEF the crystal electric field.

1.2.1 Mott-Hubbard approach

In many transition metal materials, the Coulomb repulsion U between d electrons is of the same order of magnitude as the d bandwidth. The Mott-Hubbard Hamiltonian is a simplified, yet effective, approach for dealing with electron correlations. The correlated system is described by a single band model in which the d electrons experience a Coulomb U interaction when two of them occupy the same site. In the Mott Hubbard framework, the contribution of U is formalized as an extra term added to the kinetic energy t in the Hamiltonian:

$$\mathcal{H} = \sum_{i,j,\sigma} t_{ij} a^{+}_{i\sigma} a_{j\sigma} + U \sum_{i} n_{i\uparrow} n_{i\downarrow} \tag{1.2}$$

$a^+_{i\sigma}$ ($a_{i\sigma}$) creates (annihilates) an electron of spin σ at site i, and $n_{i\sigma} = a^+_{i\sigma}a_{i\sigma}$. In the strongly correlated picture, the relative magnitude of U and the d-bandwidth W governs the tendency toward localized ($U/W > 1$) or itinerant ($U/W < 1$) behavior of the d electrons. Correlations explain well the non-metallic character in transition metal materials: in the case of half filling or less, hopping of d electron through the lattice is energetically unfavorable because of the strong on-site Coulomb interaction, leading to the characteristic insulating state. This theoretical description was later extended by Zaanen, Sawatzky, and Allen (ZSA) [1] to account for large discrepancies observed between the estimated and measured band gap in some transition metal insulators and also explain their photoemission spectra. In addition to the on-site d-d Coulomb interaction U employed in the original Mott-Hubbard theory, the ligand-valence bandwidth, the ligand-to-metal charge-transfer energy (Δ), and the ligand-metal hybridization interaction are explicitly included as parameters in the model Hamiltonian. Systems where $U < \Delta$ are dubbed Mott insulators while $U > \Delta$ characterizes so-called charge-transfer insulators. In particular, it is now well established that though the U correlation energy is relatively high in NiO, the band gap is of the charge-transfer type that is primarily O-2p to Ni-3d character.

This classification scheme has been very successful in describing the diverse properties and some seemingly contradicting behavior of a large number of these compounds. However, these high-energy-scale charge fluctuations are primarily characteristic of the elements involved, and thus cannot be freely adjusted for systematic study of their effects, although they can be varied somewhat by external temperature and magnetic field. On the other hand, pressure can introduce much larger perturbations of these parameters than can either temperature or magnetic field. Hence, it is of great interest to study the high-pressure behavior of these systems, and specifically, to correlate observed transformations with changes in electronic structure.

1.2.2 Metal-insulator transition

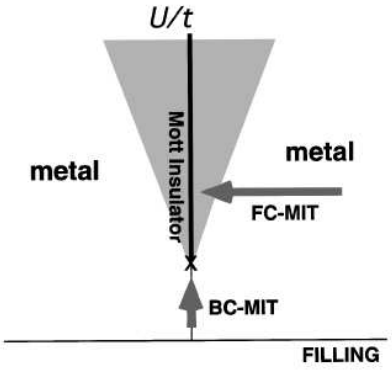

Figure 1.2: Metal-insulator transition in correlated transiton metal (from Imada et al. [2])

One important aspect of pressure-induced electronic changes are metal-insulator transitions. According to the categorization proposed by Imada et al. [2], pressure deals with bandwidth-control (BC) MIT as it affects the interatomic distances, hence the orbital overlap and the related bandwidth. In this picture, the control parameter U/t (or equivalently U/W) determines the transition from a Mott insulator to a metallic state. V_2O_3 is a prototypical example showing of BC-type insulator to metal transition by application of pressure. In correlated materials, the metallic state (gray area in Fig. 1.2) in the immediate

vicinity of the insulator state shows an anomalous behavior: the carrier are on the verge of localization, and the system is subject to strong spin, charge and orbital fluctuations. This is the case for example in V_2O_3 which is characterized by anomalous specific heat and susceptibility near the MIT region.

The strength of resonant spectroscopy lies in its ability to decouple these different degrees of freedom while applying pressure. The change in the charge transfer and electronic correlations through the MIT will be more specifically discussed in sections 3.2.2 in two model compounds, NiO and CoO.

1.2.3 Magnetic collapse

In his pioneering work, N. Mott pointed out the tight relationship between the insulating state of transition-metal compounds and electronic density [3]. In Mott's picture, the insulating character persists upon increasing density (i.e. pressure) until screening becomes effective enough to destroy the electronic correlation that maintains the insulating state, while the d-bandwidth increases due to the growing band overlap. At high pressure, the system is therefore expected to undergo a first-order insulator-metal transition, which is usually accompanied by the disappearance of the local d magnetic moment (and not only the long-range magnetization). The itinerant character of the d electrons for magnetism is formalized by the Stoner criterion. The stability of the magnetic state is expressed by the balance between exchange and kinetic energies, according to $I \times n(\varepsilon_F) > 1$, where I is the Stoner integral and $n(\varepsilon_F)$ the density of the states at the Fermi energy. As the d bandwidth increases, $n(\varepsilon_F)$ decreases, eventually leading to a state where the Stoner criterion is no longer fulfilled. Here, this *magnetic collapse* is understood as a direct consequence of the progressive delocalization of the d electrons under pressure.

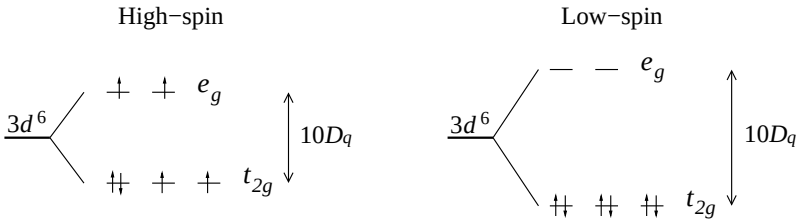

Figure 1.3: Example of high-spin ($S = 2$) and low spin ($S = 0$) configurations for a $3d^6$ metal ion in octahedral symmetry. $10D_q$ is the crystal field strength.

Magnetic collapse can be more simply sketched within an atomic picture. The atomic picture is mostly useful when discussing spectroscopic data in transition metals. Let's consider for instance a transition-metal ion sitting in an octahedral site. Because the crystal field strength is larger than the spin-orbit coupling, the d band splits into two subbands, t_{2g} and e_g, of sixfold and fourfold degeneracy respectively (cf. Fig. 1.3 for a $3d^6$ ion). At ambient conditions, the d band is spin polarized and the majority and minority band are split by the exchange interaction J. When pressure is applied, the crystal field strength increases as a result of the metal-ligand distance shortening. In contrast, the intra-atomic exchange J is barely affected. At a given pressure, the crystal field strength $10Dq$ will overcome the magnetic exchange interaction, resulting in a high spin (HS) to low spin (LS) transition. In this simplistic picture, the magnetic collapse therefore results from a competition between the crystal field and magnetism (exchange interaction), while it stems rather from the interplay between the d-d Coulomb interaction U and d-bandwidth

W in the strongly correlated electron scheme.

Pressure-induced magnetic collapse in transition-metal oxides as well as the relative influence of crystal field vs. bandwidth will be discussed in section 3.2.

1.3 Hybridized f states

Contrary to d levels, the $4f$ electrons in the solid are considered as localized, rather unaffected by the proximity of the conduction band. Under pressure, the conduction bandwidth and Fermi energy will change eventually modifying the f-electronic behavior: The crystal structures is driven from high-symmetry structures to low-symmetry phases. In rare earth and actinides, such structural changes are often correlated to a sudden contraction of the lattice leading to volume collapse transitions (VCT) [4]. The magnetic susceptibility evolves from Curie-Weiss behavior to a Pauli-like paramagnetism, suggesting loss of the moments such as in Ce. The black to golden phase transition in SmS is another startling illustration of pressure-induced metallization in f-systems. Even so, because the Hund's coupling energy is much larger than the f bandwidth, the f electrons are suspected to retain their localized character to a large extent, hybridization being considered a second-order perturbation. Similarly, it is largely admitted that the VCT in mixed valent rare earth is mostly caused by the a pressure-induced change of occupation of the f and d bands. But the general consent is that only a minute fraction of the f electrons delocalizes to hybridize with the conduction band, while the other part can still be considered as well localized. A situation at odds with d electron behavior where the bandwidth is orders of magnitude larger than in hybridized f electrons (cf. Fig. 1.1).

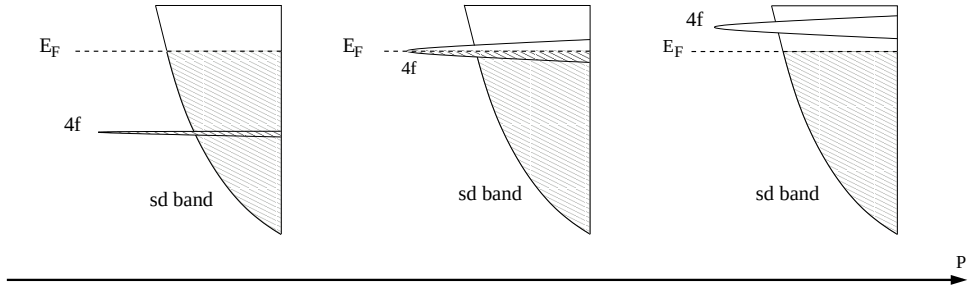

Figure 1.4: Schematic change of the f-state with pressure in elemental rare-earth.

In the 70's, Johansson and Rosengren [5] modeled the electronic changes of rare earth under pressure in the more general context of the intermediate valency. The physical picture is that the $4f$ energy (ε_f) comes closer to the Fermi energy (E_F) as P increases (cf. Fig. 1.4) until $\varepsilon_f \approx E_F$. At this point, the $4f$ level progressively empties in the conduction band. At still higher pressure, the empty $4f$ band (now located above the Fermi level) denotes the transition to a new valent state. Considering a linear variation $\Delta E(P)$ of the energy distance between ε_f and E_F,

$$\lim_{P \to 0} \frac{d\Delta E(P)}{dP} = \mathcal{V}_{n+1} - \mathcal{V}_n \tag{1.3}$$

with $\mathcal{V}_n$ the atomic volume of the $|4f^n\rangle$ configuration, Johansson was able to predict the valence transition pressures in rare earth. Thus, the stability of one valency over the other is seen to result from the balance between the gain in cohesive energy and the energy price to promote an f electron into the conduction band. However, the latter process is

poorly taken into account in the model. The description of a hybridized f-state is in fact a formidable task, which lies at the core of modern treatment of f electrons, involving the formation of a Kondo singlet state or the heavy fermion (HF) behavior, two most challenging aspects of the f mixed valent state (cf. Ref. [6] for a review). Both Kondo and HF phenomena deal with low temperature physics on an energy scale far different from that envisaged in this review. Yet, the competition between the localized and delocalized tendency, Kondo screening and Fermi liquid behavior can be tuned effectively by applying pressure.

1.3.1 Mixed valency

It is convenient to treat the hybridized f state as a mixed (or fluctuating) valent state, the f electron acquiring part of the conduction electrons character. Hybridization or mixed-valency may be defined formally in terms of configuration interaction. Then, the ground state is written as a linear combination $c_{n-1}\left|f^{n-1}v^{m+1}\right\rangle + c_n\left|f^n v^m\right\rangle + \cdots$ of degenerated states (v stands for the valence electrons) with a probability $|c_i|^2$ [7]. The degeneracy is lifted in presence of a core-hole, such as in intermediate or final state of IXS.

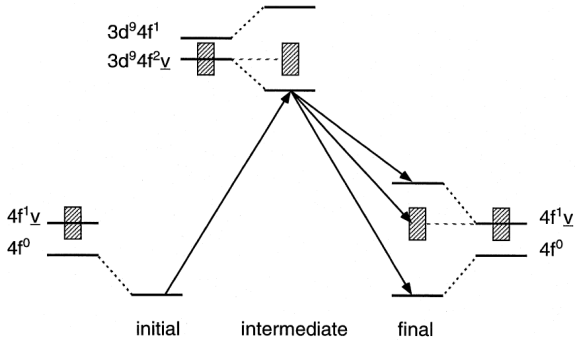

Figure 1.5: Total energy level scheme of the Ce in initial, intermediate and final state of IXS in CeO_2 (from Kotani [8])

Large fluctuations are excluded due to the strong Coulomb repulsion, but the f valency may vary around the ground state value at a characteristic timescale determined by the f bandwidth [9, 10]. In the case of the f systems with a narrow bandwidth, fluctuations are slower than typical core-hole lifetimes in x-ray spectroscopy. Hence, mixing of configuration can be in principle resolved by such techniques. Section 3.3 is mainly devoted to exploring this aspect.

1.3.2 Anderson Impurity Model

The hybridization of a single f level with band states is well described by the Anderson impurity model (AIM). The Anderson Hamiltonian applies to the case of a single magnetic impurity of energy ε_f weakly interacting with conduction electrons, described by the dispersion $\varepsilon(k)$. The AIM is related to the Hubbard Hamiltonian in Eq. 1.2 in that it also accounts for correlations between the f electron by an on-site Coulomb parameter U.

$$\begin{aligned}\mathcal{H} &= \sum_{km}\varepsilon(k)c^+_{km}c_{km} + \varepsilon_f\sum_m \hat{f}^+_m\hat{f}_m \\ &+ \sum_{km}V(k)(\hat{f}^+_m c_{km} + c^+_{km}\hat{f}_m) + \frac{U}{2}\sum_{m\neq m'} n^f_m n^f_{m'} + \mathcal{H}_0 \end{aligned} \tag{1.4}$$

$\mathcal{H}_0$ represents the conduction electrons term which do not couple to the impurity; $\hat{f}_m^+$ creates an electron f with a magnetic quantum number m from an previously empty site. The hybridization strength is given by V. At $V \neq 0$, the ground state is a singlet Kondo state ($S = 0$). In first approximation, U is usually taken in the limit $U \to \infty$, which implies that double occupancy configuration is not allowed.

The AIM framework grasps the most important concepts of hybridized f electrons such as the stabilization of singlet ground state and the building-up of the Abrikosov-Suhl resonance which a characteristic of the Kondo excited states. A more accurate treatment would include f-electrons correlation and their hybridization with an electron bath from self-consistent band structure approach [11]. The influence of pressure can be clearly seen when one expresses the energy gain $\Delta\varepsilon$ due to the formation of the singlet state [12]:

$$\Delta\varepsilon = -D\mathrm{e}^{-|\varepsilon_f|/(\nu_f N(0) V^2)} \tag{1.5}$$

D is the half bandwidth of the conduction band, V the hybridization strength, ν_f the f-orbital degeneracy and N(0) the conduction electron density of states (per spin). This energy is usually associated to a characteristic temperature T_K. V is known to be strongly pressure dependent because the band overlap is reinforced when the unit cell is reduced. As in the γ-α transition in Ce, the Kondo state is favored at high pressure. Similarly, T_K is expected to increase with pressure as hybridization becomes stronger. This is indeed the case in Ce but not in Yb which shows the opposite behavior. The difference between electron-type (Ce) and hole-type (Yb) Kondo temperature has been explained by the influence of two competing and contradictory effects under pressure: increase of hybridization and suppression of valency fluctuation [13]. We will come back to this issue in section 3.3.

Another important parameter which is derived from the generalized AIM Hamiltonian is the f-occupancy n_f and double occupancy. In the case of strong coupling V, i.e. at high T_K, n_f significantly deviates from unity, while the double occupancy is expected to increase [14]. In the Kondo regime, a proportion $1 - n_f$ of the f electrons are delocalized. Having an experimental access to the f-occupancy and following its evolution when pressure is applied is therefore crucial for a proper description of the f hybridized state. This will be the main object of section 3.3.2.

1.3.3 Actinides case

Due to the hierarchy between crystal field and spin-orbit interactions, the $5f$ states in actinides are considered as intermediate between $4f$ and $3d$ electrons in terms of electron localization [15, 16]. Thus, in the early actinides (Th–Np), the pressure-induced decrease of the atomic volume is well described by normal band structure calculations pointing to an itinerant behavior of the f electrons. From Am onwards, the $5f$ starts to localized at ambient conditions, while Pu seems to lie at the borderline of localization-delocalizaton: f states show an itinerant character in the numerous phases of Pu, while in δ-Pu the f states are close to localization.

In the U-compounds, which will be more specifically discussed in section 3.3.3.1, the $5f$ electron bandwidth is of the same order of magnitude as the spin-orbit energy and the on-site Coulomb interaction, and all these parameters must be taken into account on the same footing. The $5f$ electronic behavior in U is then expected to be highly sensitive to modification of these interactions when pressure increases, and simplistic treatment of the f electron as band states is no longer valid. Similarly, in Am under pressure the $5f$ electrons were shown to delocalize in a Mott sense, and a proper treatment means correlations must be included [17].

Chapter 2

An introduction to IXS

"There are only three basic actions to produce all the phenomena associated with light and electrons: A photon goes from place to place, an electron goes from place to place, an electron emits or absorbs a photon.", Richard Feyman

2.1 Basics of inelastic x-ray scattering

2.1.1 A question of terminology

Properly naming new spectroscopic techniques is far from trivial for it can help neophytes to identify the nature of the underlying process and replace it in its historical context. As many recent spectroscopies that is not attached to one outstanding contributor, the terminology for inelastic x-ray scattering (IXS) has gone through a maze of mutations.

Sparks [18] first evidenced the "inelastic resonance emission of x rays" using a lab-top x-ray source. The new experimental finding, here correctly designated as an emission process in the resonant conditions, differs from early results obtained in the Compton regime for which the photon energy is chosen far from any resonances, and at high momentum transfer. The interest of synchrotron radiation for inelastic x-ray scattering was emphasized a few years later by Eisenberger et al. [19] who first performed "resonant x-ray Raman scattering" at the Cu K-edge, and simultaneously adopted Raman terminology for an x-ray based process. Though historically justified, this widespread terminology is somewhat confusing. In this work, we will limit ourselves to the use of *resonant inelastic x-ray scattering* (RIXS). An exception will be made for *resonant x-ray emission spectroscopy* (RXES) or *x-ray emission spectroscopy* (XES) as a sub-category of RIXS, when it clearly applies.

The non-resonant case of IXS (nrIXS)[1] has followed a different thread. Non-resonant experiments of DuMond and coworkers on "x-ray Compton scattering" precede resonant measurements by several decades. This was pursued by pioneer work of M. Cooper and W. Schülke with x-ray rotating anodes and later synchrotron light (cf. Refs. in Schülke [20]). Susuki [21] later measured the K-edge of Be using "X-ray Raman scattering" (XRS) by extending the energy loss region away from the Compton region. A terminology still in use to distinguish the measurements of the absorption spectra of light element in the x-ray energy loss spectra from that of other type of non-resonant scattering events, such as coupling to phonon modes.

[1] The acronym for non-resonant inelastic scattering (nrIXS) has not to be confused with that of nuclear resonant inelastic x-ray scattering

Finally, *inelastic x-ray scattering* (IXS) denotes the general scattering process from which both RIXS and nrIXS originate.

2.1.2 IXS cross section

The general inelastic x-ray scattering process is illustrated in Fig. 2.1. An incident photon defined by its wave vector, energy and polarization ($\mathbf{k_1}$, ω_1, $\boldsymbol{\epsilon}_1$) is scattered by the system, and a second photon ($\mathbf{k_2}$, ω_2, $\boldsymbol{\epsilon}_2$) is emitted. $\mathbf{q} = \mathbf{k_1} - \mathbf{k_2}$ and $\omega = \omega_1 - \omega_2$ represent the momentum and energy respectively transfered during the scattering process. For x-rays, $k_1 \approx k_2 = k$, and $q = 2k\sin(\theta)$.

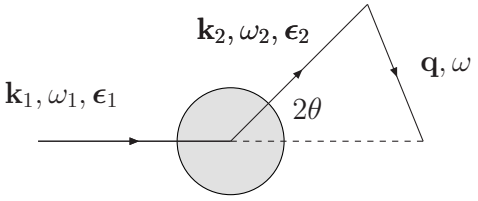

Figure 2.1: Scattering process of a photon

The starting point for describing the scattering process theoretically is the interaction Hamiltonian between the incident electromagnetic field described by its potential vector $\mathbf{A}$ and the electrons of momentum $\mathbf{p}$. In the Coulomb gauge ($\nabla\mathbf{A} = 0$), it can be written as:

$$\mathcal{H} = \sum_i \frac{\alpha^2}{2}\mathbf{A_i}^2 + \alpha(\mathbf{p_i} \cdot \mathbf{A_i}) \tag{2.1}$$

where α is the fine structure constant and the sum is over all the electrons of the system. We have dropped the spin-dependent term.

The scattering cross section derived from the interaction Hamiltonian in the sudden approximation is known as the Kramers-Heisenberg equation [22]. It consists of the sum of three terms, represented as a Feynman diagram in Fig 2.2, which are discussed below.

2.1.2.1 Non-resonant scattering

The first term (Fig 2.2(a)) arises from the $\mathbf{A}^2$ term in the interaction Hamiltonian in first order of perturbation. Far from any resonances, the scattering cross section depends on the dynamical structure factor $S(\mathbf{q}, \omega)$ according to:

$$\frac{d^2\sigma}{d\Omega d\omega_2} = \frac{\omega_2}{\omega_1}\left(\frac{e^2}{mc^2}\right)^2 (\boldsymbol{\epsilon}_1 \cdot \boldsymbol{\epsilon}_2)^2 S(\mathbf{q}, \omega), \tag{2.2}$$

using the notation of Fig. 2.1. The pre-factor is equivalent to the Thomson scattering by free electrons. The dynamical structure factor reflects the system properties in absence of perturbation by the probe (fluctuation-dissipation theorem). Following Van Hove [23], $S(\mathbf{q}, \omega)$ can be written as the Fourier transform of electron pair correlation function.

$$S(\mathbf{q}, \omega) = \frac{1}{2\pi}\int dt\, \exp(-i\omega t)\left\langle g \left| \sum_{jj'} \exp(-i\mathbf{q} \cdot \mathbf{r}_{j'}(t)) \exp(i\mathbf{q} \cdot \mathbf{r}_j(0)) \right| g \right\rangle \tag{2.3}$$

where $|g\rangle$ is the ground state and the sum is carried over the position $(r_j, r_{j'})$ of the electron pairs. Depending on how q compares with characteristic length scale of the system λ_c,

equation 2.3 describes phenomena ranging from the dynamics of collective modes ($q\lambda_c \ll 1$) to single particle excitations ($q\lambda_c \gg 1$) can be examined. It is also useful to relate $S(\mathbf{q},\omega)$ to the dielectric function ϵ through

$$S(\mathbf{q},\omega) = \frac{q^2}{4\pi e^2} Im\left[\frac{1}{\epsilon(\mathbf{q},\omega)}\right], \tag{2.4}$$

This equation is similar to the electron energy loss spectroscopy (EELS) cross section providing that the pre-factor is replaced with an appropriate cross section for electron-electron scattering. Compared to EELS or neutron scattering, nrIXS can probe a wider domain in the ($\mathbf{q}$,ω) phase space because of the higher photon energy, and the absence of kinematic limitations which allows $\mathbf{q}$ to vary independently of ω. The energy transfer is limited by the best achievable energy resolution.

2.1.2.2 Resonant scattering

The non-resonant contribution to scattering cross section can normally be neglected when the incident photon energy is tuned in the vicinity of an absorption edge. In such a case, the $\mathbf{p}\cdot\mathbf{A}$ interaction dominates (Fig 2.2(b)). In the second order, this term describes the scattering process where the incident photon is absorbed and a secondary photon is emitted as illustrated in Fig. 2.3(a). In the resonant regime, the absorption and emission events interfere, and cannot be treated separately. The resonant denominator and interference term in the corresponding cross section (Eq. 2.5) characterize the regime of resonant inelastic x-ray scattering (RIXS).

$$\frac{d^2\sigma}{d\Omega d\hbar\omega_2} = \frac{\omega_1}{\omega_2}\sum_f \left| \sum_i \frac{\left\langle f \left| D^{(L)} \right| i \right\rangle \left\langle i \left| D^{(L')} \right| g \right\rangle}{E_g + \hbar\omega_1 - E_i + i\Gamma_i/2} \right|^2 \times \delta(E_f - \hbar\omega_2 - E_g - \hbar\omega_1), \tag{2.5}$$

where $|g\rangle$, $|f\rangle$ and $|i\rangle$ stand for the ground state, final state, and intermediate state and $D^{(L)}$ are electric 2^L-pole transition operators. Γ_i is lifetime broadening of the core-excited state. Energy conservation is reflected by the argument of the δ-function in Eq. 2.5. This gives rise to the so-called Raman shift of the scattered photon energy $\hbar\omega_2$, which varies linearly as a function of the incident photon energy.

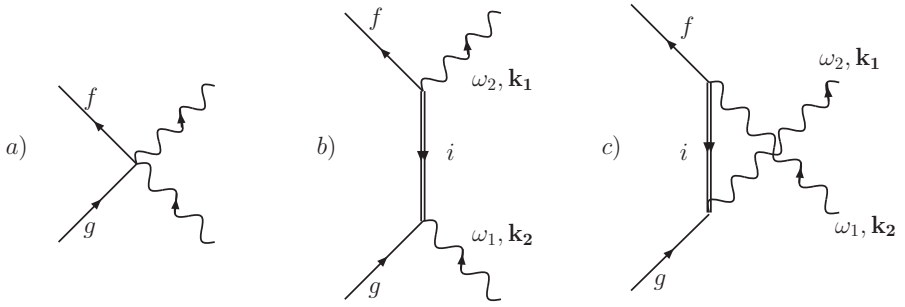

Figure 2.2: Terms in the IXS cross section : a) non-resonant, b) and c) resonant scattering. Wavy (straight) lines represent the photon (electron) wave functions; double lines are inner-shell core-hole.

Because of the finite lifetime in the final state Γ_f, the δ-function in Eq. 2.5 has to be replaced by a Lorentzian $\Delta(\omega) = \Gamma_f/(\omega^2 + \Gamma_f^2)$. This in turn plays a fundamental role in the formation of the RIXS profile [24] (cf. 2.1.3). Other correction terms would include convolution by Gaussian functions to account for the experimental resolution and incident energy bandwidth.

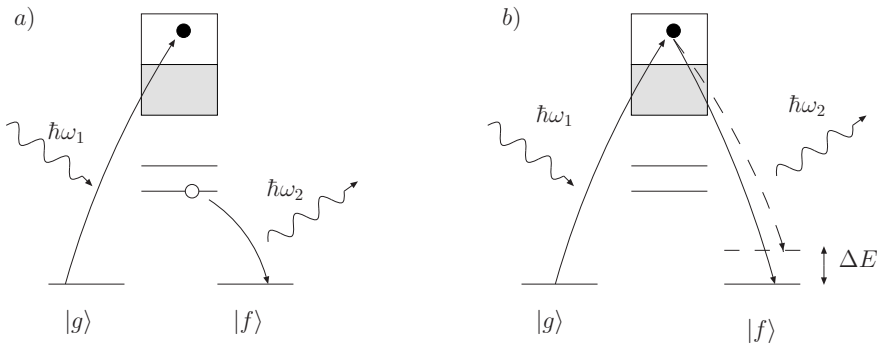

Figure 2.3: One electron picture of two types of RIXS process : resonant emission (a), and direct recombination (b). Shaded area are occupied states. ΔE stands for the energy of one particular excited state relatively to the ground state.

2.1.2.3 Direct recombination

Of particular interest is the RIXS process involving the decay of the participant electron (cf. Fig. 2.3(b)) in the final state. The scattered photons then have either the same energy as the incident photon, producing a quasi-elastic line, or can leave the system with an energy loss ΔE that is transfered to the electrons. In this direct recombination process, the system is left in the final state with no core-hole present and low energy excitations can be probed similarly to EELS or optical absorption but with several advantages compared to the latter: i) the momentum transfer can be varied on a larger scale and the dispersion of the excitation studied over multiple Brillouin zones; ii) the scattering cross section benefits from the resonant enhancement including the chemical selectivity.

2.1.2.4 Fluorescence

Far above the absorption edge, the resonant processes still prevails but coherence between the absorption and emission is lost. It is no longer possible to determine when the photon is absorbed or emitted. Time-permuted events such as described by diagram Fig 2.2(c) can exist. This situation corresponds to the fluorescence regime or x-ray emission spectroscopy (XES), where the emitted photon energy no longer depends on the choice of the energy of the incident photon. The fluorescence cross-section is well approximated by using a two-step model (absorption followed by emission) by multiplying the x-ray-absorption cross section with the emission cross section.

In the case of the Kα and Kβ XES, the absorption process only contributes to the emission spectrum as a proportionality factor. This approach is limited for ionic systems, where configuration interactions in the intermediate state can be neglected. For covalent systems, a coherent second-order model gives a more accurate description when relaxation in the intermediate state can occur.

2.1.3 Narrowing effects

In the resonant regime, the overall lifetime Γ broadening effect can be partly overcome, depending on the detuning $\delta\omega$ of the incident photon energy ω with respect to the resonance energy. Such a narrowing effect was first observed at the Cu K edge [26].

For clarity, we distinguish between RIXS processes where a core-hole is left in the final state from those which involve direct recombination. The former process can be simply

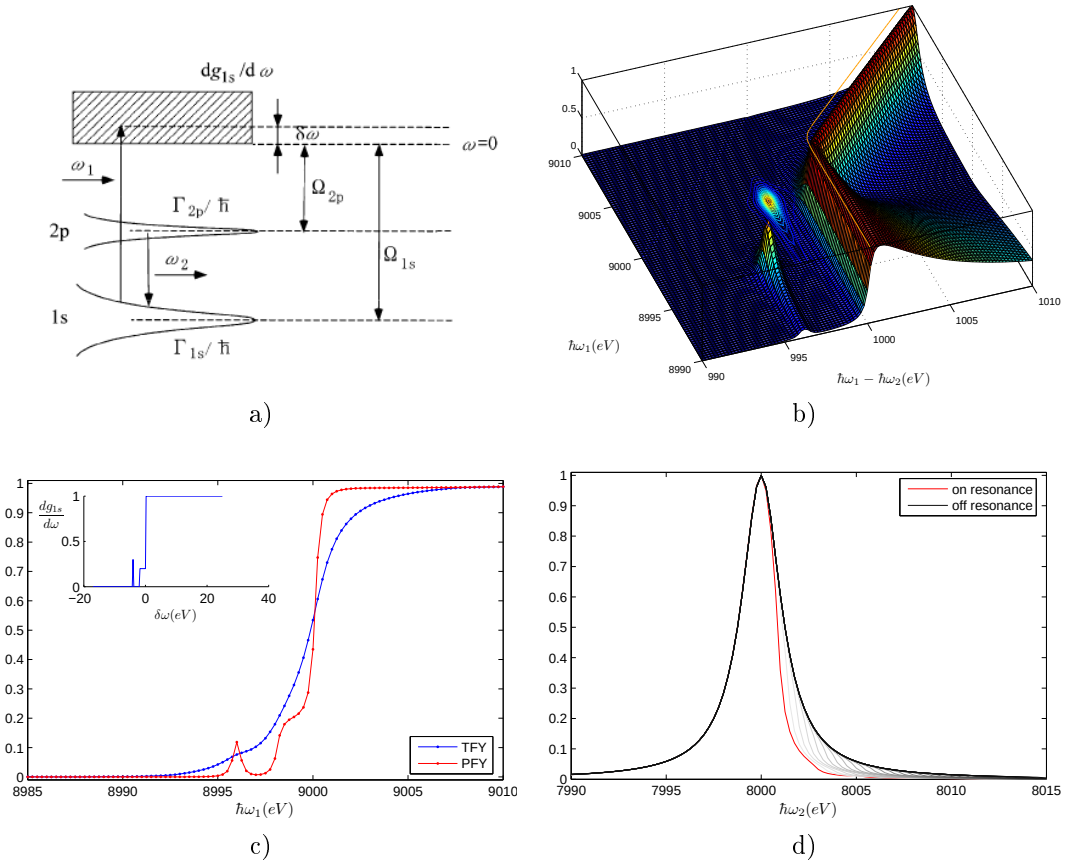

Figure 2.4: Narrowing effects for $1s2p$-RIXS. (a) RIXS process in a one-electron picture (from Hayashi et al. [25]); (b) map of the cross section in the incident vs. transfer energy plane; (c) Partial and total fluorescence yield absorption spectra - inset indicates the model density of unoccupied states; (d) Comparison of RXES spectra on resonance to fluorescence regime (off resonance).

viewed as the resonant emission of a photon. In the following, the associated technique is called resonant emission spectroscopy (RXES).

2.1.3.1 Resonant X-ray emission

To illustrate the narrowing effects, we take the example of a $1s2p$-RXES. In this process (Fig. 2.4(a)), a incident photon of energy $\hbar\omega_1$ provokes the transition of a $1s$ electron primarily to states of p-symmetry. The decay of the atom occurs via the transition of a $2p$ electron back to $1s$ level. The cross section then reads as Eq. 2.6 with notations defined in Fig. 2.4(a). The sum over discrete intermediate states in Eq. 2.5 has been substituted by integration over a continuous density of unoccupied states, represented by the function $dg_{1s}/d\omega$ [27].

$$\frac{d\sigma(\omega_1)}{d\omega_2} \propto \int \frac{(\omega_2/\omega_1)(\Omega_{1s}+\delta\omega)(dg_{1s}/d\omega)}{((\Omega_{1s}+\delta\omega-\omega_1)^2+\Gamma_{1s}^2/4\hbar^2)\left((\Omega_{2p}+\delta\omega-(\omega_1-\omega_2))^2+\Gamma_{2p}^2/4\hbar^2\right)} d\omega \tag{2.6}$$

We use Eq. 2.6 to simulate the $1s2p$-RXES process with the following parameters: Ω_{1s} =9000 eV, Ω_{2p} =1000 eV, Γ_{1s} =2 eV, Γ_{2p} =0.5 eV. We choose a model empty density of states, shown in the inset to Fig. 2.4(b), represented by a step function centered at

Γ_{1s} with some structure at the bottom edge. We have also introduced in pre-edge region, a sharp non-zero density of states which could be associated to localized $3d$ states. The results of the RXES process is shown in Fig. 2.4(b) as a function of incident and transfer energy. In this plane, emission from localized states appears at constant transfer energy, while fluorescence emission disperses along the main diagonal. Cuts of this surface at fixed $\hbar\omega_1$ probe the final states with a Γ_{2p} resolution. In the opposite direction, at fixed transfer energy, one is able to scan through the intermediate state with a resolution given by Γ_{1s}. The differential resolving power is clearly observed in the pre-edge feature, which stretches further in the direction parallel to incident energy axis (cf. Fig. 2.4(b), contour plot). At the resonance, a narrowing of the emission below the lifetime broadening is observed (Fig. 2.4(d)) as expected from the above arguments.

2.1.3.2 Partial Fluorescence Yield X-ray absorption

Instead of measuring the emitted spectra at fixed incident energy as in RXES, it might be useful to follow the scattered intensity at fixed emission energy while the incident energy is varied across an absorption edge. This corresponds to cuts along the diagonal in Fig. 2.4(b). In such case, x-ray absorption spectra are obtained with an improved resolution [28]. The sharpening effect results from the absence of a deep core-hole in the final state. As opposed to measurements in the total fluorescence yield (TFY) mode however, partial fluorescence yield (PFY) spectra are not strictly equivalent to conventional absorption [29], since it depends on the choice of the emitted energy. In this case, the lifetime broadening is given by :

$$\frac{1}{\Gamma_{PFY}^2} = \frac{1}{\Gamma_i^2} + \frac{1}{\Gamma_f^2} \tag{2.7}$$

As a rule of thumb, the lifetime broadening of the final state is considerably smaller than that of core excited state ($\Gamma_f \ll \Gamma_i$), which gives the possibility of performing x-ray absorption spectroscopy below the natural width of the core excited state. The sharpening effect in the case of the $1s2p$ process is exemplified in Fig. 2.4(b) where PFY and TFY spectra calculated from Eq. 2.6 are superimposed and compared to the model density of states.

2.1.4 Third-order terms

The core hole left in the RIXS intermediate state can be considered to form a virtual excitonic pair with the excited electron (cf. Fig. 2.5(a)). The Coulomb interaction of this short-lived exciton then acts as an extra potential which may scatter off valence electrons. The occurrence of such a shake up event supposes that the intermediate state is long enough (failure of the sudden approximation) and requires an ad-hoc treatment beyond the Kramers-Heisenberg formulation. Shake up process is correctly described by a third order perturbation treatment of the scattering cross section [30, 31]. In the shake up description, the RIXS cross section is explicitly related to the dynamical structure factor $S(\mathbf{q},\omega)$, weighted by a resonant denominator [32, 33]. Although in most case it is not necessary to resort to such an extreme, it was suggested that third order corrections could explain the deviation from linear Raman shift observed in cuprates.

2.2 Instrumental integration

IXS is a second order process of weak intensity. If the very first experiments were performed on second generation sources, the true take-off of IXS as a spectroscopic probe coincides

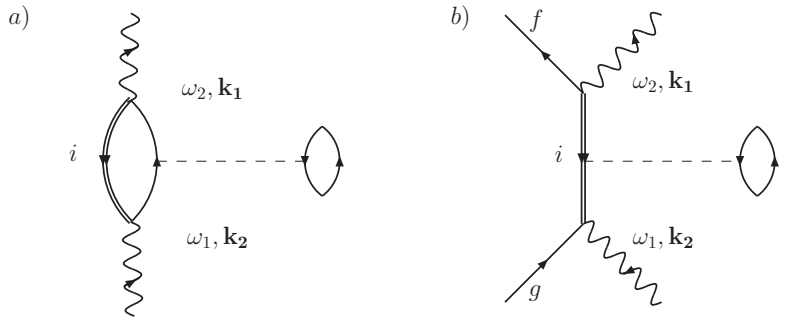

Figure 2.5: First order Coulomb corrections (dotted line) to RIXS. In diagram a), an excitonic pair is formed in the intermediate state.

with the development of insertion devices on third generation synchrotron. Simultaneously, new x-ray optics based on the Rowland circle geometry has provided relatively large acceptance angle while maintaining an excellent energy-resolution.

2.2.1 IXS Spectrometer

2.2.1.1 Energy selection

The selection of the emitted photon energy is realized by Bragg reflection on a crystal analyzer. Because perfect crystal quality is required to attain the best resolving power, Si or Ge analyzer are preferentially used. Another key point is to adapt the Bragg angle to the photon energy in order to minimize the geometrical contribution to the resolution. This quantity is given by equation 2.8 where $\Delta\theta$ is the source size (including the beam divergence) and θ_B the Bragg angle of a given reflection. Thus, the higher the Bragg angle, the smaller the geometrical term.

$$\left.\frac{\Delta E}{E}\right|_g = \Delta\theta \cot\theta_B \tag{2.8}$$

Typical analyzers are indicated in Table 2.1 for selected transition metals, rare earths and actinides emission energies.

Emission Line	Energy (eV)	Analyzer	Bragg angle (deg)
Mn-Kα_1	5900.4	Si(440)	71.40°
Fe-Kα_1	6405.2	Si(333)	67.82°
Mn-K$\beta_{1,3}$	6490.4	Si(440)	84.10°
Co-Kα_1	6930.9	Si(531)	76.99°
Fe-K$\beta_{1,3}$	7059.3	Si(531)	73.06°
Ni-Kα_1	7480.3	Si(620)	74.82°
Co-K$\beta_{1,3}$	7649.1	Si(620)	70.70°
Cu-Kα_1	8046.3	Si(444)	79.38°
Ni-K$\beta_{1,3}$	8264.6	Si(551)	80.4°
Cu-K$\beta_{1,3}$	8903.9	Si(553)	79.97°
Ce-Lα_1	4840.2	Si(400)	70.62°
Yb-Lα_1	7416.0	Si(620)	76.78°
U-Lα_1	13614.7	Ge(777)	77.40°

Table 2.1: Analyzer crystals and Bragg angles sorted by increasing emission energies for selected transition metals, rare-earths and actinides.

2.2.1.2 Rowland circle

IXS has largely benefited from the technological developments concerning x-ray spectrometers. One of the major step towards high resolution - high flux spectrometer was to adapt the Rowland circle in the Johann's geometry to x-ray optics. In this geometry, the sample, the analyzer and the detector sit on a circle which diameter corresponds to the analyzer bending radius R. The Johann geometry departs from the exact focusing or Johansson's geometry by a different curvature of the analyzer surface, as illustrated in figure 2.6. In the latter, the analyzer surface entirely matches the Rowland circle, while in the former the focusing condition is only fulfilled at a single point.

Machining the analyzer surface to the Johansson's condition is a difficult task, and the Johann geometry is usually preferred. The consequent Johann error can be expressed by equation 2.9, where r is the distance from the analyzer center. This contribution to the overall resolution is negligible as long as the analyzer diameter is small compared to the bending radius.

$$\left.\frac{\Delta E}{E}\right|_J = \frac{1}{2}\left(\frac{r}{R}\right)^2 \cot^2\theta_B \tag{2.9}$$

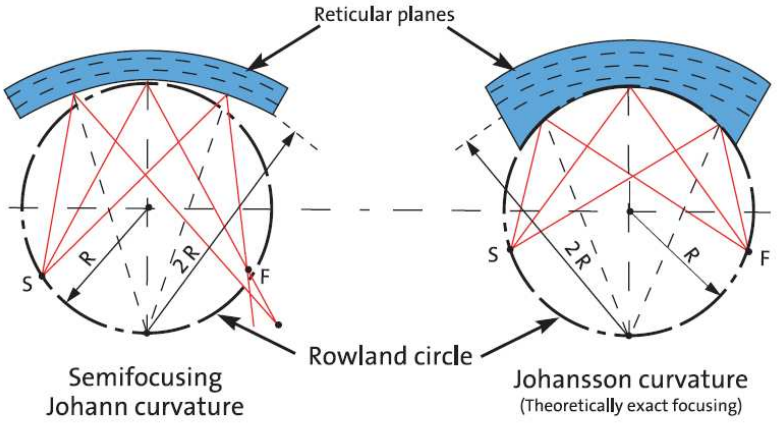

Figure 2.6: Johann geometry is an approximation of the Johanssonn geometry for large ΔE.

2.2.1.3 Analyzer bending

The analyzer is the spectrometer masterpiece. It serves both to select the emitted photons energy and to focus the beam onto the detector. Among many different focusing setups, we privilege herein spherically bent analyzers for they combines wide solid-angles and high-resolution capabilities. Static bending can be realized by pressing the analyzer wafers onto a spherical glass substrate. The two pieces are bonded together either by gluing the analyzer backface with a resin, or by anodic-bonding method which was recently applied to the fabrication of Si analyzer [34]. In this technique, bonding is ensured by migration of Na^+ ions in the glass at high temperature and in a presence of a high electric field. Excess of O^{2-} ions forms at the glass/Si interface which ultimately leads to the formation of Si-O bonds. Figure 2.7 shows a press developed for anodic bonding at IMPMC (Paris).

Bending a crystal results in elastic deformations that affect the energy resolution according to

$$\left.\frac{\Delta E}{E}\right|_P = \frac{l}{R}\left|\cot^2(\theta_B) - \nu\right| \tag{2.10}$$

where l is the effective thickness of the crystal and ν the material Poisson ratio. This term is normally small, but a conventional gluing process may introduce extra strain that further contributes to enlarge the energy bandwidth. Because of the absence of interfacial gluing resin, the anodic bonding technique has provided the best resolving power so far. An intrinsic resolution of the order of 200 meV was obtained at 8.979 keV with a 2-m radius Si(553) analyzer prepared at IMPMC.

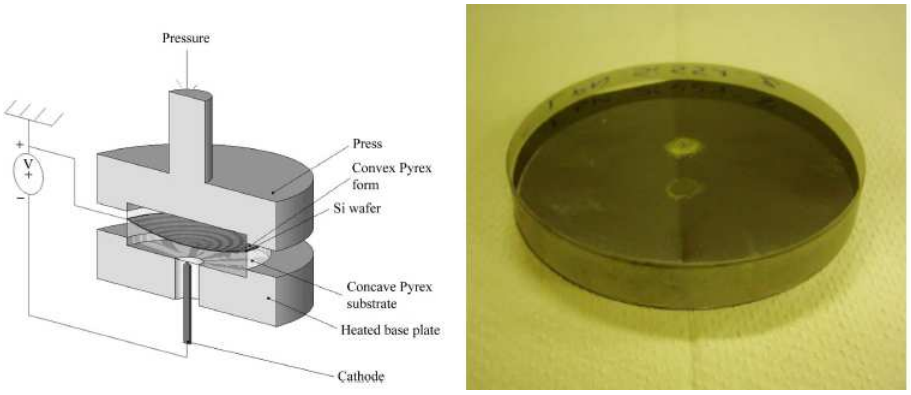

Figure 2.7: (left) Press for anodic bonding; (right) Bent Si(53) analyzer (from Collart et al. [34]).

2.2.2 Optics

2.2.2.1 Overview

IXS setups are nowadays widespread at synchrotron facilities. If details of the beamline optics can differ, they have in common a high-resolution monochromatization stage and focusing optics, both necessary to IXS measurements.

A typical beamline setup is shown in Fig. 2.8. It is essentially based on a 2-crystal fixed-exit pre-monochromator followed by a 4 crystal high-resolution monochromator and focusing optics comprising a toroidal mirror and a set of Kirkpatrick-Baez (KB) mirrors. A collimating mirror placed upstream of the high-resolution monochromator ensures maximum throughput, as explained below.

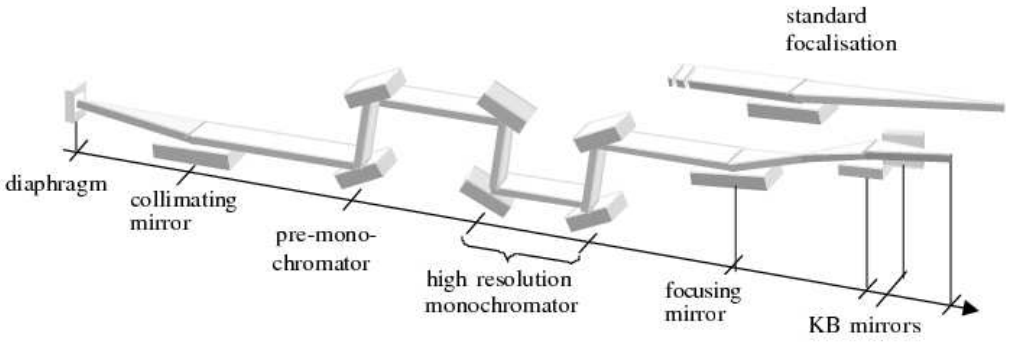

Figure 2.8: Main optical elements of the GALAXIES beamline at SOLEIL in the micro-focusing mode (front) and standard focalization (back).

2.2.2.2 Monochromatization

To achieve resolution compatible with spectroscopic needs, the monochromator bandwidth has to be adapted between 50 meV and 1 eV. An efficient and versatile design consists of combining a two-bounce channel cut with a four-bounce monochromator.

The channel-cut energy resolution at a given Bragg reflection characterized by its Darwin width $\delta\omega_D$ reads as follows :

$$\frac{\Delta E}{E} = \delta\omega_D \cot\theta_B \tag{2.11}$$

Away from backscattering, the effect of the incident beam divergence $\delta\omega_i$ can be included in Eq. 2.11 by replacing ω_D by $\sqrt{\delta\omega_D^2 + \delta\omega_i^2}$. The formula 2.11 can be graphically illustrated using the Dumond diagram as on Fig. 2.9(a) for a two-bounce channel cut. Interestingly enough, in the case of a four-bounce (2+2) reflection (Fig. 2.9(b)) in the dispersive geometry, the resolution in independent of $\delta\omega_i$ (providing $\delta\omega_D < \delta\omega_i$) but the throughput (gray area) is optimum when $\delta\omega_i$ matches $\delta\omega_D$. This condition can be fulfilled by placing a collimating mirror before the four-bounce monochromator.

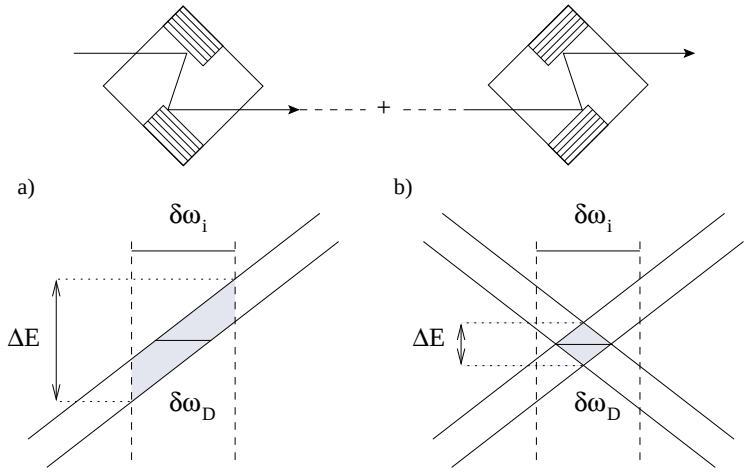

Figure 2.9: Dumond diagram for a two-bounce (a), or four-bounce setup (b).

Chapter 3

Results of High Pressure IXS

"With four parameters I can fit an elephant and with five I can make him wiggle his trunk", John von Neumann

3.1 Pressure setups for the spectroscopist

Among various pressure apparatus, diamond anvil cells (DAC) are leading the race in spectroscopy (cf. Ref. [35] for an extensive description of DAC technique). Let alone the exceptional hardness of diamonds which has pushed the highest achievable pressures to the megabar region, diamonds are transparent in a broad spectral range covering infrared, visible light, and x-ray (mostly above 5 keV). DAC are small devices which can be easily mounted on a goniometer head, in a vacuum chamber or in a cryostat for low-temperature measurements, or coupled to a power-laser source such as in laser-heating technique.

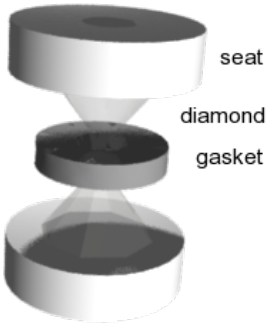

Figure 3.1: Close-up around the sample in a diamond anvil cell

The sample is loaded in a chamber drilled in a gasket that serves to limit pressure gradient during compression by the two diamonds. To ensure hydrostaticity, the gasket chamber is normally filled with a pressure transmitting medium. Ruby chips are also inserted for pressure calibration. Different geometry can be envisaged depending on the experimental needs. Fig. 3.2 illustrates setups in the in-plane, transverse or transmission geometries. Both in-plane and transverse geometries require x-ray transparent gasket material such as high-strength Be. The choice of the cell geometry is in part dictated by the absorption of the diamonds, particularly strong along the exit path – the scattered energies typically fall within the 5–10 keV energy range – which makes it difficult to work in full transmission geometry. However to determine the optimum geometry, self-absorption of the scattered x-rays has to be taken into consideration.

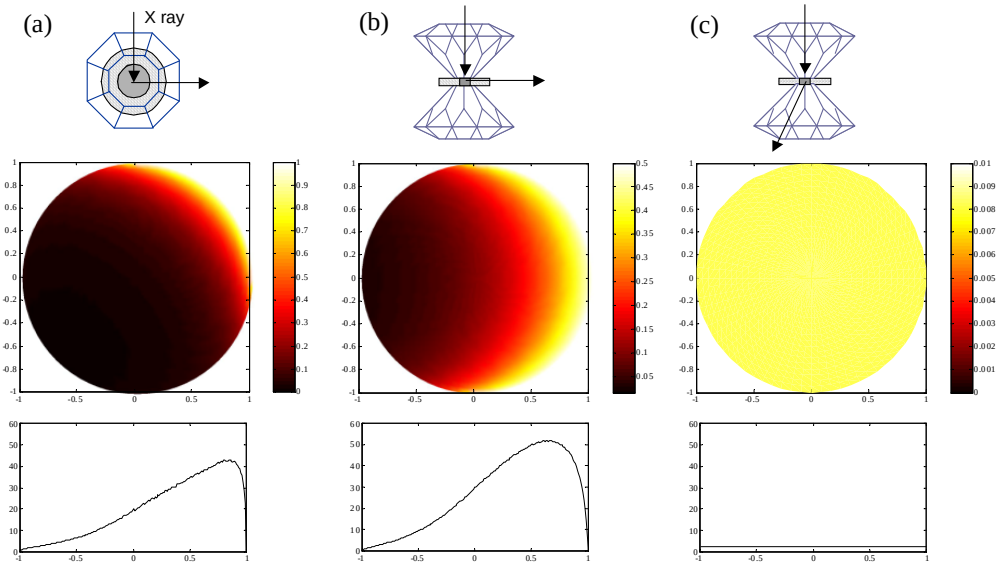

Figure 3.2: Self absorption effect in a model transition-metal oxide sample contained in a pressure cell. From top to bottom, sample geometry (a) in-plane scattering (b) transverse geometry, (c) full transmission (the sample and the gasket are shown in gray); 2D emission profile; integrated intensity. The sample diameter is 100 μm, and we considered an attenuation length of 30 μm, typical of metal oxides around 8 keV. (from Ref. [36])

The self-absorption strength depends on the sample total length projected along the detection direction, here the sample-analyzer axis, and the x-ray attenuation length for the considered material. The 2D intensity profile emitted by the sample is simulated on figure 3.2 for different geometries : (a) in-plane scattering through a Be gasket, (b) transverse geometry (the incident x-ray enters the cell through diamond and exits through a Be gasket), or (c) full transmission through the diamonds. The simulation was carried out by considering a sample of diameter 100 μm placed in an incident x-ray beam of 15 keV, and an attenuation length of 30 μm, conformed to the value found at the Kβ emission-line energy in the considered transition-metal oxides. As expected, the highest peak-intensity is obtained for the in-plane configuration, but because both incident and emitted x-ray are strongly absorbed, only a portion covering about one-third of the sample surface is visible from the analyzer point of view. In the transverse configuration, the fluorescence comes approximately from one-half of the sample. Even if the first diamond absorbs part of the incident beam, the integrated intensity is comparable to the in-plane configuration thanks to the wider emitting area. Finally, a homogeneous sample can be obtained in the full transmission mode, but then the emitted intensity is strongly absorbed by the exit diamond, resulting in a loss of intensity by a factor of ≈30. This limitation can

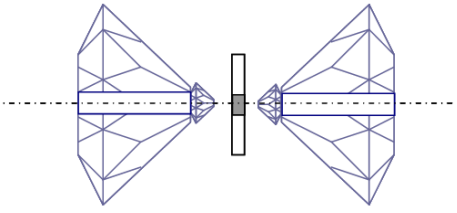

Figure 3.3: Diamond anvil cell in transmission geometry with perforated diamonds. Sample is shown in dark gray

be avoided to a large extent by using perforated diamonds as recently proposed [37]. The diamonds can be either partially emptied leaving simply a thin but opaque back-wall (down to 200 microns) or fully drilled as illustrated in Fig. 3.3 ; in such a case a small diamond (typically of 500 microns height) is glued onto the tip of the perforated (bigger) diamond with the advantage of an optical access to the sample chamber. In the very high pressure regime, solid diamonds are preferable and the transverse geometry therefore appears as the best compromise between integrated intensity and sample homogeneity, as far as the sample size is kept small compared the attenuation length and hydrostaticity preserved throughout the entire pressure range. Finally, EXAFS measurements down to the S K-edge (2.47 keV) under high-pressure was recently made possible by using Be gaskets in the in-plane geometry where part of the gasketting material was hollowed-out along the scattering path.

3.2 Transition metals at high pressure

3.2.1 Spin state transition

3.2.1.1 XES at the Kβ line

Besides other techniques conventionally devoted to magnetism, x-ray emission spectroscopy can be used as an alternative probe of the transition-metal magnetism (for a comparison between magnetic probes, cf. Ref. [51]). XES is well suited to high-pressure studies thanks to the intense fluorescence yield in the hard x-ray energy range, especially when combined with bright and focused x-ray beams provided by third-generation synchrotron sources. More particularly, the Kβ ($3p \rightarrow 1s$) emission line from the transition metal atom (and to a less extent the Kα ($2p \rightarrow 1s$) line) turns out to be extremely sensitive to the transition metal spin state.

A typical example of a Kβ emission line is shown in Fig. 3.4. The spectral lineshape is characterized by an intense main line (K$\beta_{1,3}$) and a satellite structure (usually referred to as Kβ') on the low energy side. The satellite has been successively proposed to arise from exchange interaction [52], shake-up or plasmon phenomena, and charge transfer effects [53], before being attributed correctly to the multiplet structure [54–56]: The Kβ-XES initial state is formed by $1s$ core-hole. For a $3d^n$ ion with a ^{2S+1}L configuration (where L and S are the total orbital and spin momentum), the $1s$-$3d$ exchange interaction splits the degenerate ground state into two configurations of high-spin (^{2S+2}L) and low-spin symmetry (^{2S}L). In turn in the final state the $3p$-$3d$ exchange interaction leads to two "spin-polarized" configurations that result from the two possible spin orientations for the $3p$ hole with respect to spin-up d electrons. These, in principle, can be simply constructed from the high-spin and low-spin symmetries of the emission initial state. But configuration interaction both in the initial and final states leads to mixing of states, ending in a complicate multiplet structure which spreads over the entire spectral range. In the Kβ emission case, the spread of the multiplet terms is nevertheless dominated by the $3p$-$3d$ exchange interaction because the strong $3p$ overlap with the $3d$ states. As first proposed by Tsutsumi et al. [52], the energy difference between the main peak K$\beta_{1,3}$ and the satellite Kβ' is then well approximated by $J(2S+1)$, where J is the exchange parameter (of the order of 15 eV). The satellite and main emission line then approximatively coincides with the spin-up ($\underline{3p^{\uparrow}}3d^{\uparrow}$) and spin-down components ($\underline{3p^{\downarrow}}3d^{\uparrow}$). The $3p$ spin orbit splits the states further within $\sim$1 eV. Through a magnetic collapse transition, the $3d$ magnetic moment abruptly changes and so does the Kβ lineshape (see Fig. 3.4).

Thus, XES appears as a local probe of the $3d$ magnetism. No external magnetic field is

Sample	Formal Valence	P (GPa)	Structure	Properties	S	(Ref.)
MnO	2+	0 100	NaCl NiAs	(AF)I (NM)M	HS LS	[38]
Fe	2+	0 13	bcc hcp	(FM)M (NM)M	HS LS	[39]
FeS	2+	0 10	NiAs Monoclinic	(AF)I (NM)M†	HS LS	[40]
FeO	2+	0 140	NaCl NiAs*	(AF)I (NM)M	HS LS	[41]
Fe_2O_3	3+	0 60	Corundum Corundum*	(AF)I (NM)M	HS LS	[42]
Fe_3C	3+	0 10–25	Orthorhombic Orthorhombic	(FM)M (NM)M	HS LS	[43]
Fe-Ni (Invar)	2+	0 20	fcc fcc	(FM)M (NM)M	HS LS	[44]
(Mg,Fe)O	2+	0 60	NaCl NaCl	(PM)I (NM)M	HS LS	[45–47]
$(Mg,Fe)SiO_3$	2+/3+	0 120	Perovskite Perovskite	PM(I) (NM)I	HS/HS LS/LS	[48]
CoO	2+	0 100	NaCl NaCl	(AF)I (NM)M	HS LS	[38]
$LaCoO_3$	3+	0 10	Perovskite Perovskite	(PM)I (NM)M	IS LS	[49]
$La_{0.72}Sr_{0.18}CoO_3$	3+/4+	0 14	Perovskite Perovskite	(PM)M (NM)I	IS/LS LS/LS	[50]
$Pr_{0.5}Ca_{0.5}CoO_3$	3+/4+	0 12	Perovskite Perovskite	(PM)M (NM)I	IS/LS LS/LS	[50]
NiO	2+	0 (140)	NaCl NaCl	(AF)I (AF)I	HS HS	[38]

Table 3.1: Summary of main properties of the studied transition metal samples under pressure. S is the spin state obtained from XES. I(M) corresponds to insulating (metallic) state.
(*debated structure)
(†or semi-conducting)

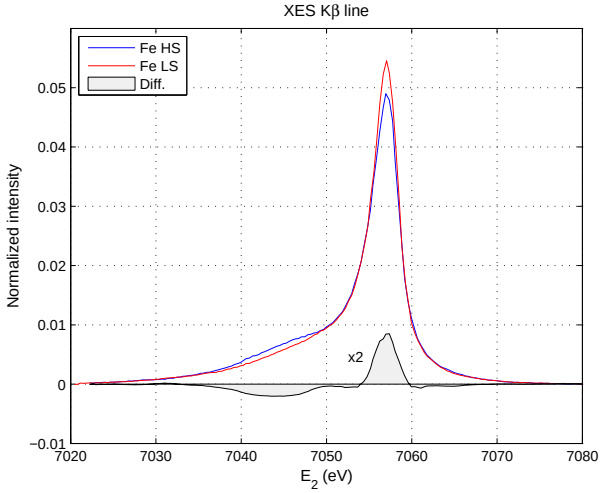

Figure 3.4: Fe Kβ emission line through a pressure-induced high-spin to low-spin transition. The spectra are normalized to an area of one. HS-LS difference spectrum is shown in gray

required since XES benefits from the intrinsic spin-polarization of the d electrons. In the following, we will review XES results obtained in various transition metal compounds under high pressure (and temperature) conditions. Starting from a purely phenomenological approach, we will see that the variation of the XES lineshape across a magnetic transition is well accounted for by full multiplet calculations including ligand field and charge transfer effects, giving insights on the d electrons properties under extreme conditions.

3.2.1.2 Integrated absolute difference

The magnetic information contained in the XES spectra is not immediately available. In the absence of formal sum rules such as in x-ray magnetic circular dichroism (XMCD), one is restricted to using a more approximate approach. The changes of the local magnetic moment can be estimated from the integrated absolute difference (IAD) [39, 49, 57] which relates the spectral lineshape to the $3d$ spin-state as follows :

$$\text{IAD} = \int |I_{XES}(\omega, P) - I_{XES}(\omega, P_0)|\, d\omega, \tag{3.1}$$

$I_{XES}(P)$ is the intensity of the x-ray emission at a given pressure P; P_0 is a reference pressure point. The IAD is a phenomenological analysis but shows a remarkable agreement when compared to model systems. Fig. 3.5 for instance illustrates the IAD analysis applied to Fe^{2+} simulated spectra of known spin state. The spectra are constructed from a linear combination of γ_{HS} HS and $(1 - \gamma_{HS})$ LS XES spectra. The deviation $\Delta\gamma_{HS}$ of the extracted high spin fraction compared to the known values is negligible. This is no longer the case when other extraction techniques of the spin state are used.

The IAD method has been widely applied for the quantitative estimate by XES of the spin-state under pressure.

3.2.1.3 Temperature effect

At a given pressure, excited spin states of energies within k_BT from ground state will mix. At equilibrium, the spin population in a pure atomic approach can be described by considering an assembly of ions in a series of spin states i defined by their enthalpy H_i

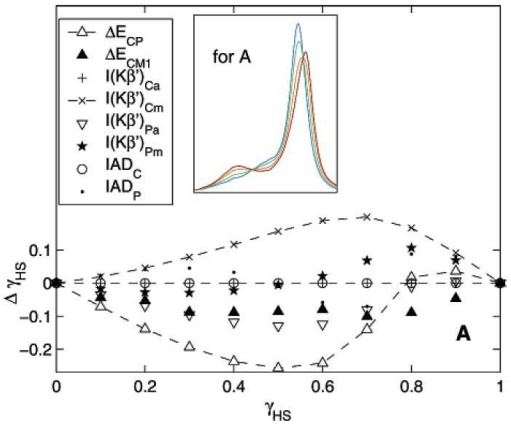

Figure 3.5: Deviations of the HS fraction γ_{HS} as determined from different extraction techniques (see details in the cited reference) in simulated XES spectra of known spin state. The spectra are constructed from a linear superposition of theoretical HS and LS spectra in a Fe^{2+} ion with a HS weight γ_{HS} (inset). The IAD values (open circles and dots) show the best results (from Vankó et al. [57]).

and degeneracy g_i. The fraction of ions in the i-state is expressed by Eq. 3.2, assuming a Boltzmann statistics ($\beta = 1/k_BT$). The main effect of temperature is to broaden the spin transition as illustrated in Fig. 3.6. According to this simulation, a broadening of the transition is already observed at room temperature, where most of the measurements were performed. However, the disturbance due to thermal excitations becomes dominant only in the very high temperature region.

$$n_i = \frac{1}{1 + \sum_{j \neq i} \frac{g_j}{g_i} \exp[-\beta(H_j - H_i)]} \tag{3.2}$$

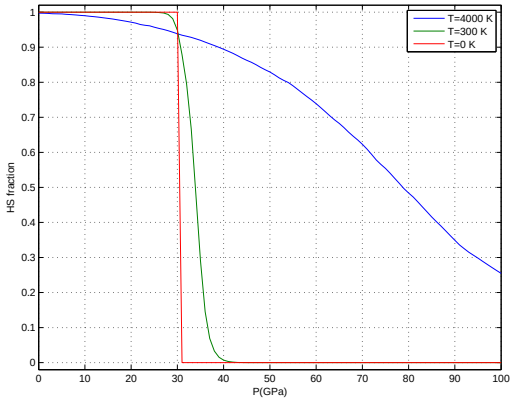

Figure 3.6: HS fraction in Fe^{2+}. Pressure dependence of enthalpies was borrowed from Tsuchiya et al. [58].

3.2.1.4 Fe compounds

FeS First observation of magnetic collapse using of XES was obtained in FeS [40]. FeS is an anti-ferromagnetic insulator (T_N=598 K) and crystallized in the NiAs-related (troilite) structure (cf. Table 3.1 for a summary of the samples properties). FeS falls at the boundary

between charge-transfer and Mott-Hubbard insulators in the ZSA phase diagram ($\Delta < U$ with U relatively small) [59]. Pressure-induced structural phase transitions in FeS have been extensively studied because the material is considered to be a major component of the cores of terrestrial planets [60–62]. Under pressure and ambient temperature, FeS undergoes two structural phase transitions, from the NiAs-related to a MnP-related structure at 3.5 GPa, and then to a monoclinic phase at 6.5 GPa. The last transition is further accompanied by an abrupt shortening of the c parameter from 5.70 to 5.54 Å. Fig. 3.7

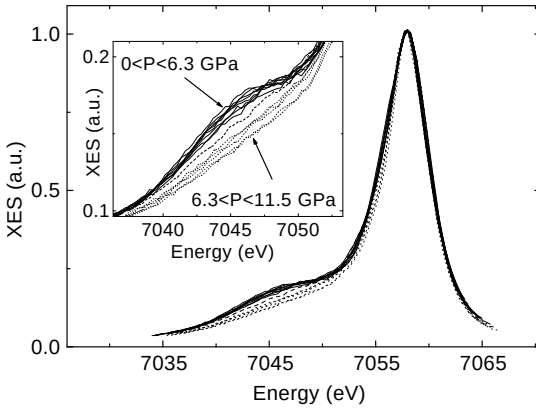

Figure 3.7: Fe Kβ emission line in FeS as a function of pressure. At low pressure, the satellite at 7045.5 eV is characteristic of the HS state. The satellite decrease at high pressure denotes the transition to the LS state (dotted lines) (from Rueff et al. [40]).

show the changes XES spectra measured as pressure changes from 0 to 11.5 GPa. The well defined satellite at low pressure is indicative of the local magnetic state of the Fe^{2+} ion (despite the anti-ferromagnetic long-range order). The satellite intensity disappears in spectra for pressures ranging between 6.3 and 11.5 GPa. The width of the main line also shows significant narrowing in this pressure range, as expected in the low-spin state.

Fe Iron is another example where the structural change is accompanied by a magnetic collapse. At room temperature and with increasing pressure, iron shows a phase transition from the ferromagnetic α-phase (bcc) to the non-magnetic ϵ-phase (hcp) around 13 GPa. The α-ϵ transition is well documented by Mössbauer spectroscopy [63]. The IAD analysis applied to Fe (cf. Fig. 3.8) shows a decrease spin state at 10 GPa before it reaches a full low spin state at 15 GPa in good agreement with the Mössbauer data.

The α-ϵ transition shows the interplay between structural and magnetic transitions, of which the Invar effect (see below) is another emblematic example. Whether the magnetic collapse precedes the structural change or not is still a matter of debate. Recent experiments in pure Fe by XMCD seems to indicate the anteriority of magnetism collapse over the structural changes [64]. On the contrary, results in hematite (Fe_2O_3) have demonstrated that crystal-structure change is likely to drive the electronic transition.

Fe_2O_3 Hematite is a wide-gap AF insulator considered as archetypal of a Mott localization. The stable α-phase at ambient pressure crystallizes in the corundum structure. At a pressure of about 50 GPa, Fe_2O_3 transforms into a low-volume phase of still debated nature. Recent Mössbauer study has demonstrated that the structural change is accompanied by an insulator to metal transition, understood by the closure of the correlation gap and the emergence of a non-magnetic phase [65]. The abrupt magnetic collapse at 50 GPa was confirmed by XES experiment at the Fe Kβ line (cf. Fig. 3.9(a)). More interestingly, in a

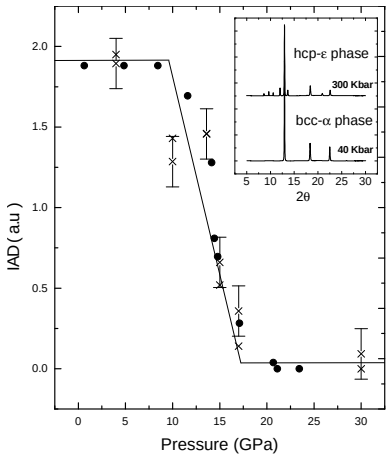

Figure 3.8: Integrated absolute difference calculated from the XES spectra in pure Fe compared to the α-phase fraction determined by Mössbauer spectroscopy (Ref. [63], solid circles) across the transition. The diffraction pattern measured in both phases, shown in the inset, confirm the structural change. Spin state is indicated (from Rueff et al. [39]).

similar XES experiment at the Advanced Photon Source the evolution of the spectral lineshape was acquired simultaneously to measurements of the x-ray diffraction pattern [42]. Hematite was compressed to 46 GPa without noticeable change of spin or structure (state 1 in Fig. 3.9(b)). At that point, the sample was laser heated using an offline Nd:YAG laser and immediately quenched in temperature, thus let in metastable state (state 2) characterized by a LS state and a structure typical of the high pressure phase. After relaxation, the electronic spin state reverts to the initial HS state while the structure stays unchanged showing that the LS is not required to stabilize the high pressure strucural phase.

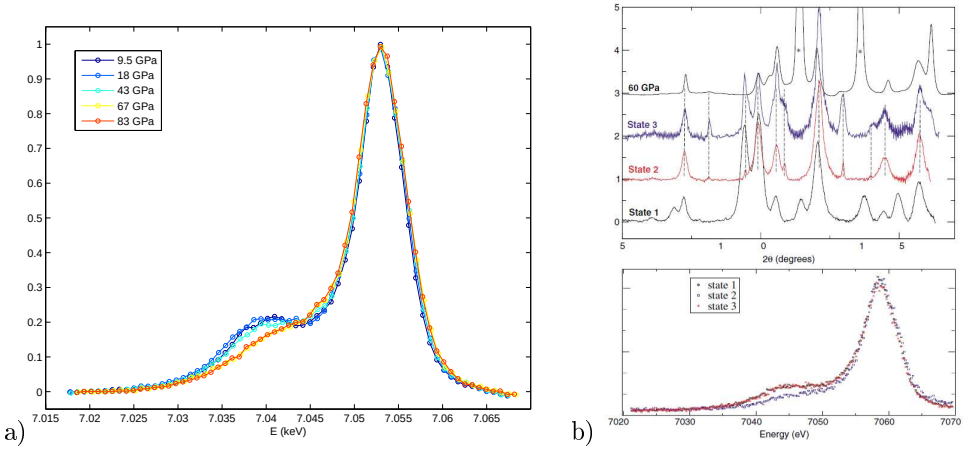

Figure 3.9: a) Fe Kβ emission in Fe_2O_3 as a function of pressure (from Rueff [66]); b) Diffraction patterns through the metastable phase transition and correspoding XES spectra (adapted from Badro et al. [42]).

Fe Invar The Invar effect is the anomalously low and stable thermal expansion of certain metallic alloys over a wide range of temperature. One of the most commonly accepted models of the Invar anomaly is the so-called 2γ-state model proposed by Weiss [67]. According to this model, iron can occupy two different states: a high volume state and a slightly

less favorable low volume state. With increasing temperature, the low volume state is thermally populated thus compensating the lattice expansion. This model is supported by fixed-spin moment calculations in Invar which shows that, as a function of temperature, the Fe magnetic state switches from a high spin to low spin states of high and low atomic volume respectively [68]. The same effect is also expected under applied pressure at ambient temperature: Pressure tends to energetically favor a low volume state, eventually leading to a HS to LS transition.

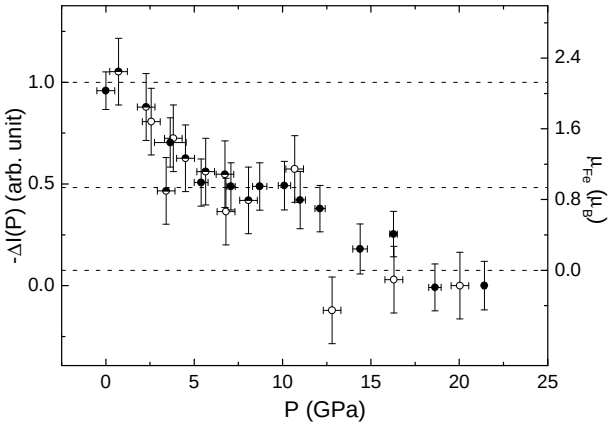

Figure 3.10: Integrated absolute difference calculated from the XES spectra in the Fe-Ni Invar. The open, half filled, and solid circles represent IAD value for the consecutive series of measurements. The right scale is deduced from the pure Fe XES data. Horizontal lines emphasize the three magnetic states (HS, LS, NM) of the Fe atom (from Rueff et al. [44]).

The spin state of Fe in $Fe_{64}Ni_{36}$ was monitored by XES at the Fe Kβ line up to 20 GPa in a diamond-anvil cell. The pressure dependence IAD(P) is shown in Fig. 3.10. In the low pressure region below 5 GPa, the curve presents a linear decrease followed by a plateau in the intermediate pressure region which extends up to about 12 GPa. At higher pressures, the intensity drops to zero around 15 GPa and plateaus there up to the highest measured pressure point around 20 GPa. The existence of two plateaus supports the interpretation of two magnetic transitions taking place in the 2–5 GPa and in the 12–15 GPa ranges, respectively. This clearly demonstrates the existence of three distinct magnetic states that are successively reached as pressure is increased: HS ($S = 5/2$), LS ($S = 1/2$) and finally diamagnetic ($S = 0$). Further information on the magnetism in Invar can be obtained comparing the Invar XES spectra with those previously measured in pure iron under pressure. This confirms that: i) the Fe atom in the Invar alloy is in a high-spin state at zero pressure as it is in iron and, ii) at high pressure 20 GPa, the Fe atom in the Invar alloy is in a nonmagnetic state as it is in ϵ iron, iii) therefore the plateau in the intermediate pressure region can be associated with the existence of a low spin magnetic state.

This interpretation supports the 2γ-state model and is also in qualitative agreement with XMCD [69] and Mössbauer measurements carried out on both Fe-Pt Invar and Fe-Ni Invar under pressure. Note that these two techniques probe the long range magnetism contrary to XES which has pure local character. The deduced magnetic moment (here in the sense of magnetization) is thus sensitive to the reported decrease of the Curie temperature with pressure in Invar alloys. In the recently discovered Invar Fe_3C for instance, a HS-LS transition was found at 10 GPa [70] by XMCD whereas the magnetic instability manifests itself in the XES spectra at 25 GPa [43]. The difference is related to the occurrence of a paramagnetic phase (at room temperature) above 10 GPa.

3.2.1.5 Fe solid-solutions: Geophysical aspects

In solid solutions, the transition metal ions form an assembly of isolated magnetic impurities bearing a local moment. At low pressure, electron correlations are important because of the narrow *d*-band. Under pressure, electron itinerancy sets in while the *d*-band broadens and solid solutions then provide an interesting counterpart to compounds or alloys. Fe solid solutions are often found in relevant minerals for geophysics. Being able to describe the electronic properties of these materials under high pressure (and temperature) is crucial for the description of their properties (elasticity, thermodynamics, transport) under realistic conditions for planetary studies.

(Mg,Fe)O Magnesiowüstite is considered as the dominant phase of the Earth's lower mantle. At ambient conditions of pressure and temperature, (Mg,Fe)O is a paramagnetic insulator of moderate charge transfer character with Fe^{2+} in the high spin state. AF correlation builds up when temperature is decreased with a Néel temperature T_N of about 25 K (with 20% of iron). The spin state of iron was measured in $(Mg_{0.83},Fe_{0.17})O$ by XES. The spectra (cf. Fig. 3.11) change with pressure denotes a broad transition from HS to LS. The transition starts around 20 GPa and full conversion to LS state is completed in the 60–70 GPa region [45]. The magnetic transition was confirmed laterly by Mössbauer spectroscopy [71, 72].

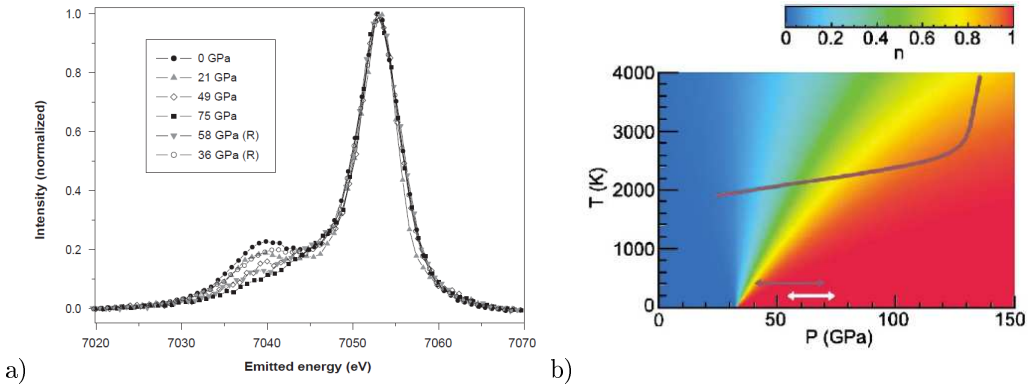

Figure 3.11: a) Fe X-ray emission spectra measured in magnesiowüstite solid solution $(Mg_{0.83},Fe_{0.17})O$ (from Badro et al. [45]); b) computed LS fraction n in the (P,T) space (from Tsuchiya et al. [58]).

Recent calculations give insights into the electronic properties and magnetic transition in magnesiowüstite under pressure [58]. Using an LDA+U approach, both U and the *d*-bandwidth W are found to increase with pressure but the latter at a faster rate so that U/W eventually decreases, an indication of less correlation in the high pressure phase. Because the LS and HS states have closed energies, the average spin state at finite temperature is a Boltzman average of the two spins as shown in Fig. 3.11(b). In this picture, there is a coexistence of Fe(LS) and Fe(HS) sites in the lattice. A different approach is proposed in section 3.2.1.7. The magnetic collapse also impacts on the compressional behavior of the Fe mineral: The high-pressure LS state exhibits a much higher bulk modulus and bulk sound velocity than the HS phase at low pressure [46] which can be traced back to the lower atomic volume of the LS state.

(Mg,Fe)SiO_3 Iron perovskite $(Mg,Fe)SiO_3$ is another candidate for the Earth's lower mantle mineralogy. Under high pressure conditions, it undergoes two successive mag-

netic transitions around 70 GPa and 120 GPa as observed by XES at the Fe Kβ line (cf. Fig. 3.12(a)) [48]). The transitions are characterized by a sudden decrease of Kβ' peak intensity and a shift of the K$\beta_{1,3}$ feature to lower energy.

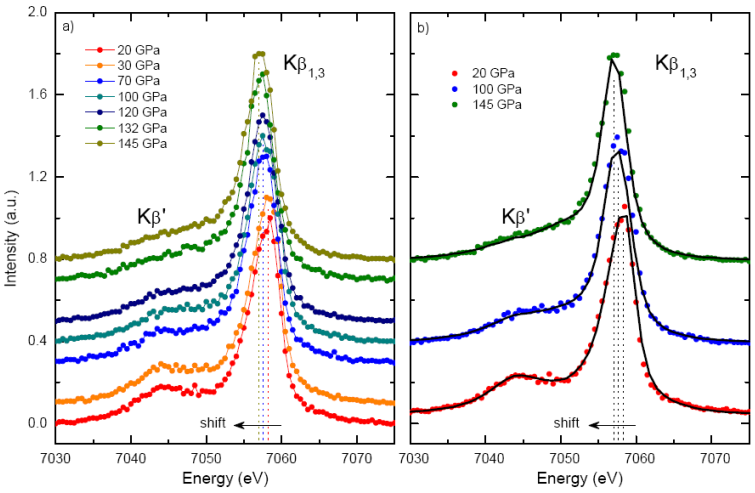

Figure 3.12: a) Fe X-ray emission spectra measured in $(Mg_{0.9},Fe_{0.1})SiO_3$ between 20 and 145 GPa; b) XES spectra in model compounds (solid lines) are superimposed to three spectra representative of the three different spin states (from Badro et al. [48]).

In the perovskite, iron is present as ferrous (Fe^{2+}) or ferric (Fe^{3+}) species. It is admitted that the ferrous iron occupies the large dodecahedral A site, whereas the smaller octahedral B site is the host of ferric iron together with lesser amounts of the ferrous species. In the measured sample, perovskite is supposed to contain 75% of Fe^{2+} and 25% Fe^{3+}, with 75% of the Fe^{2+} being in the A site and 25% in the B site and all Fe^{3+} being in the B site. This leads to 56% ferrous dodecahedral, 25% ferric octahedral, 19% ferrous octahedral sites; i.e., 56% of total iron in the A site and 44% in the B site. To clarify the nature of the two transitions, the XES spectra in $(Mg,Fe)SiO_3$ are compared in Fig. 3.12(b) to spectra obtained in Fe model compounds containing Fe^{2+} or Fe^{3+} iron in pure HS and LS spin states. To help the comparison with the perovskite data, composite spectra were built from the model compounds, starting from the known abundance of Fe^{2+} and Fe^{3+} ions. Best agreement is obtained by combining model spectra of ferrous and ferric iron both in the HS states in the low presure region, while the high pressure regime is well described by having both ions in the low spin states. In the intermediate regime, a mixed state is seemingly realized with relative amounts of the HS and LS iron species of ~55% and 45%, respectively. This could indicate that the transition is site-specific; the first and second transitions could correspond to electron pairing in the A then B site, respectively.

From simple crystal field arguments, one expects the magnetic collapse in $(Mg,Fe)SiO_3$ to lead to a blue shift of the iron absorption bands. Initially in the infrared (IR) and red region, it is expected to shift to the green-blue region when in the LS state. This interpretation is at odds with the charge transfer character of the insulating gap. Calculations in magnesiowüstite suggest a red-shift of the optical absorption spectrum due to the partial closure of the charge-transfer gap at high pressure [58].

3.2.1.6 Co compounds

$LaCoO_3$ The rhombohedral perovskite $LaCoO_3$ is an unusual case of a non-magnetic semi-conducting ground state. Because of the large crystal field splitting, Co is trivalent

(e_g^6 configuration) at 0 K with a low-spin state ($S = 0$). As a function of temperature, two broad transitions have been observed in the magnetization measurements at around 90 K and 500 K. The first transition is conventionally interpreted by the occurrence of a $t_{2g}^4 e_g^2$ ($S = 2$) high spin state while the metallization which goes with the second transition at high temperature remains of unclear origin. Other interpretations have proposed more recently the formation of an intermediate spin state (IS) ($S = 1$) above 90 K, characterized by a doubly degenerated $t_{2g}^5 e_g^1$ configuration. The stability of the spin state in $LaCoO_3$ was studied Korotin et al. [73] within a LDA+U calculations. The non-metallic state in the low temperature range is attributed to the intermediate spin: The degeneracy of the IS state is lifted by Jahn-Teller effect, which supposedly leads to an orbital ordering on the Co sites and the opening of the semi-conducting gap. In this model, the high temperature insulator/metal transition is accounted for by the "melting" of the orbital-ordered state. Hints of a LS to IS transition have been identified in the T-dependence of the magnetic susceptibility [74].

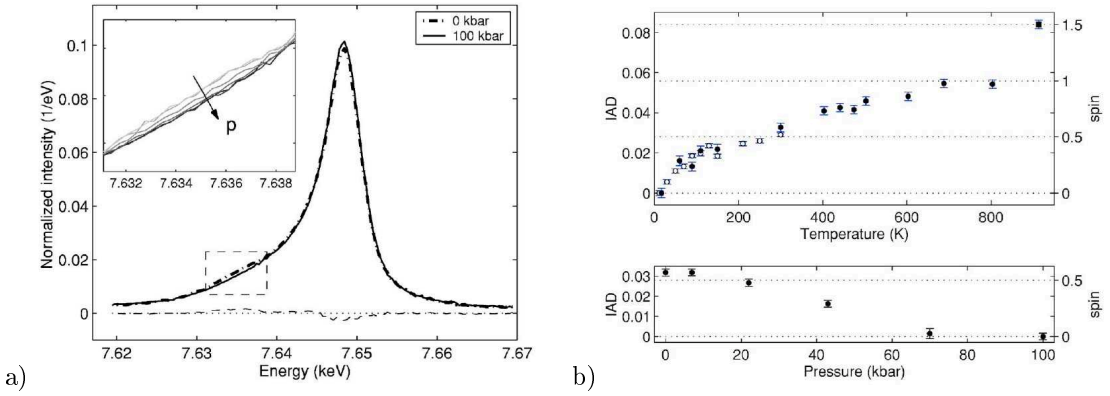

Figure 3.13: a) Evolution of the Kβ emission line in $LaCoO_3$ as a function of pressure; b) Pressure ($T = 300$ K) and temperature (at ambient pressure) dependence of IAD values derived from XES (left scale) and estimated Co spin-state (right scale) (from Vankó et al. [49]).

Pressure can also cause spin-state transitions in $LaCoO_3$, as the crystal field splitting sharply increases when bond lengths shrink. Since the transitions of $LaCoO_3$ are associated to anomalous volume expansions, it is apparent that relatively low pressure can have considerable effect on the spin state. Asai et al. [75] showed that the energy gap between the LS and the higher spin state increases with pressure. More recently, Vogt et al. [76] interpreted the pressure-induced changes by x-ray powder diffraction as a continuous transition from IS to LS state. Chemical pressure, introduced by a partial substitution of La^{3+} with the smaller Eu^{3+}, leads to a similar stabilization of the LS state.

The pressure (and temperature) dependence of the Co spin state was investigated by XES at the Co Kβ line [49]. Fig. 3.13(a) shows the evolution of the emission spectra as a function of pressure. A gradual variation of the Kβ lineshape is observed up to 70 kbar. The data are further analyzed using the IAD approach (cf. Eq. 3.1). The IAD values were rescaled to spin moment by comparison to model Co-compounds with a well characterized spin-state: $S = 2$ in CoF_3; $S = 1.5$ in $LaCoO_{2.5}$; $S = 1$ in Co^{2+}-molecular compounds; $S = 0$ in $LiCoO_2$ (right scale, Fig. 3.13(b)). The pressure dependence can be analyzed in terms of spin-excited states: At ambient temperature and low pressure, both $S = 0$ and $S = 1$ states are populated leading to an average of $S \sim 0.5$. Upon pressure increase, the low-volume/low-spin state is increasingly favored with respect to IS. Full LS state is reached around 100 kbar. In contrast, the spin state increases with temperature. Starting

from the LS state at low T, S ramps up progressively to $S = 1$ at 800 K. In this T-region, the spin variation is well described by a Boltzman statistics [49] involving both LS and IS states but not the HS state. Above 800 K, the sample is no longer stoichiometric. Oxygen vacancies form and S jumps to 3/2, a value characteristic of $LaCoO_{2.5}$.

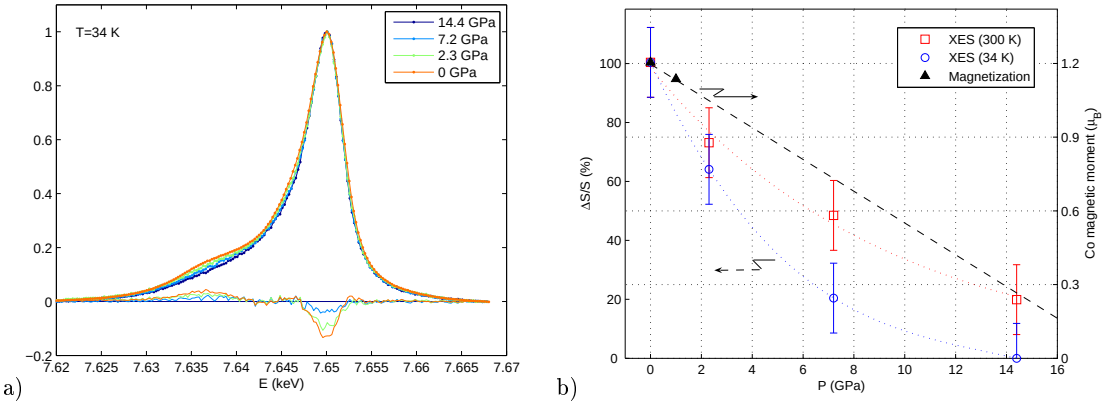

Figure 3.14: a) Evolution of the Co Kβ emission line in $La_{1-x}Sr_xCoO_3$ ($x = 0.18$) as a function of pressure at $T = 34$ K; b) Pressure dependence at 34 and 300 K of spin state (IAD values) derived from XES (from Lengsdorf et al. [50]). Dashed lines are guides to the eyes.

$La_{1-x}Sr_xCoO_3$ When substituting La^{3+} by Sr^{2+} ions, hole-type carriers are introduced in $LaCoO_3$. The hole-doped compounds are of particular interest as they clearly display the interplay between spin-state degree of freedom and electronic and magnetic properties close to a metal-insulator transition. Depending on the doping level, $La_{1-x}Sr_xCoO_3$ changes from a spin glass $x > 0.05$ to a ferromagnetic metallic character at $x \geq 0.18$. At ambient pressures, the $x = 0.18$ compound is reasonably conducting with a metallic like behavior in the FM regime. The behavior differs drastically under pressure [77]: above 2 GPa the compound departs from metallicity and turns into an insulator over the whole temperature range. More remarkably, the resistivity increases continuously under pressure until it saturates around 5.7 GPa. This contrasts for example with $La_{1-x}Sr_xMnO_3$ which is metallic under pressure, a behavior more in line with the expected band widening in the compressed unit cell.

Compared to the manganites, the metal ion in $La_{1-x}Sr_xCoO_3$ has an additional degree of freedom related to the spin state. The spin state was investigated by Kβ x-ray emission spectroscopy under pressure and temperature [50] (cf. Fig.3.14(a)). Fig.3.14(b) illustrates the variation of the spin state (in arbitrary units) with pressure at 300 K and 34 K. Similarly to $LaCoO_3$, S diminishes with pressure toward a LS configuration. At 300 K, the final spin value is higher than at low temperature as a probable consequence of thermally excited spin states. The conversion of the Co^{3+} ions into LS species under high pressure affects sensibly the electron transport properties through the lattice. As illustrated in Fig. 3.15, the e_g-type electron hopping which takes place between the Co^{3+} and Co^{4+} sites is strongly suppressed when the trivalent ion converts into a LS state and only the weak t_{2g} hopping remains. This blocking mechanism turns out to be efficient enough to provoke a metal-insulator transition at high pressure despite the bond length shortening (and increase of the Co-O-Co bond angle) which acts an opposite way by favoring double exchange.

$Pr_{1-x}Ca_xCoO_3$ Simultaneous metal-insulator and spin-state transition is also observed in this other series of cobaltates. $Pr_{0.5}Ca_{0.5}CoO_3$ was first shown to undergo a metal-

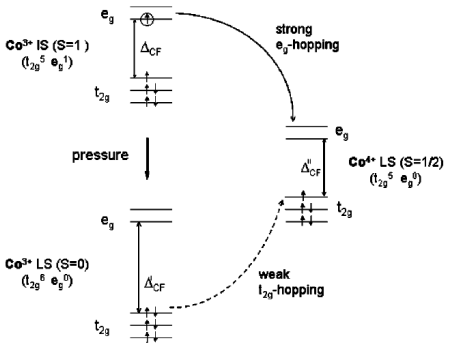

Figure 3.15: Electron hopping mechanism in the Co^{3+}/Co^{4+} lattice in $La_{1-x}Sr_xCoO_3$ (from Lengsdorf et al. [77]).

insulator and paramagnetic-paramagnetic spin-state transition at 90 K. The transition is marked by a sizable contraction of the unit cell (2% in volume) [78]. The transition is explained by the change from intermediate-spin to low-spin state on the Co^{3+} sites from the measurement of the bulk magnetization. Co^{4+} stays LS throughout the entire phase diagram.

The structural change suggests that a low-volume LS configuration is to be stabilized at high pressure. Fig. 3.16 displays the Co Kβ emission spectra in the half-doped sample as a function of pressure. A continuous decrease of the spin-state was indeed observed with increasing pressure up to 12 GPa by XES, similarly to $La_{1-x}Sr_xCoO_3$.

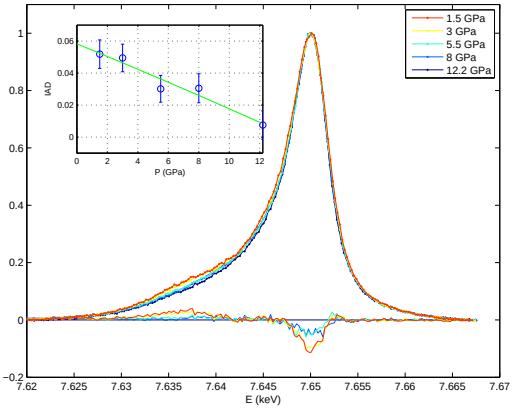

Figure 3.16: a) Evolution of the Co Kβ emission line in $Pr_{1-x}Ca_xCoO_3$ ($x = 0.5$) as a function of pressure at $T = 300$ K; (inset) Pressure dependence of spin state (IAD values) derived from XES).

3.2.1.7 Transition-metal monoxides

When occurring at very high pressure in strongly correlated materials, magnetic transition gives insights on high energy excitations of the systems (correlation, charge transfer) which are relevant to describe the transport properties and metal-insulator transition phenomena. With this aim in mind, magnetic collapse has been investigated in a series of prototypical strongly-correlated metals, MnO, FeO, CoO, and NiO in the megabar range [38] by XES. All these compounds are considered as wide-gap charge-transfer insulators [59, 79] ($\Delta < U$) except for CoO, closer to a Mott insulating state ($\Delta \approx U$).

Fig. 3.17(a–d) summarizes the Kβ emission spectra measured in the transition-oxides

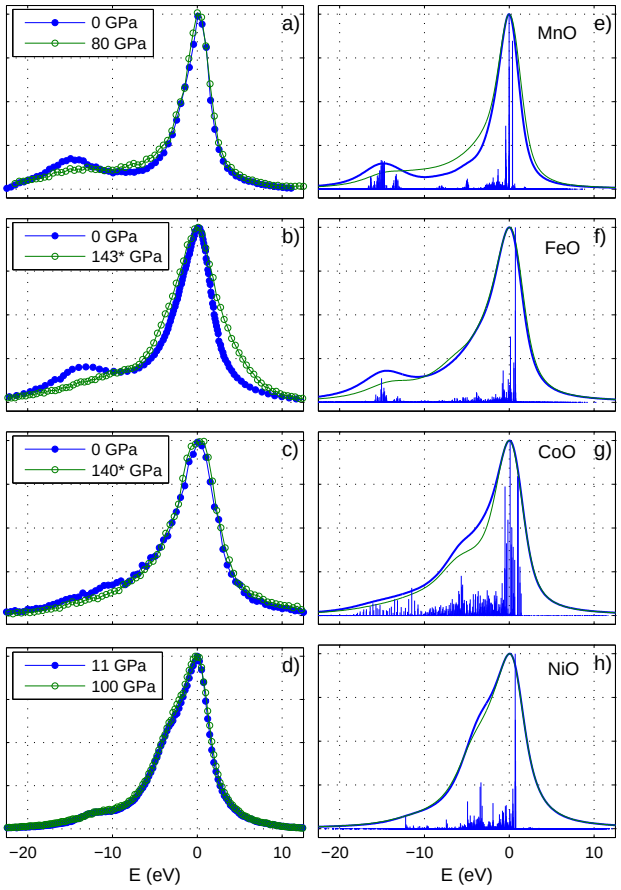

Figure 3.17: (a–d) Kβ-XES spectra measured in MnO, FeO, CoO and NiO in both low (close circles) and high pressure (open circles) phases. (*) indicates spectra obtained after offline laser-heating. (e–h) Calculated spectra at high pressures (thick) and low pressures (thin lines). Ticks represent the multiplet states, before broadening (from Mattila et al. [38].)

series at low and high pressures. All the spectra but NiO show significant modifications in the lineshape, essentially observed in the satellite region, through the transition[1]. Following the description put forward by Peng et al. [55] within the atomic multiplet formalism, the satellite is expected to shrink with decreasing $3d$ magnetic moment, and move closer to the main peak. This agrees well with the observed spectral changes when going from MnO ($3d^5$, $S = 5/2$) to NiO ($3d^8$, $S = 1$). It also qualitatively accounts for the collapse of the satellite at high-pressure observed in MnO, FeO and CoO, viewed as the signature of the HS to LS transition on the given metal ion. The indistinguishable spectra in NiO, where no such transition is expected, confirms the rule.

The atomic description however omits the crucial role played by the O($2p$)-M($3d$) charge-transfer effects and finite ligand bandwidth. Here, the data are analyzed in the light of full multiplet calculations within the Anderson impurity model [80, 81]. In contrast to band-like treatments of d electrons, crystal-field, ligand bandwidth, and charge transfer are here explicitly introduced as parameters. The model, derived from configuration interaction approach, was first put forward to explain the core-photoemission spectra of transition metal [82, 83]. It was later applied to the Kβ emission line in Ni-compounds [54] and more recently in transition metal oxides [84–86]. The multiplet calculation scheme yields an

[1] The asymmetric broadening of the main line in FeO at 140 GPa is an artifact

accurate model of the emission lineshape. More interestingly, it allows a direct estimate of the fundamental parameters, which are adjusted in the calculations with respect to the experimental data.

P (GPa)	Δ	U	V_{e_g}	$10Dq$	U_{dc}	W_{2p}
MnO						
0 (HS)	5	-	2.2	1	10	3
80 (LS)	6	-	3.06	1.6	10	4
100 (LS)	6	-	3.7	2.3	10	6
FeO						
0 (HS)	5	-	2.4	0.5	7	3
140 (LS)	5	-	3.2	0.8	7	9
CoO						
0 (HS)	6.5	6	2.5	0.7	7	4
140 (LS)	6.5	6	4.2	1.2	7	9
NiO						
0	3.5	8.2	2.4	0.3	9	5
140	4.5	9.2	3	0.65	9	7.5

Table 3.2: Parameters used in the calculations (in eV): Δ is the charge transfer energy; U the d-d correlation; V_{e_g} the hybridization strength; the crystal-field splitting is given by $10Dq$, and the core-hole Coulomb interaction by U_{dc}; W_{2p} denotes the ligand bandwidth.

Inclusion of the charge-transfer in the multiplet calculations substantially improves the simulated main-peak to satellite intensity ratio, via a transfer of spectral weight to the main peak. In the cluster model charge-transfer enters the calculations through a configuration interaction scheme. The ground state is described by a linear combination of $3d^n$ and $3d^{n+1}\underline{L}$ configurations, where $\underline{L}$ denotes a hole in the O-$2p$ states. A third configuration ($3d^{n+2}\underline{L}^2$) was added for CoO ($n = 7$) and NiO ($n = 8$). The calculations were made in the O_h basis set at 300 K, i.e. considering thermal population of excited states. Details on the computational method is given in Ref. [38]. The model parameters were first chosen to reproduce the emission spectra at ambient pressure. The parameters, charge-transfer energy Δ, hybridization strength in the ground state (V_{e_g} and $V_{t_{2g}}$), the ligand bandwidth W(O-$2p$), the on-site Coulomb interaction U and the crystal field splitting $10Dq$ are summarized in table 3.2. U is a second order perturbation of the spectral lineshape and was dropped in the calculations when not necessary.

Fig. 3.17(e-h) shows the calculated spectra for both the ambient and high pressure phases. For MnO, CoO and FeO the calculations in the highest pressure phases yield a LS ground state. Yet, the high spin state multiplet stays energetically close the ground state LS multiplet. An intermediate regime is therefore expected where both HS and LS states coexist on the same ion. Note that the increased ligand bandwidth W_{2p} is driving all the systems towards a metallic ground state. The HS-LS transition is then understood as resulting from the conjugated effects of increase of the crystal-field parameter $10Dq$ *and* a broadening of the O-($2p$) bandwidth W_{2p} together with an increasing covalent contribution from the hybridization to the ligand field at high pressures. The increase of $10Dq$, seen as the driving force toward a LS state, traces back to the atomic description of the magnetic collapse. More notable is the interplay of the ligand bandwidth together with the increased hybridization. The parallel evolution of these parameters across the magnetic collapse transition is represented in a phase diagram, Fig. 3.18. The lines mark the calculated HS-LS transition boundary for CoO for different values of V_{e_g}. NiO is included in the diagram although it does not undergo a spin state transition. The results demonstrate the dual behavior – both localized and delocalized – of the correlated d electrons at extreme

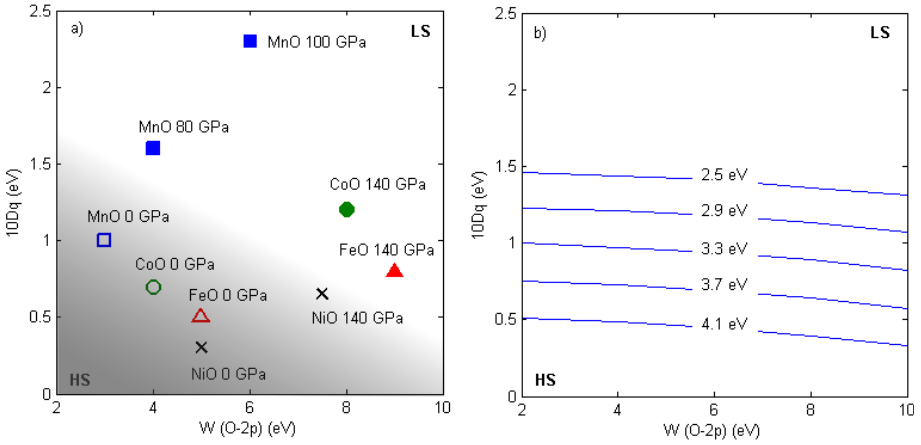

Figure 3.18: Phase diagram of the magnetic collapse in the transition-metal oxides. a) The point coordinates refer to calculated values of the crystal-field splitting $10D_q$ and ligand bandwidth $W(O-2p)$, both in the HS (open symbols) and LS (closed symbols) states, as obtained from comparison with the experimental spectra. b) Solid lines mark the calculated HS-LS transition boundary for CoO for different values of V_{e_g}.

conditions.

3.2.2 Metal-Insulator transition

3.2.2.1 NiO and CoO

NiO In an earlier study on NiO, Kao et al. [87] showed that the RIXS signal consists of two peaks, centered around 4.9 and 7.8 eV. The first feature is associated to the metal-ligand transition leading to a $d^{n+1}\underline{L}$ excited state where d^n is the metal ground state configuration, and $\underline{L}$ is a ligand hole. The energy loss to the edge of this shoulder corresponds to the charge-transfer gap in NiO. The nature of the second peak at 8.5 eV is less clear. It can be tentatively ascribed to the metal-metal transitions leading to $d^{n+1}d^{n-1}$ excited states and thus to the correlation energy U. RIXS thus provides a unique way to address the metal-insulator transition issue in strongly correlated materials.

RIXS in NiO was carried out recently under very high pressure conditions [88]. In Fig. 3.19, the RIXS spectra was obtained by tuning the incident energy the pre-peak resonance with the following two benefits: The pre-peak is associated with quadrupolar transitions (favored at large scattering angles) and the lowest-energy excited states relevant to the electronic properties of NiO are the $3d^{n+1}$ configurations. As pressure is increased, the RIXS features progressively decreases. Secondly the double structure (shoulder and peak) clearly resolved at ambient and lower pressures, smears at pressures above 50 GPa into a poorly-defined line-shape. This tendency primarily reflect the increasing bands dispersion at high pressure. In particular overlap with the ligand states increases since the lattice parameter changes by about 10% at 100 GPa. Calculations suggest that the shape of the electronic density of states does not change much with pressure but the density of states decreases uniformly and band width increases [89]. This is compatible with the behavior of the 5.3 eV peak which increases in width without appreciable change in position. It is the increase in width, or the increased dispersion which reduces the value of the charge transfer gap. The behavior of the 8.5 eV peak would suggest an initial growth of the *d-d* Coulomb interaction with pressure. Though this is unexpected since screening increases with pressure, it seems to be limited to the lower pressure regime. Finally the observed

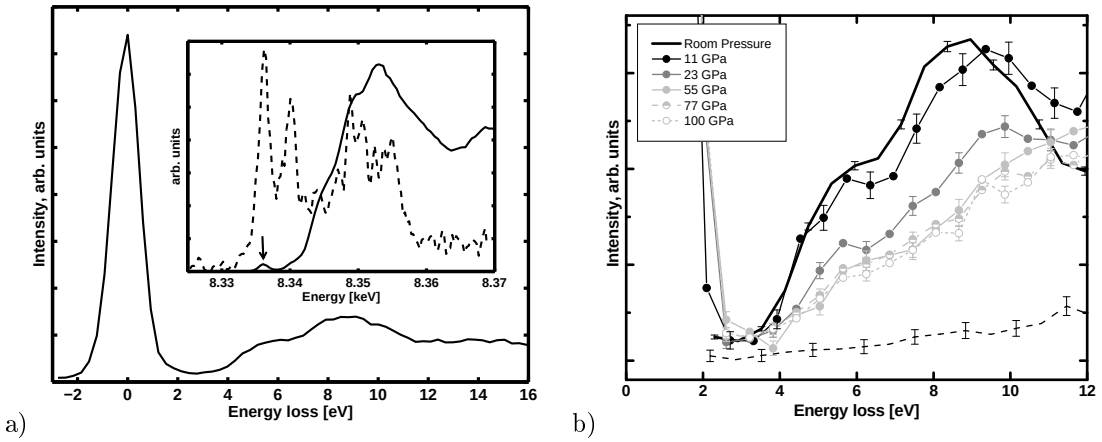

Figure 3.19: a) RIXS in NiO at ambient pressure ; the incident energy is tuned to the quadrupolar pre-peak in the absorption spectrum (arrow in inset). b) Dependence of the RIXS spectra as a function of pressure ; the dashed line is the non-resonant background (from Shukla et al. [88]).

trends suggest that a metal-insulator transition would happen mainly due to the closing of the charge-transfer gap as predicted by theory in NiO [90] (in addition to band-broadening and crystal-field effects) and in other charge-transfer insulators at lower pressures [91].

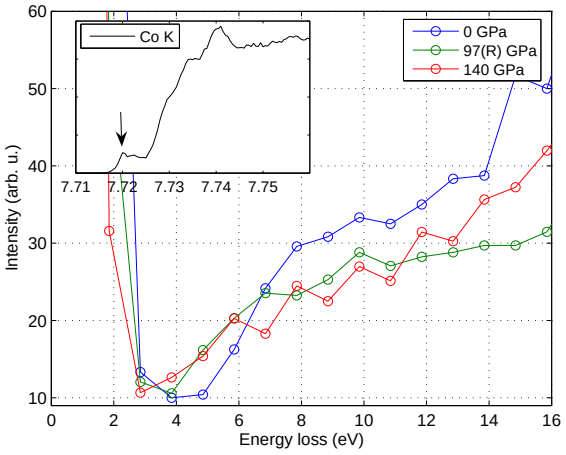

Figure 3.20: RIXS in CoO as a function of pressure ; the incident energy is tuned to the quadrupolar pre-peak in the absorption spectrum (arrow in inset). (R) indicates pressure release.

CoO The CoO insulating gap is supposedly intermediate between Mott-Hubbard and charge-transfer type. The RIXS spectra obtained in CoO under pressure is illustrated in Fig. 3.20. The incident energy was tuned to the pre-edge region in the absorption spectra (shown in inset). In the ambient pressure spectrum, a sharp increase is observed around 6 eV energy loss, characteristic of the insulating gap. No other RIXS features show up at higher energy contrary to NiO. Following the interpretation of the RIXS spectra in the latter, this could indicate that U and Δ are of similar magnitude in CoO, in agreement with Shen et al. [92]. The spectral features are smeared out upon pressure increase, while the gap region is filled. The tendency points to a metal-insulator transition which could occur in the megabar range. The pressure estimate of the gap closure is consistent with magnetic collapse pressure which is deduced from XES.

Note that, in these experiment, NiO and CoO powder were loaded in pressure cell without transmitting medium. Powder alone is to preserve hydrostaticity, though sizable pressure-gradient are expected in the megabar range. A better setup would consist of using single-crystals loaded with gaseous He which is hydrostatic up to several 100 GPa.

3.3 Delocalization of f electrons

Sample	P (GPa)	Structure	Properties	$\bar{v}$	(Refs.)
Ce	0	fcc	(PM)M	3.03	[93]
	20	fcc	(NM)M	3.2	
Gd	0	hcp	(PM)M	7	[94]
	110	hcp	(NM)M	7+δ	
SmS	0	NaCl	(NM)SC	2	[95]
	20	NaCl	(AF)†M	3	
TmTe	0	NaCl	(AF)SC	2	[96]
	4	NaCl	(FM)M	2.5	
	10	Tetragonal	(AF)I	2.8	
Yb	0	fcc	(NM)M	2	[97]
	20	bcc	(PM)M	2.55	
	60	hcp	(PM)M	2.7*	
$YbAl_2$	0	$MgCu_2$	(NM)M	2.3	[98]
	40	$MgCu_2$	(NM)M	2.9	
YbS	0	NaCl	(NM)SC	2.35	[99]
	40	NaCl	(NM)M	2.6	
UPd_2Al_3	0	P6/mmm	(AF)M	4-δ	[100]
	40	Cmmm	(NM)M	4	
UPd_3	0	dhcp	(AF)M	4	[100]
	40	dhcp	(-) M	4	

Table 3.3: Summary of main properties of the studied transition rare earth and actinide samples under pressure. $\bar{v}$ is the mean valence of the f ion determined from RXES.
(* extrapolated)
(† undefined)

3.3.1 $2p3d$-RXES

Because of their mainly localized-like character, f electron states are clearly identifiable in spectroscopic data as obtained by x-ray photoemission (XPS) or x-ray absorption (XAS) [101, 102]. They are thus the two probes that have contributed most to unraveling the electronic properties of f-electron materials in the past. At stake is the ability to quantify the f hybridization with the conduction electron which characterizes the mixed-valent systems, Kondo regime or heavy fermion state.

As pointed out in section 1.3.1, hybridization can be introduced by a superposition in the ground state of degenerated $|f^n\rangle$ configurations. The degeneracy is lifted in the

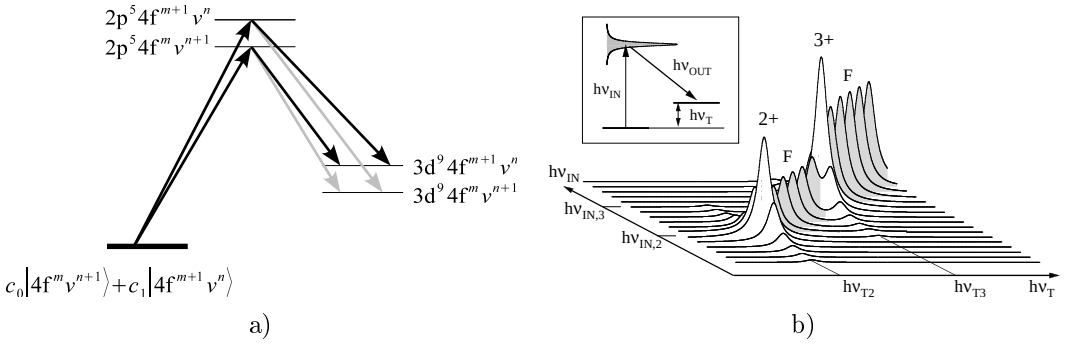

Figure 3.21: (a) $2p3d$-RXES process in a model mixed-valent rare-earth represented by the superposition of two valent states ; v stands for the valence electrons. Gray arrows indicate less probable transitions. (b) Illustration of the $2p3d$-RXES in a mixed-valent ions in the incident energy ($\hbar\nu_{IN}$) vs. transfer energy($\hbar\nu_T$) plane; F indicates the fluorescence contribution (from Dallera et al. [98]).

XPS or XAS final state, as the core-hole is screened differently by the various f states. Well separated features, each assigned to a different f valency then indicate that there is more than just a single component. This allows an estimation of the various f-electron weights, and therefore help to characterize the degree of hybridization of the f-electron. Alternatively, resonant inelastic x-ray scattering has emerged as a powerful means of probing the mixed-valent behavior in bulk materials in considerable details (cf. Table 3.3). Of particular interest is the $2p3d$-RXES process as explained in Fig. 3.21 in the case of a mixed valent $|4f^m\rangle + |4f^{m+1}\rangle$ ion. It consists of measuring the $L\alpha_{1,2}$ emission ($3d \rightarrow 2p$) in resonant conditions at the $L_{2,3}$ edges ($2p \rightarrow 5d$). As in first order spectroscopies, the different f-states, supposedly mixed in the ground state, are split in the RXES final states. By tuning the incident energy to particular intermediate states (here in presence of $2p$ core hole), one of the multiple f-states can be specifically enhanced through the resonance. The gain in resolution and intensity of selective spectral features improves the accuracy of the data reduction, and helps the comparison with theoretical calculations.

$2p3d$-RXES can be utilized to extract the rare earth valency and to follow its evolution as a function of some external parameters. Weighting the various valent states imply the ability to resolve each contribution. In such a case, the accuracy of the data analysis is considerably improved thanks to the resonant enhancement that RIXS provides. The average valent state ($\bar{v}$) can be derived from Eq. 3.3 in a two-configuration mixing f^n and f^{n+1}.

$$\bar{v} = n + \frac{I(n+1)}{I(n+1) + I(n)} \tag{3.3}$$

where $I(n)$ ($I(n+1)$) represents the integrated intensity of the n ($n+1$) spectral features. These intensities can be estimated either from the PFY spectra or the resonant emission spectra combined with standard fitting routines. Dallera et al. [103] first proposed $2p3d$-RXES technique to study $YbAgCu_4$ and $YbInCu_4$ compounds. A similar procedure was later applied to other mixed valent systems under pressure. Details about the data analysis can be found in these cited works.

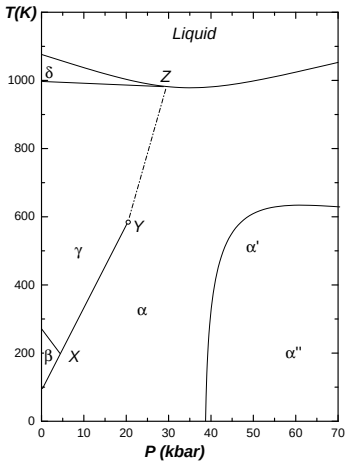

Figure 3.22: Phase diagram in elemental Ce (from Eliashberg and Capellmann [104]).

3.3.2 Kondo behavior and mixed valency in rare earth

3.3.2.1 Ce γ-α

The γ-α transition in Ce is archetypical of Kondo phenomenon encountered in f-electron systems. This isostructural phase transition accompanied by a large volume contraction that ends in a tricritical point is a manifestation of subtle interactions between f-levels self-consistently embedded in a sea of conduction electrons. As such, it is instructive to recall briefly the various theories put forward to explain the γ-α transition in Ce. The promotional model [105] first considered an integer valence change with the transition of one $4f$ electron into the conduction band. This model was soon ruled out by melting-point and cohesive energy arguments by Johansson [106], predicting that the $4f$ electrons undergo a Mott transition from localized in the γ phase to weakly itinerant in the α phase (f-band model). In the following years, the Kondo lattice model [107, 108] (Kondo volume collapse, KVC) has envisaged the disappearance of Ce magnetism in the α phase by an extremely high Kondo coupling. The KVC model differs from Johansson's scenario essentially by the active role played by the conduction electrons which hybridized with the f states.

We discuss in the following applications of $2p3d$-RXES to Ce solid-solutions (chemical pressure) [109, 110] and elemental Ce under pressure across the transition. The γ-α is normally triggered by applying external pressure, but the transition may also be tracked as a function of temperature by using chemical pressure (cf. Fig. 3.22). In this case, the formation of the parasitic β-phase is normally avoided and sample handling is simplified but alloying effects with the doping element cannot be excluded.

Ce(Sc,Th) RXES was applied to Ce solid solutions ($Ce_{0.93}Sc_{0.07}$, $Ce_{0.90}Th_{0.10}$, and $Ce_{0.80}Th_{0.20}$) which exhibit a comparable γ-α transition, driven by temperature, in presence of chemical pressure. The resonant $L\alpha_{1,2}$ lines were obtained at the Ce L_3 edge in the three compounds. The changes across the γ-α transition are barely visible in the Ce L_3 XAS spectra measured in the total fluorescence-yield mode in one of the compounds ($Ce_{0.90}Th_{0.10}$) (cf. inset to Fig. 3.23(a)). The intense whiteline at 5728.8 eV and the very weak feature at $\approx$ 5736 eV are respectively ascribed to the mainly $\underline{2p}4f^1$ and $\underline{2p}4f^0$ components. The $\underline{2p}4f^2$ configuration which is expected below the white line is not visible in the Ce L_3 XAS spectra but was observed by PFY-XAS [110] in Sc-doped Ce.

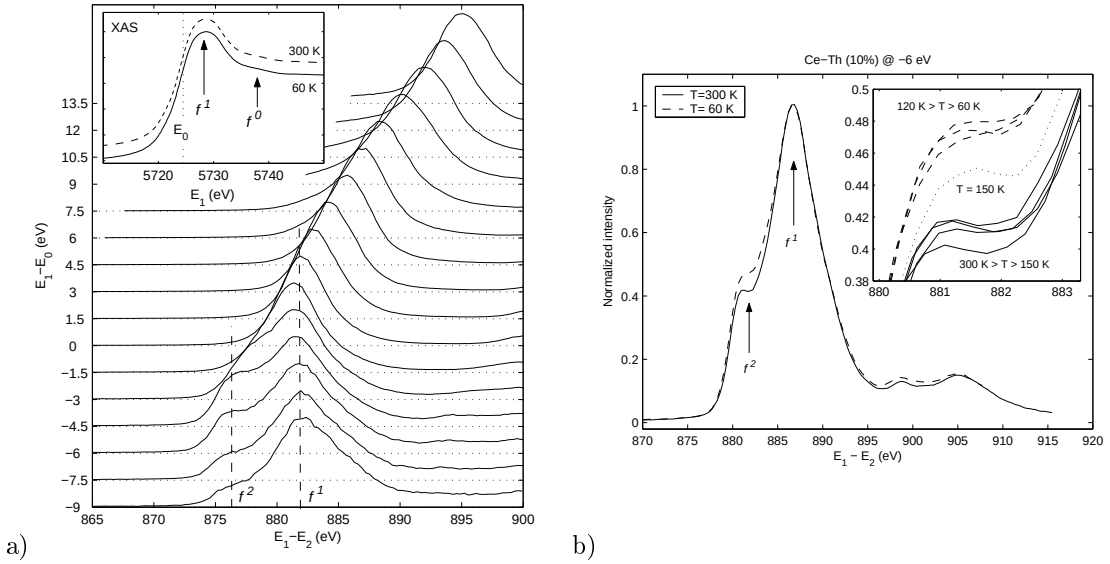

Figure 3.23: (a) Ce-2p3d RXES spectra for $Ce_{0.90}Th_{0.10}$ at 60 K as a function of the transfer energy; inset shows the XAS spectra at 60 K and 300 K. (b) Variation of the spectrum measured at the f^2 resonance while changing the temperature through the transition (from Rueff et al. [109]).

Lα_1-RXES spectra for $Ce_{0.90}Th_{0.10}$ measured at 60 K are shown in Fig. 3.23(a) on a transfer energy scale. In the Raman regime ($E_1 - E_2 < E_{edge}$), the spectra consist of a well-resolved double structure peaking at 876.1 eV and 881.9 eV transfer energies—each component corresponding to an identifiable final state—while a single feature dominates in the fluorescence regime ($E_1 - E_2 > E_{edge}$). The 881.9 eV peak resonates in the whiteline region and is assigned to the $\underline{3d}4f^15d^{n+1}$ final state. The peak at 876.1 eV has its maximum intensity for excitations well below the whiteline and corresponds to the well screened $\underline{3d}4f^25d^n$ final state. The extra stability compared to the f^2 configuration results from the strong intrashell Coulomb interaction U_{ff}.

The resonance enhancement due to the RIXS process allows one to derive the variation of the f^1/f^2 ratio with temperature as it is cycled through the transition. Fig. 3.23(b) illustrates the temperature dependence of the normalized RIXS spectra in $Ce_{0.90}Th_{0.10}$ measured at fixed incident energy. The f^2 shoulder shows a marked relative increase in intensity when the temperature is lowered below the transition. McMahan et al. [14] predict that the weight of doubly occupied states increases at the expense of single occupancy when the system goes from γ to α: At the γ-α transition, the Ce–Ce interatomic distance dramatically shrinks, which strengthens the f itinerant character through hybridization. The RIXS data confirms this tendency. However, electron interactions with the dopant element (Sc or Th) likely intervenes in the Ce-4f electronic properties. Such a perturbation of the f-states has been observed, for instance, in the Sc-doped Kondo system $YbAl_2$ by XPS [111].

Ce Thanks to the combination of perforated diamonds and the bulk sensitivity of RIXS, it has been possible to investigate directly the γ-α in elemental Ce under pressure [93]. Without the alloying effects inherent to chemical substitution, the Anderson impurity model can be correctly applied. From there, one can derive the ground state f-counts in both γ and α phases and more particularly the variation of n_f and double occupancy across the transition. Figure 3.24(a) shows the experimental L_3 XAS spectra as a function of pressure. The white line exhibits a marked decrease in intensity as Ce is driven through

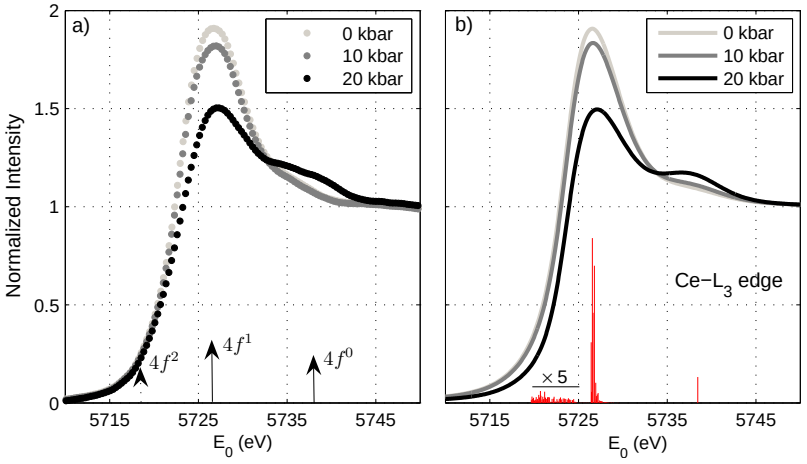

Figure 3.24: Experimental (a) and calculated (b) L_3 XAS spectra in elemental Ce as a function of pressure. Ticks in panel b) are the multiplet states (shown at 0 kbar) (from Rueff et al. [93]).

the γ-α transition, while the feature denoted $4f^0$ progressively builds up at higher energy. The overall spectral shape and the spectral changes at the transition are consistent with early results by Lengeler *et al.* [112]. The $4f^2$ component is masked by the $2p_{3/2}$ core-hole lifetime. Fig. 3.25(a) illustrates the evolution of the $2p3d$-RXES spectra measured on resonance (at $E_0 = 5718.3$ eV) as pressure is increased. The spectrum at 1.5 kbar barely shows a difference with the ambient pressure data. However, a striking increase ($\approx 40\%$) in the $4f^2/4f^1$ intensity ratio is observed as the systems passes the γ-α transition pressure.

The data were analyzed by carrying out full multiplet calculations within the Anderson impurity model and a f^0,f^1 and f^2 configuration mixing. Details of the calculations in Ce can be found in Ref. [93]. The model calculations and Hamiltonian have been described in previous works [80, 113]. The XAS spectra (Fig. 3.24(b)) are well reproduced throughout the transition. The overall agreement for RIXS is equally good (Fig. 3.25(a)), except on the high energy-transfer side. The discrepancy likely results from a fluorescence-like contribution to the spectra, which is not taken into account in the calculations. The main

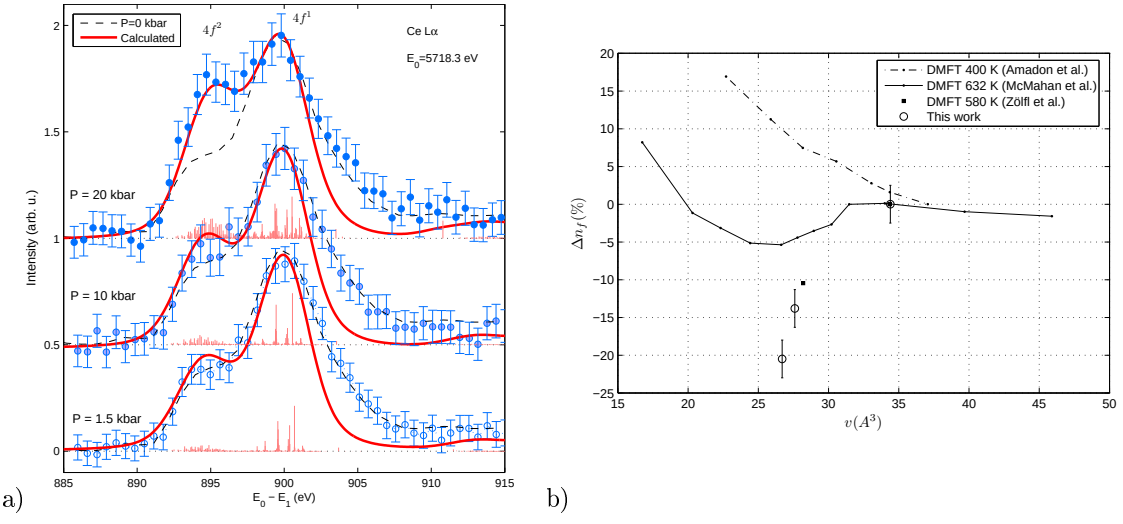

a) b)

Figure 3.25: (a) $2p3d$-RXES spectra in elemental Ce as a function of pressure ; thick lines are calculated spectra (from Rueff et al. [93]) ; (b) Calculated and experimental relative change in f-occupation number.

effect, according to the calculation, is the sharp decrease in the $4f^1$ component to the advantage of the $4f^0$-related feature, which gains intensity as Ce becomes more α-like. Such a trend is consistent with the spectral changes in the XAS spectra. Formally, the transfer of spectral weight from the $4f^1(5d^1)$ configuration toward a more $4f^0(5d^2)$ configuration in the α-phase can be understood as a partial delocalization of the $4f$ electrons. Interestingly enough, the highly hybridized $4f^2$ state also shows a sizable ($\sim$40%) increase with pressure. The expanding contribution of the doubly-occupied state at high pressure stresses the reinforcement of the interaction between the $4f$ and the conduction electrons in the α-phase, a characteristic feature of Kondo-like behavior. This growth of the double occupancy at low volume has another important consequence: it points to less correlation in the α-phase as electron hopping is favored. Therefore, the picture that arises from the RIXS analysis at the γ-α transition is that of the coexistence of competing effects: partial delocalization of the $4f$ electrons through band formation with the conduction states on the one hand, and reduced electron-electron correlations on the other hand that allows the system to accommodate stronger on-site repulsion.

Finally, the change in n_f can be obtained from the calculated weights of the $4f$-components (cf. Fig. 3.25(b)). The results are consistent with earlier estimations [110, 114, 115] for the γ-phase, but not for the α-phase where the RXES values differ substantially; n_f-value is found 10–15% lower. These new values of the f-occupation can be compared to recent *ab initio* calculations using dynamical mean-field theory (DMFT). The discontinuous dependence of n_f at the transition is well accounted for by DMFT [14, 116] in the low temperature limit. On the other hand, the drop in n_f at the transition is largely underestimated (4–10% in the DMFT calculations against $\approx$ 20% according to the RIXS results).

n_f deviates from unity in Ce as a direct consequence of non-zero hybridization. A remarkable manifestation of this Kondo behavior is the occurrence of a quasiparticle resonance at E_F in the single-particle spectral function $\rho_f(\omega)$. According to the Friedel sum rule, $\rho_f(E_F)$ depends only on the ground state value of n_f, the degeneracy N_f of the local orbital, and a coupling parameter $\Delta \propto V^2/W$, and varies as $n_f(1-n_f)$. The sharp decrease of n_f in the α-phase indicates a strong enhancement of the quasiparticle peak and that of the renormalization of the bare particle corresponding to $(1-n_f)$. But the former effect is partly smeared out at temperatures comparable to the Kondo temperature T_K [14]. T_K is here the key quantity to characterize the $4f$-electron coupling with the Fermi sea. It can be evaluated thanks to the Friedel sum rule and given the approximate relationship $(1-n_f)/n_f \sim (\pi k_B T_K)/(N_f \Delta)$ [7] in the limit of large N_f. The derived values of T_K were 70 K in the γ-phase and 1700 K in the α-phase assuming $\Delta \sim 110$ meV. The temperatures show a fair agreement with neutron scattering data [117] obtained in Ce-Sc alloys but differ very significantly from the generally accepted XPS-derived values [115]. They are consistently smaller by a factor ~ 2 in the α-phase. The RIXS results demonstrates that the full characterization of the hybridized f-state necessitates an access to the bulk properties.

3.3.2.2 Gd

Maddox et al. [94] have studied the f-delocalization in Gd under high pressure using $2p3d$-RXES. Similarly to Ce, Gd undergoes a volume collapse ($\Delta V/V \sim 5\%$) around 59 GPa . Fig. 3.26(a) shows resonant spectra taken at 18 GPa. The spectra consist of dipolar (B and B^*) and quadrupolar (A) excited states. At high pressure, an additional feature C grows on the low energy side of A which is interpreted as the signature of the increased valency. The data was interpreted assuming a $c_1 \left|4f^6v^4\right\rangle + c_2 \left|4f^7v^3\right\rangle + c_3 \left|4f^8v^2\right\rangle$ mixed

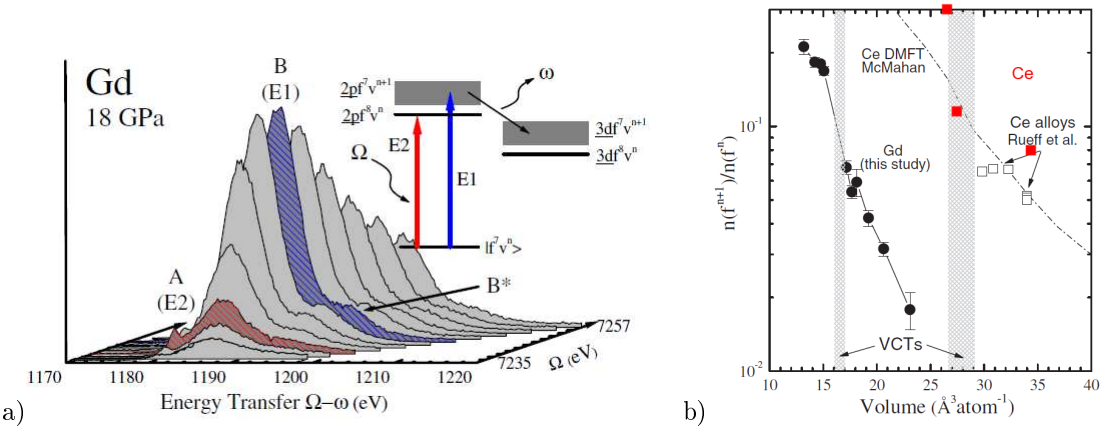

Figure 3.26: $2p3d$-RXES in Gd as at high pressure; b) experimental and calculated f^{n+1}/f^n ratio as a function a pressure (from Maddox et al. [94]). Results of Ce are added (solid squares).

ground state. Feature B and C are attributed to $\underline{2p}4f^7v^4$ and $\underline{2p}4f^8v^3$ respectively. The progress of 4f delocalization was estimated by f^8/f^7 spectral ratio. The results are shown in Fig. 3.26(b) which also display results from Ce-Sc and Ce under pressure.

The smaller f^8/f^7 ratio compared to Ce at the same volume is consistent with the more localized f electron in Gd since the f shell is more tightly bound in the heavier lanthanides due to the ever-increasing but incompletely screened nuclear charge. The continuous decay in Gd as a function of pressure suggests a Kondo-like aspect of the delocalization of the f electron in fair agreement with DMFT predictions (in the Ce case). Interestingly enough, the volume instability in Gd falls approximatively within the same f^{n+1}/f^n region as in Ce where a low volume Kondo-state is favored.

3.3.2.3 Yb compounds

Yb Like Ce, metallic Yb is characterized by a tendency to form an intermediate valence ground state. At ambient condition, Yb is divalent with an almost filled $4f$ shell, a configuration reminiscent of the quasi empty f states in Ce at the opposite end of the rare earth series. Thus, f holes in Yb are expected to play a role similar to that of the f electrons in Ce. In contrast to Ce though, Yb undergoes two consecutive structural transitions: at 4 GPa from fcc to bcc phases and at 30 GPa where it transforms to the hcp phase. Furthermore, if f electron delocalization are favored in Ce under pressure, pressure is to suppress valency fluctuation in Yb and leads the Yb ions towards a localized trivalent state.

The Yb L_3 XAS spectra were measured as a function of pressure in the PFY mode at the Yb Lα_1 line (Fig. 3.27(a)) [97]. With increasing pressure, spectral weight is transfered from the edge region to a new peak B at ∼10 eV higher energy. An additional peak A is also observed in the mid energy region, which progressively shifts to higher energy. The spectral line shape is understood as the superposition of two replicas of the d density of states, shifted in energy and weighted by the proportion of Yb^{2+} and Yb^{3+} in the ground state. The two extreme features correspond to the $\underline{2p}4f^{14}v^2$ and $\underline{2p}4f^{13}v^3$ final states split by the Coulomb interaction. The transfer of spectral weight as P increases reflects the enhancement of the Yb^{3+} contribution at high pressure, in accordance with early XAS measurements [118]. More precisely, Fig. 3.27(b) portrays the evolution of the Yb mean valence $\bar{v}$ derived from Eq. 3.3 as a function of pressure. Similar results are obtained by decomposition of the $2p3d$-RXES spectra (not shown) measured in the pre-edge region. The steep jump at low pressure is indicative of the structural transition at 4 GPa. At

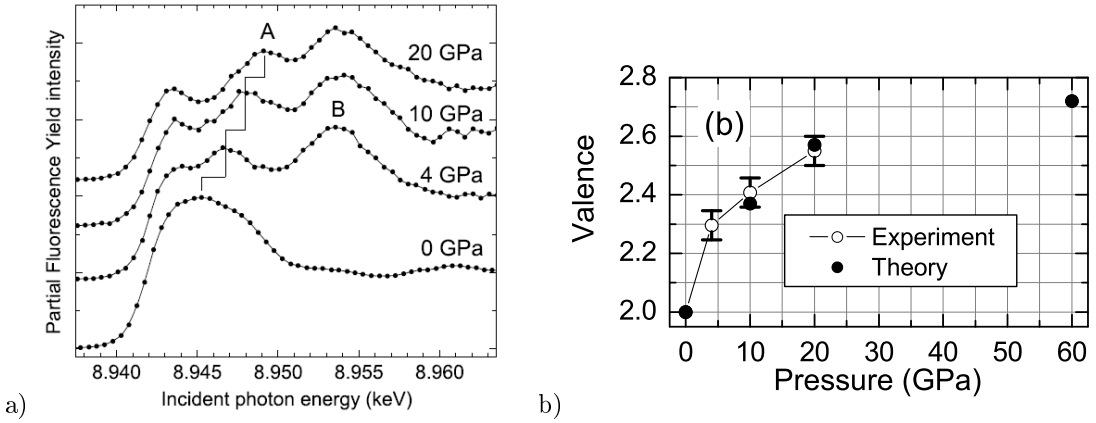

Figure 3.27: (a) PFY absorption spectra in elemental Yb as a function of pressure; (b) Calculated and experimental values of the Yb valence. (from Dallera et al. [97]).

higher pressure, $\bar{v}$ progressively increases until it reaches ∼2.55 at 20 GPa, the maximum pressure obtained during the experiment.

Because feature A is sharp and well separated, one is tempted to associate it to the formation of localized f states. Both variation of PFY-XAS spectral line shape and Yb valency as a function of pressure are in fact well accounted for by ab-initio calculations, including dynamical screening of the core-hole. Details of the calculations can be found in Refs. [97, 119]. Within this scheme, the feature A is attributed to modifications of the d conduction band states at high pressure in presence of the $2p$ core hole. The computed valency, reported in Fig. 3.27(b), shows a remarkable agreement with the experimental values. An extra pressure point was simulated at 60 GPa, yielding a valency of 2.72. This value is significantly lower than previous estimation of Syassen et al. [118] indicating that Yb is almost trivalent at 30 GPa. The structural change toward the hcp phase of higher coordination number in this pressure region might explain the sudden increase of the Yb valency above 30 GPa as determined experimentally in the earlier work [118].

$YbAl_2$, YbS Contrary to pure Yb, $YbAl_2$ and YbS both exhibit signatures of non-integer valence at ambient conditions. In $YbAl_2$, the magnetic susceptibility and specific heat indicates a moderate renormalization, while a strong valence fluctuation and a correspondingly large Kondo temperature T_K=2000 K is inferred from inelastic neutron scattering [120]. The T-dependence of the Yb valence in $YbAl_2$ has been estimated by a variety of bulk techniques such as thermodynamic measurements, magnetic susceptibility, and thermal expansion, as well as by spectroscopic probes including PES and inverse photoemission. Yet, these results are far from being consistent. Furthermore, pressure-dependent studies are limited, although valence change could be probed on a larger scale: A 0.2 valence increase was deduced from standard XAS in Yb solid solutions, using chemical pressure via Ca and Sc substitution [121].

The RIXS spectra were obtained in $YbAl_2$ and YbS under high pressure [98, 99]. The pressure dependence of the Lα_1 PFY-XAS spectra in $YbAl_2$ is shown on Fig. 3.28(b). The ambient pressure spectrum is characterized by two well-separated features that are assigned to Yb^{2+} and Yb^{3+} components in the final state. The latter gains in intensity as pressure is increased, indicating the valence increase. Fig. 3.29 illustrates this evolution in $YbAl_2$. Results obtained in Yb and YbS are shown for comparison purpose. The simple lineshape of the PFY-XAS spectra compared to Yb allows a direct estimation of the Yb valence from

regular fitting procedure. The Yb valency is found to grow from ∼2.2 to 2.9 over 40 GPa pressure increase, as deduced from the PFY data. Consistent results are obtained using the RXES spectra (cf. Fig. 3.28(a)).

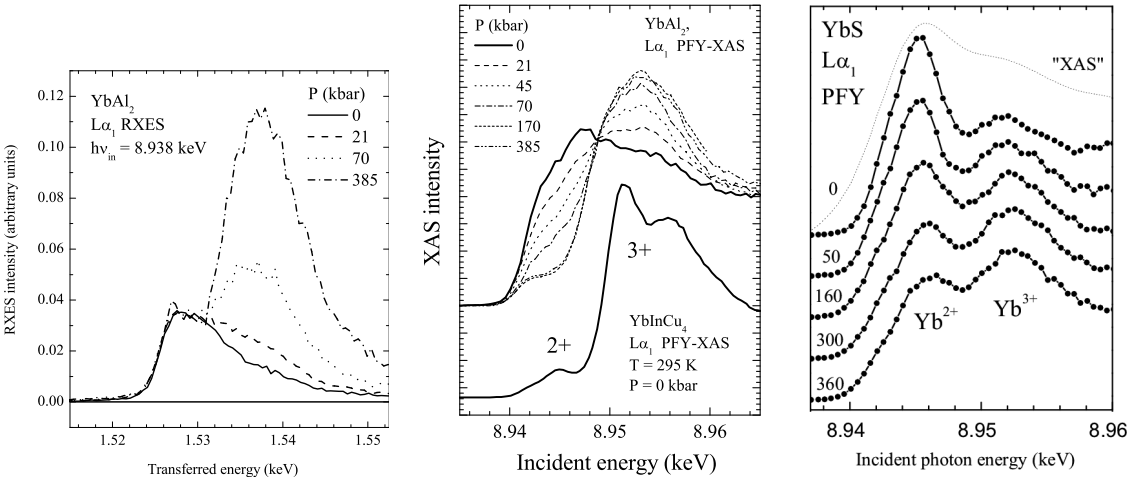

Figure 3.28: (a) $2p3d$-RXES in $YbAl_2$ measured at fixed incident energy set in the pre-edge region; (b) and (c) PFY-XAS spectra in $YbAl_2$ and YbS as a function of pressure (from Dallera et al. [98] and Annese et al. [99]).

Fig. 3.28(c) displays the PFY spectra measured in YbS as a function of pressure. In contrast to $YbAl_2$ where two similar lineshapes for the 2+ and 3+ PFY component were used, the fitting procedure in YbS takes into account quadrupolar excited states observed in the pre-edge region (see the kink around 8.942 keV in Fig. 3.28(c)). This excitation involves $2p \rightarrow 4f$ transitions in the intermediate states, which is only realized for Yb^{3+} since Yb^{2+} has a full $4f$ shell. The nature and position in energy of the quadrupolar peak was confirmed by multiplet calculations. Interestingly enough, quadrupolar features are not visible in Yb (and $YbAl_2$) even in the high pressure regime where the weight of trivalent Yb supposedly dominates the mixed-valent states. As discussed below, the difference between Yb metal and Yb sulphide provides insight into the f electron localization. This opposite behavior is also reflected in the variation of the Yb valence with pressure in YbS as indicated in Fig. 3.29: $\bar{v}$ slowly increases with pressure from 2.3 at 0 GPa up to 2.6 at 38 GPa, contrasting with the steeper increase in Yb and $YbAl_2$.

Strange et al. [122] have estimated the rare-earth valency in the metallic phase and in sulphides from first principle local spin density (LSD) calculations including self interaction correction (SIC). In the SIC-LSD approach, f electrons can be treated both as localized (where they experience a potential corrected from self-interaction) and band electrons (moving in a mean field potential) that are found only in trivalent systems. The merit of this approach is to allow for non-integer f occupancy in contrast to other theoretical frameworks [123]. In the SIC-LSD picture, the *effective valency* n_{eff} (i.e. the number of non-f valence electrons) results from the hybridization of the f band-state and the broad conduction band. The stability of either nominal divalent or trivalent configurations results from a trade-off between the localization energy and the energy gained by hybridization. SIC-LSD calculations were more specifically applied to a series of Yb compounds [124] and pressure induced valence transition in Yb based materials [125]. SIC-LSD predicts that Yb and YbS are strongly divalent ($n_{eff} = 2$ at T=0 K), as the trivalent excited state is

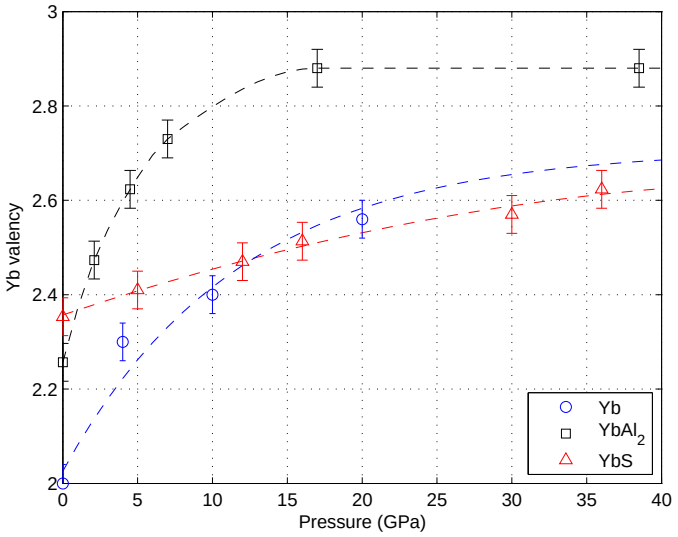

Figure 3.29: Summary of the Yb valency as a function of pressure from Refs. [97–99]; dashed lines are guide to the eyes.

located far above in energy. On the other hand, $YbAl_2$ is supposed to be weakly trivalent ($n_{eff} = 2.46$).

The RIXS-extracted valency (at $P = 0$) is coherent with this picture in Yb, while the experimental n_{eff} is slightly underestimated in $YbAl_2$ compared to theory. A discrepancy which may be ascribed to temperature effects as the divalent state is expected to contribute more at finite T. Calculations in YbS can be more difficult to reconcile with the RIXS experimental value which shows a stark departure from divalency (note that indirect estimate of the Yb valency in YbS by diffraction [126] did conclude to a divalent state at low pressure). The predicted stability of the divalent state in the sulfide presumably rules out temperature effects. On the other hand, YbS is a semiconductor, contrasting with the metallic character of Yb and $YbAl_2$, which is less accurately described by the SIC-LSD approach, and more appropriate methods, such as DMFT [127], should be envisaged. YbS differs also by the sluggish variation of the valence state as a function of pressure. In divalent YbS, the two electrons provided by the rare earth ion fill the S-3p band whereas they occupy the s-d band in Yb. When going to the more trivalent state, the f hybridized band state is pulled closer to the Fermi energy while the s-d electronic structure is more or less unchanged contrary to the metallic materials. This indicates that f electrons in Yb-sulphide are less affected by bonding, and significantly less sensitive to the lattice compression at high pressure compared to Yb. No structural change has indeed been reported in YbS even though the compressibility shows a small anomaly around 15–20 GPa. In the light of the RXES results, the anomaly cannot be attributed to a 2+ to 3+ valence transition as first proposed [128] or the onset of valence instability [126] but has to be related to the gap closure and metallization.

3.3.2.4 TmTe

TmTe a divalent semiconductor at ambient conditions, was proposed to become mixed-valent metallic under pressure greater than 2 GPa [129]. In TmTe, these valence instabilities give rise to a Kondo-like behavior in the resistivity at low temperature and a strong ferromagnetic state [130] under pressure. A previous compressibility study suggested that

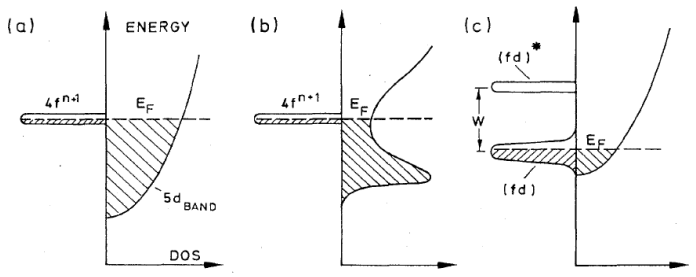

Figure 3.30: Models of intermediate valence states in sulphides (from Syassen et al. [126]).

TmTe departs from divalency at 2 GPa to reach full trivalency at 6 GPa [131].

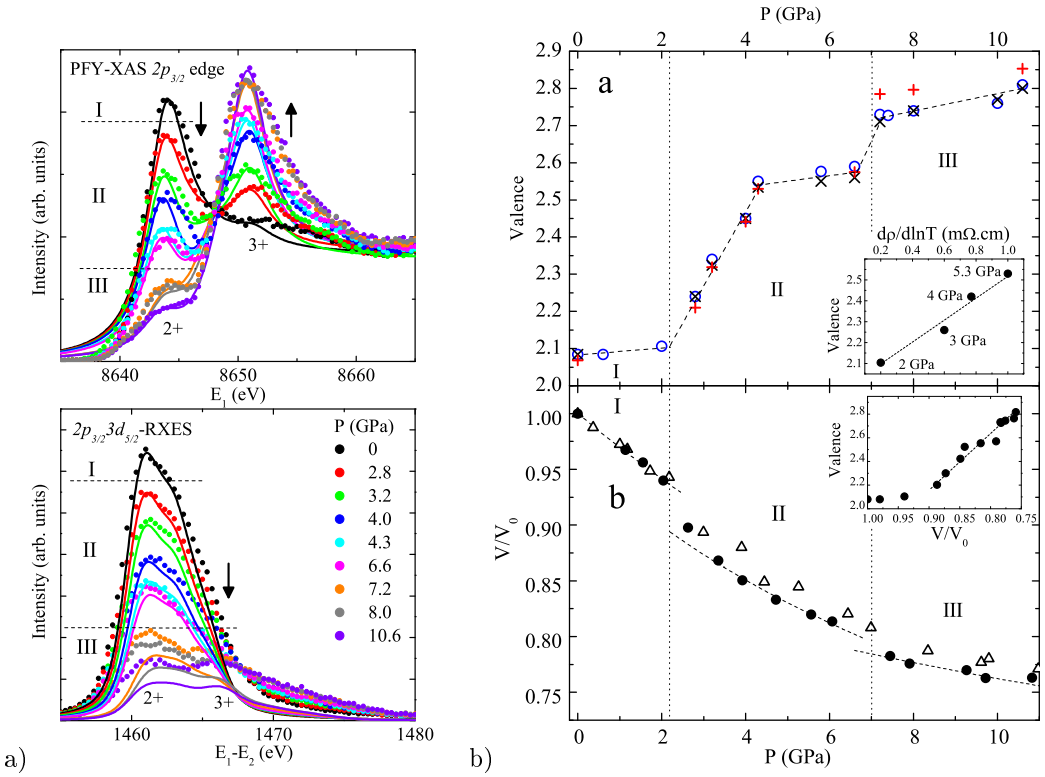

Figure 3.31: (a) (top) PFY-XAS spectra measured for TmTe at the Tm L_3-edge at pressures up to 10.6 GPa; (bottom) RXES spectra measured at the 2+ resonance (solid circles); solid lines are multiplet calculations; (b) (top) Pressure dependence of the Tm valency in TmTe as obtained by PFY-XAS (circles) and RXES (crosses) and calculations (full squares); (bottom) Relative volume change in TmTe from x-ray diffraction (from Jarrige et al. [132]).

The Tm valence was studied by $2p3d$-RXES under high pressure [96, 132] in parallel, with high-pressure x-ray diffraction. Figure 3.31(a) summarizes the spectroscopic results in TmTe under high-pressure. The pressure-dependence of the Tm valence was estimated by fitting independently the PFY and RXES spectra using a phenomenological approach similar to that described by Dallera et al. [98] (cf. Fig. 3.31(b)). Tm remains mostly divalent over the 0–2 GPa range (region I) until full closure of the semiconducting gap, in agreement with Matsumura et al. [129]. In the metallic regime above 2 GPa, the valence rapidly increases up to ∼2.5 at 4.3 GPa where the lattice volume suddenly drops (region II). Above 4.3 GPa the valence increases at a slower pace while the volume shows normal

compressibility behavior. Finally, the structural transition from the NaCl-type cubic to the high-pressure phase around 7 GPa (region II to III) coincides with the sudden valence increase from 2.52 to 2.70. The Tm valence saturates ∼2.8 at 10.6 GPa, contrasting with the 2+ to 3+ transition suggested over the 2-6 GPa range in the previous compressibility study. A strong hysteretic behavior is observed upon pressure release. The NaCl-like structure is recovered at ∼4.6 GPa.

The abrupt valence changes observed around 2 and 6 GPa at the I-II and II-III phase boundaries has implications in terms of magnetic state. Neutron diffraction [130] indicates that the antiferromagnetic state (AF) of type II formed below 0.5 K at ambient pressure transforms into a ferromagnetic (FM) state at 2.7 GPa below 14 K. When further increasing the pressure, the ordered magnetic moment decreases up to 5.3 GPa, and at 6 GPa an AFI-type state is formed below 2.55 K [133]. The FM order was suggested to result from a competition between a double-exchange interaction and a RKKY coupling.

3.3.2.5 SmS

The mixed valent state in SmS is a consequence of the interplay between charge, lattice, and magnetic degrees of freedom, considered as its strongest in this material. At ambient pressure, SmS is a semiconductor which crystallizes in the NaCl structure (black phase) with a divalent non-magnetic configuration ($4f^6$). At 0.65 GPa and room temperature, it undergoes a first-order isostructural phase transition to a metallic state (gold phase), marked by a significant contraction of the unit cell (cf. Fig. 3.32(a)). In the high pressure phase, the Sm ion is supposedly in an intermediate valence state. In contrast to the room temperature behavior, the semi-conducting state persists at T=0 K up to P_Δ=2 GPa, where the sample ultimately becomes metallic. It is expected that, near P_Δ or at still higher pressure, a magnetic quantum critical point will be reached when the Sm ion approaches its trivalent state. The transition toward a magnetic ground state at 2 GPa was confirmed by nuclear forward scattering (NFS) experiments performed at low temperature [134]. A value of 0.5 μ_B was estimated for the Sm magnetic moment, which points to a trivalent state. Magnetism was found stable up to 19 GPa.

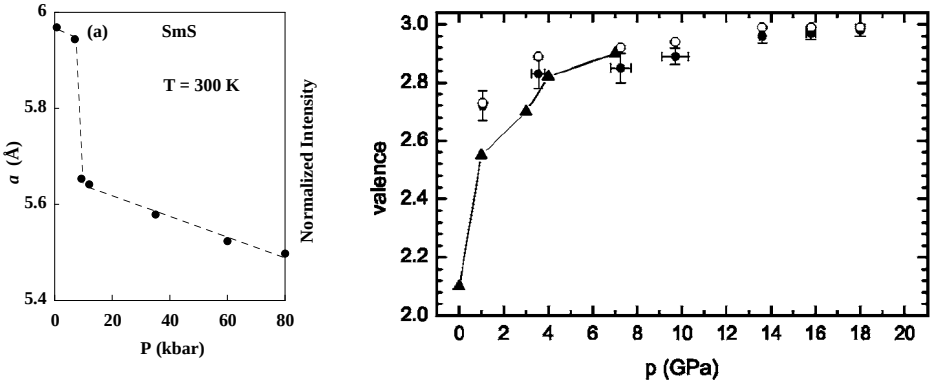

Figure 3.32: (a) Pressure variation of the lattice parameter a of SmS at T=300 K (from Raymond et al. [135]); (b) Variation of the Sm valence in SmS obtained by RIXS (circles) (from Annese et al. [95]) and standard x-ray absorption (triangles) borrowed from Ref. [136].

The pressure dependence of the Sm valency was studied by Annese et al. [95] using $2p3d$-RXES from 3 to 18 GPa at room temperature. Experimental details are given in the cited work. The results (Fig. 3.32(b)) compare well with early estimations obtained

by XAS at the Sm L_3 edge [136] that are extended here to much higher pressure. RXES indicates that the onset of long-range magnetic order at P_Δ is not correlated with transition to the full trivalent state ($P_c \sim 13$ GPa), but occurs beforehand at a valence $\bar{v}$=2.8. On the other hand, NFS data from Barla et al. [134] do not show any anomaly around P_c. In fact, barely no change in the magnetic properties is observed from 2 to 19 GPa. It seems therefore that the Sm $4f$ electrons behave magnetically like a completely trivalent ion well before the pressure P_c for the transition to the pure trivalent state is reached.

3.3.3 Actinides

3.3.3.1 U heavy fermions

In the U-compounds, U normally exists in two valencies with nominal U^{3+} ($5f^3$) and U^{4+} ($5f^2$) ionic configurations. The exact valency is in fact poorly characterized. Magnetic measurements are unable to distinguish between these two valent states because they share a similar paramagnetic moment. Furthermore, hybridization of the $5f$ electron with the conduction electrons, hence the possibility of a non-integer $5f$ occupancy, cannot be omitted. An idea supported by the Ce structure in the α phase reminiscent of the U structure [137].

As explained hereafter, the extension of $2p3d$-RXES to actinides provides an alternative way for determining the U valency and following its evolution with pressure. Delocalization of $5f$ was investigated in a series of model U-compounds submitted to high pressure conditions.

UPd_3,UPd_2Al_3 UPd_3 is a clear-cut example of a well defined $5f^2$ state. Divalency is confirmed by neutron spectroscopy via the measurement of crystal field excitations [138] and photoemission [139]. Pressure-induced delocalization toward a $5f^1$ state at 25 GPa was predicted by Petit et al. [140] using self-interaction corrected local spin density (SIC-LSD). However no corresponding effect of volume collapse was observed experimentally up to 53 GPa by x-ray diffraction under pressure [141]. UPd_2Al_3 is an antiferromagnetic superconductor (T_N=14 K, T_c= 2K), characteristic of the interplay between magnetism and superconductivity and of a moderate heavy fermion character. Contrary to UPd_3, UPd_2Al_3 undergoes a structural phase transition around 23.5 GPa. The doubling of the compressibility was interpreted by a valence change [142] induced by the partial delocalization of the f electrons [143]. The dual nature of $5f$ electron is supposedly illustrated by the behavior at ambient conditions of another U-compound, UPt_3, a heavy fermion superconductor (T_c=0.5 K). The unconventional character of UPt_3 is considered to be partly related to the coupling between localized f^2 state and delocalized f electrons [144] which are found at the Fermi energy [145].

Figure 3.33 illustrates the PFY x-ray absorption spectra at the U-L_3 edge in UPd_3 and UPd_2Al_3 as a function of pressure [100]. The UPd_3 spectra show well defined peaks (A, C and D in the figure) in the edge region but no f-related features in the pre-edge region contrary to the rare earth compounds. As pressure increases, the structures C gains in intensity while the high energy features D and D' seemingly split in energy. Simultaneously, a shoulder A' appears on the low energy side of the white line that gradually becomes asymetric. The evolution of the U-L_3 edge in UPd_2Al_3 as a function of pressure (Fig. 3.33(b)) strongly differs from UPd_3. The spectra barely vary up to 20 GPa except for the progressive increase of a second feature which appears as a shoulder to the white line (A') along with a slight energy-shift of the white line itself A and of the high energy

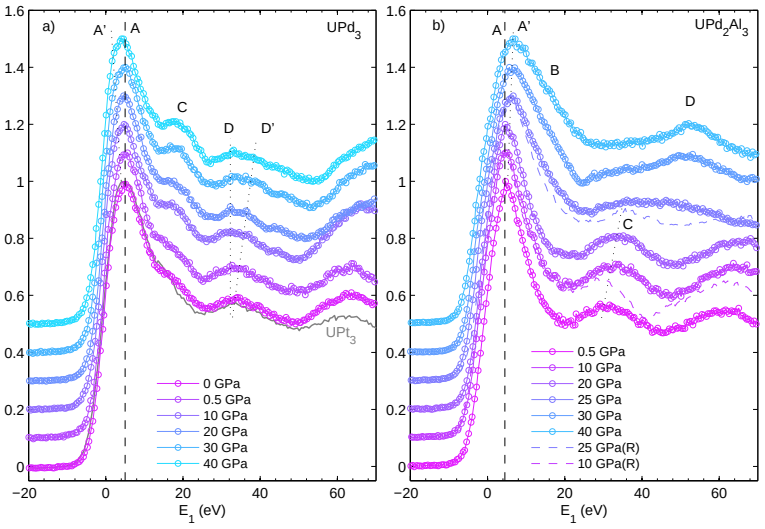

Figure 3.33: PFY-XAS spectra in UPd_3 (a) and UPd_2Al_3 (b) as a function of pressure (open circles). Ambient PFY-XAS spectrum of UPt_3 is shown (black line) for comparison purpose (from Rueff et al. [100]).

oscillations C. The white line suddenly broadens above the structural transition while the high energy oscillating pattern reduces to a single peak (D).

The data have been analyzed by *ab-initio* calculations of the U L_3 edges within the linear muffin tin orbital (LMTO) method in the LDA+U approximation. In UPd_3, this method was shown to gives a pertinent solution with two localized f electrons [146], while the $5f$ level in UPt_3 are found partly delocalized in agreement with the XPS results. The LMTO

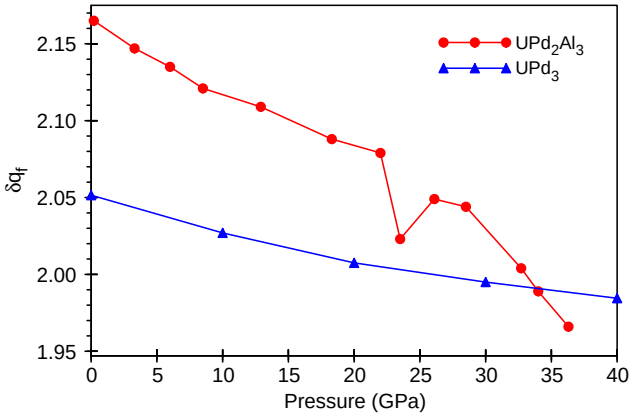

Figure 3.34: Calculated occupation number in UPd_2Al_3 and UPd_3 as a function of pressure (from Rueff et al. [100]).

cannot reproduce the exact lineshape of the absorption spectra but yields a reasonable estimation of the $5f$ occupancy number (cf. Fig. 3.34). This quantity is calculated from the difference δq between the f electron density inside the U atomic sphere (q_f^U) and that inside of a Th sphere (q_f^{Th}) which is substituted to a U atom. The correction serves at excluding the contribution from the Pd and Al states with f symmetry inside the U atomic sphere.

In UPd_3 the occupation of the U $5f$ shell averaged over two inequivalent U sites monotonously decreases from 2.05 at ambient pressure to 1.98 at 40 GPa. In the whole

pressure range δq_f remains very close to 2 which suggests that the valence state of U ions does not change under lattice compression. Thus, the picture that emerges is that of a localized f^2 configuration, consistent with the diffraction data of Heathman et al. [141] and former band calculations by Ito et al. [139]. It definitely rules out the prediction of a f^2 to f^1 transition under pressure reported in Ref. [140].

In UPd_2Al_3, δq_f=2.17 at ambient pressure indicates that the U ion is in an intermediate valence state. δq_f then gradually decreases with pressure with a somewhat higher rate above the structural transition. Comparing the UPd_2Al_3 data to the $\delta q_f(0)$=2.05 for UPd_3, for which the U $5f^2$ configuration is well established, one can suppose that the structural transition at 23.5 GPa is related to the change of the valence state of a U ion from an intermediate $U^{(4-\delta)+}$ valency to U^{4+}. This semi-qualitative analysis does not allow to answer the question whether the U valency in the high pressure phase remains integer or becomes $U^{(4+\delta)+}$. It nevertheless agrees with the current understanding of the U valence in UPd_2Al_3 which is described by a coexistence of localized and delocalized f electrons. The mixed valent state already formed at ambient pressure deviates from the preceding assumption of 2 localized and 1 delocalized f electrons [147].

Chapter 4

Summary and perspectives

Under pressure, d and f-electron materials show behaviors far more complex that what would be expected from a simplistic band picture of electron delocalization. These spectroscopic studies have revealed unusual phenomena in the electronic degrees of freedom, brought up by the increased density, the changes in the charge-carrier concentration, the overlapping between orbitals, and hybridization under high pressure conditions. Thanks to its superior penetration depth, chemical selectivity and resonant enhancement, resonant inelastic x-ray scattering has appeared extremely well suited to high pressure physics in strongly correlated materials.

4.1 Phonons

To restrict our purpose, we have focused intentionally in this manuscript on resonant processes which involve the creation of electron-hole pairs. To a large extent the results point to a strong coupling of the electronic degrees of freedom with the lattice. In the d- and f-electron systems, this gives rise for instance to volume collapse transitions. Probing such structural instabilities is possible directly by non-resonant inelastic x-ray scattering. In the non-resonant mode, IXS gives an access to the dynamical structure factor while offering the same advantages as the resonant part in terms of bulk sensitivity thanks to the high energy x-ray and small spot size. Hence, with the help of ultra high resolution nrIXS setups ($\Delta E/E \sim 10^{-}7$), the phonon branches can be measured under high pressure conditions without the constraints on the sample size inherent to neutron scattering.

4.1.1 SmS

To illustrate phonon scattering under high pressure, we show in Fig. 4.1 nrIXS results obtained in SmS up to 80 kbar [135] at the European Synchrotron Radiation Facility (ESRF). Ultra high resolution (here 2.7 meV at 17.794 keV) is achieved by working in extreme backscattering geometry both for the monochromator and the analyzer crystals then operated at high orders of reflexion. We have already discussed in section 3.3.2.5 the Sm valence change through the volume collapse transition. The nrIXS measurements reveal an additional softening of the longitudinal acoustic modes which propagate along the [111] direction. The overall behavior of the LA[111] modes is better seen in the pressure variation of the mode Grüneisen parameter $\gamma_q = -\partial \log(\omega_q)/\partial \log(V)$ displayed in the upper panel of Fig. 4.1.

The softening spans a wide q up to the zone boundary as SmS becomes metallic. The largest softening occurs at the zone boundary and stays stable up to the highest measured

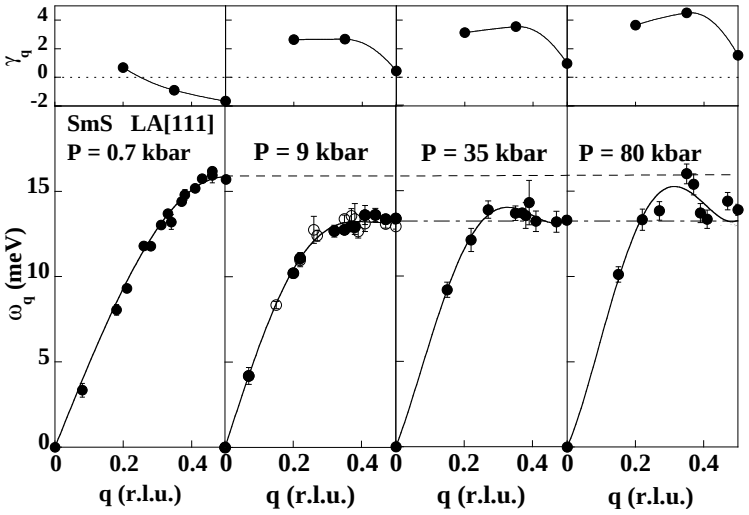

Figure 4.1: (Bottom panel) Dispersion relation ω_q for the LA [111] branch of SmS at T=300 K under pressure measured by non resonant inelastic x-ray scattering; (Upper panel) q-dependence of the mode Grüneisen parameter γ_q (from Raymond et al. [135].)

pressure of 80 kbar while a gradual hardening of the low q modes simultaneously appears. The phonon frequency increase can be related to the unusual strong pressure dependence of the bulk modulus of SmS in the metallic phase. On the other hand, the large softening at the zone boundary is suggested to be provoked by an increased density of states at the Fermi level under pressure, similarly to YS. In SmS, the latter effects occurs in parallel to (or in cooperation with) the progressive valence change at high pressure.

4.2 Temperature/pressure setups

Experimentally, the current priority is to be able to apply high-pressure while varying simultaneously temperature. At one extreme, combined high-temperature and high-pressure are mandatory to describe the electronic and magnetic properties of materials of geophysical interest, and obtain the correct magnetic or structural phase. High temperature at high pressure can be reached by associating online laser heating to diamond anvil cells. At the other extreme, low temperature allows one to explore the rich phenomena related to quantum criticality in heavy fermions.

4.2.1 Quantum critical points

The discovery of non-conventional superconductivity close to a quantum critical point (QCP) and the deviation from Fermi liquid behavior are among the challenging features observed in heavy fermions. A generalized phase diagram around the QCP is illustrated in Fig. 4.2 as a function of a non-thermal control parameter P. The latter has no univocal meaning but in the present context can be associated to pressure. In this framework, one can derive three relevant pressures which characterize the f magnetism and hybridized state following the definitions of Flouquet [6]: P_{KL} denotes the onset of itinerant magnetism, P_c (the critical pressure) marks the disappearance of long range magnetism and the onset of the Fermi liquid behavior, while at higher pressure P_v indicates the regime where the angular momentum J is quenched by the Kondo coupling. Note for example that in Ce, both P_{KL} and P_c are supposed to be negative. At low temperature, the system

undergoes a transition from a classically ordered state to a quantum disordered phase where the electrons behaves as a Fermi liquid below a characteristic temperature T^*. The two regions are separated by the QCP, a singularity marking the divergence at P_c of the quantum coherence length. It is believed that a novel ordered phase is reached as the systems approach P_c. Above this region, non Fermi-liquid behavior prevails [148].

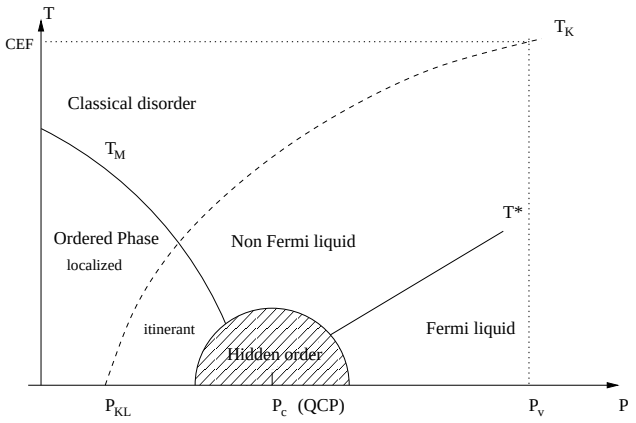

Figure 4.2: Phase diagram around a quantum critical point.

Hints of quantum critically was found in many heavy fermion compounds. In particular, it seems that the vicinity of a QCP is fundamental for superconductivity to arise in Ce and U compounds. This includes recently the discovery of superconductivity under pressure well within the AFM ($CeIn_3$ [149]) and FM magnetic (UGe_2 [150]) phase domain.

Exploring the QCP phase diagram requires combined high-pressure and low-temperature measurements. Using a light Cu-Be anvil cell mounted in a cryostat, it was recently possible to cool the sample down to 30 K at 14.4 GPa [151] in the course of an XES experiment on $La_{1-x}Sr_xCoO_3$ compounds. Improvements of such a setup would imply the external control of pressure to be varied on a fine mesh and a high stability of sample temperature. Such an accuracy is necessary to explore in details the phase diagram. Although temperatures of few K are beyond reach in current pressure setups for spectroscopic studies, the influence of the QCP is expected to encompass a wide region of the phase-space which could be investigated using the foreseen setups.

4.2.2 Online laser heating

Double sided laser heating technique enables a homogeneous and constant temperature over the illuminated sample area during data acquisition. The technique was first developed for high pressure x-ray diffraction and later adapted to x-ray emission spectroscopy [152]. The ESRF setup [153] has been recently utilized to measure the Fe Kβ emission line at 1400 K in the γ PM phase of elemental Fe. The stability of the laser spot which coincides exactly with the x-ray beam at the sample and is positioned at the focal point of the pyrometer, is necessary for long acquisition time. Preliminary results in high-pressure high temperature Fe indicate a reduction of the magnetic moment in the paramagnetic state. Such experiments could be facilitated in the future by using x-ray spectrometers of wider solid angle.

4.3 Theory

Finally, from the theoretical point of view, the parameterized multiplet approach has shown its limits and insufficiencies for the description of the strongly correlated state, although it remains one of the most efficient calculating methods for spectroscopy. One step toward an improved scheme is to implement realistic density of states, computed from first principles, in a cluster model. Such a method has a found perfect testing ground in $1s2p$-RXES thanks to the wealth of information it provides, e.g. in cuprates [154]. Alternatively, new ab-initio theoretical frameworks, such as dynamical mean field theory, has proven to be extremely useful for describing the Kondo state of f-electrons [155, 156]. These calculations can well reproduce quantities such as the XPS spectral function, and hope is that it could equally well describe second order processes including RIXS.

Glossaire

Spectroscopy

EELS : Electron Energy Loss Spectroscopy

EXAFS : Extended X-ray Absorption Fine Structure

HE-XPS : High-Energy x-ray photoemission

IXS : Inelastic X-ray Scattering

NFS : Nuclear Forward Scattering

nrIXS : non-resonant Inelastic X-ray Scattering

PFY : Partial Fluorescence Yield

RIXS : Resonant Inelastic X-ray Scattering

RXES : Resonant X-ray Emission Spectroscopy

TFY : Total Fluorescence Yield

XES : X-ray Emission Spectroscopy

XAS : X-ray Absorption Spectroscopy

XPS : X-ray Photoemission Spectroscopy

XRD : X-ray Diffraction

XRS : X-ray Raman Scattering

Theory

AIM : Anderson Impurity Model

DMFT : Dynamical Mean Field Theory

LDA : Local Density Approximation

LMTO : Linear Muffin Tin Orbital

LSD : Local spin density

SIC : Self Interaction Correction

Magnetism

AF : Antiferromagnetic

FM : Ferromagnetic

PM : Paramagnetic

HS : High Spin

IS : Intermediate Spin

LS : Low Spin

Bibliography

[1] J. Zaanen, G. Sawatzky, and J. Allen, *Band gaps and electronic structure of transition metal compounds*, Phys. Rev. Lett. **55**, 418 (1985).

[2] M. Imada, A. Fujimori, and Y. Tokura, *Metal-Insulator transitions*, Rev. Mod. Phys. **70**, 1039 (1998).

[3] N. Mott, *Metal-Insulator Transition*, Rev. Mod. Phys. **40**, 677 (1968).

[4] A. McMahan, C. Huscroft, R. Scalettar, and E. Pollock, *Volume-collapse transitions in the rare earth metals*, J. Comput.-Aided Mater. Des. **5**, 131 (1998).

[5] B. Johansson and A. Rosengren, *Pressure dependence of the f level in rare-earth systems*, Phys. Rev. B **14**, 361 (1976).

[6] J. Flouquet, *On the Heavy Fermion Road*, vol. 15 of *Progress in Low Temperature Physics* (Elsevier, 2005), chapter 2 and references therein.

[7] O. Gunnarsson and K. Schönhammer, *Electron spectroscopies for Ce compounds in the impurity model*, Phys. Rev. B **28**, 4315 (1983).

[8] A. Kotani, *Theory of resonant X-ray emission spectra in strongly correlated electron systems*, J. Electron Spectrosc. Relat. Phenom. **110-111**, 197 (2000).

[9] C. M. Varma, *Mixed-valence compounds*, Rev. Mod. Phys. **48**, 219 (1976).

[10] J. M. Lawrence, P. S. Riseborough, and R. D. Parks, *Valence fluctuation phenomena*, Reports on Progress in Physics **1**, 1 (1981).

[11] K. Held, I. Nekrasov, N. Blümer, V. Anisimov, and D. Vollhardt, *Realistic modeling of strongly correlated electron systems: An introduction to the LDA+DMFT approach*, Int. J. Mod. Phys. B **15**, 2611 (2001).

[12] P. Fulde, *Electron correlations in molecules and solids* (Springer-Verlag, 1995).

[13] A. V. Goltsev and M. M. Abd-Elmeguid, *Origin of the pressure dependence of the Kondo temperature in Ce- and Yb-based heavy-fermion compounds*, J. Phys. Condens. Matter **17**, S813 (2005).

[14] A. K. McMahan, K. Held, and R. T. Scalettar, *Thermodynamic and spectral properties of compressed Ce calculated using a combined local-density approximation and dynamical mean-field theory*, Phys. Rev. B **67**, 075108 (2003).

[15] B. Johansson, *Nature of the 5f electrons in the actinide series*, Phys. Rev. B **11**, 2740 (1975).

[16] G. H. Lander, M. S. S. Brooks, and B. Johansson, *Orbital band magnetism in actinide intermetallics*, Phys. Rev. B **43**, 13672 (1991).

[17] J.-C. Griveau, J. Rebizant, G. H. Lander, and G. Kotliar, *Superconductivity in the Americium Metal as a Function of Pressure: Probing the Mott Transition*, Phys. Rev. Lett. **94**, 097002 (2005).

[18] C. Sparks, *Inelastic resonance emission of x rays : anomalous scattering associated with anomalous dispersion*, Phys. Rev. Lett. **33**, 262 (1974).

[19] P. Eisenberger, P. M. Platzman, and H. Winick, *Resonant x-ray Raman scattering studies using synchrotron radiation*, Phys. Rev. B **13**, 2377 (1975).

[20] W. Schülke, *Handbook on Synchrotron Radiation* (Elesvier, Netherlands, 1991), vol. 3, chap. Inelastic scattering by Electronic excitations, p. 565.

[21] T. Susuki, *X-Ray Raman Scattering Experiment. I*, J. Phys. Soc. Jpn. **22**, 1139 (1967).

[22] H. Kramers and W. Heisenberg, *Scattering of radiation by atoms*, Z. Phys. **31**, 681 (1925).

[23] L. V. Hove, *Correlations in Space and Time and Born Approximation Scattering in Systems of Interacting Particles*, Phys. Rev. **95**, 249 (1954).

[24] H. Ågren and F. Gel'mukhanov, *Kramers-Heisenberg and Weisskopf-Wigner descriptions of resonant X-ray Raman scattering*, J. Electron Spectrosc. Relat. Phenom. **110-111**, 153 (2000).

[25] H. Hayashi, R. Takeda, Y. Udagawa, T. Nakamura, H. Miyagawa, H. Shoji, S. Nanao, and N. Kawamura, *Lifetime-broadening-suppressed/free XANES spectroscopy by high-resolution resonant inelastic x-ray scattering*, Phys. Rev. B **68**, 45122 (2003).

[26] P. Eisenberger, P. Platzman, and H. Winick, *X-ray resonant Raman scattering: Observations of characteristic radiation narrower than the lifetime width*, Phys. Rev. Lett. **36**, 623 (1976).

[27] J. Tulkki and T. Åberg, *Behaviour of Raman resonance scattering across the K x-ray absorption edge*, J. Phys. B: At. Mol. Phys. **15**, L435 (1982).

[28] K. Hämäläinen, D. P. Siddons, J. B. Hastings, and L. E. Berman, *Elimination of the inner-shell lifetime broadening in x-ray absorption spectroscopy*, Phys. Rev. Lett. **67**, 2850 (1991).

[29] P. Carra, M. Fabrizio, and B. T. Thole, *High resolution x-ray resonant Raman scattering*, Phys. Rev. Lett. **74**, 3700 (1995).

[30] P. Platzman and E. Isaacs, *Resonant inelastic x-ray scattering*, Phys. Rev. B **57**, 11107 (1998).

[31] G. Döring, C. Sternemann, A. Kaprolat, A. Mattila, K. Hämäläinen, and W. Schülke, *Shake-up valence excitations in CuO by resonant inelastic x-ray scattering*, Phys. Rev. B **70**, 085115 (2004).

[32] P. Abbamonte, C. A. Burns, E. D. Isaacs, P. M. Platzman, L. L. Miller, S. W. Cheong, and M. V. Klein, *Resonant inelastic x-ray scattering from valence excitations in insulating copper-oxides*, Phys. Rev. Lett. **83**, 860 (1999).

[33] J. van den Brink and M. van Veenendaal, *Theory of indirect resonant inelastic X-ray scattering*, J. Phys. Chem. Solids **66**, 2145 (2005).

[34] E. Collart, A. Shukla, F. Gelébart, M. Morand, C. Malgrange, N. Bardou, A. Madourib, and J.-L. Pelouard, *Spherically bent analyzers for resonant inelastic X-ray scattering with intrinsic resolution below 200 meV*, J. Synchrotron Rad. **12**, 473 (2005).

[35] A. Jayaraman, *Diamond anvil cell and high-pressure physical investigations*, Rev. Mod. Phys. **55**, 66 (1983).

[36] J.-P. Rueff, A. Mattila, J. Badro, G. Vankó, and A. Shukla, *Electronic properties of transition-metal oxides under high pressure revealed by x-ray emission spectroscopy*, J. Phys. Condens. Matter **17**, S717 (2005).

[37] A. Dadashev, M. P. Pasternak, G. K. Rozenberg, and R. D. Taylor, *Application of perforated diamond anvils for very high-pressure research*, Rev. Sci. Instrum. **72**, 2633 (2001).

[38] A. Mattila, J.-P. Rueff, J. Badro, G. Vankó, and A. Shukla, *Metal-ligand interplay in strongly-correlated oxides:a parametrized phase diagram for pressure induced spin transitions*, Phys. Rev. Lett. **98**, 196404 (2007), cond-mat/0612179.

[39] J.-P. Rueff, M. Krisch, Y. Q. Cai, A. Kaprolat, M. Hanfland, M. Lorenzen, C. Masciovecchio, R. Verbeni, and F. Sette, *Magnetism and structural α-ϵ phase transition in Fe monitored by x-ray emission spectroscopy*, Phys. Rev. B **60**, 14510 (1999).

[40] J.-P. Rueff, C.-C. Kao, V. V. Struzhkin, J. Badro, J. Shu, R. J. Hemley, and H. K. Mao, *Pressure induced high-spin to low-spin transition in FeS evidenced by x-ray emission spectroscopy*, Phys. Rev. Lett. **82**, 3284 (1999).

[41] J. Badro, V. V. Struzhkin, R. Hemley, H.-K. Mao, C.-C. Kao, J.-P. Rueff, and G. Shen, *Magnetism in FeO at megabar pressures from x-ray emission spectroscopy*, Phys. Rev. Lett. **83**, 4101 (1999).

[42] J. Badro, G. Fiquet, V. V. Struzhkin, M. Somayazulu, H. K. Mao, G. Shen, and T. L. Bihan, *Nature of the high-pressure transition in Fe_2O_3 Hematite*, Phys. Rev. Lett. **89**, 205504 (2002).

[43] J.-F. Lin, V. V. Struzhkin, H. kwang Mao, R. J. Hemley, P. Chow, M. Y. Hu, and J. Li, *Magnetic transition in compressed Fe_3C from x-ray emission spectroscopy*, Phys. Rev. B **70**, 212405 (2004).

[44] J.-P. Rueff, A. Shukla, A. Kaprolat, M. Krisch, M. Lorenzen, F. Sette, , and R. Verbeni, *Magnetism of Invar alloys under pressure examined by inelastic x-ray scattering*, Phys. Rev. B **63**, 132409 (2001).

[45] J. Badro, G. Fiquet, F. Guyot, J.-P. Rueff, V. V. Struzhkin, G. Vankó, and G. Monaco, *Iron Partitioning in Earth's Mantle: Toward a Deep Lower-Mantle Discontinuity*, Science **300**, 789 (2003), published online 10.1126/science.1081311.

[46] J. F. Lin, V. V. Struzhkin, S. D. Jacobsen, M. Y. Hu, P. Chow, J. Kung, H. Liu, H.-K. Mao, and R. J. Hemley, *Spin transition of iron in magnesiowustite in the Earth's lower mantle*, Nature **436**, 377 (2005).

[47] I. Y. Kantor, L. S. Dubrovinsky, and C. A. McCammon, *Spin crossover in (Mg,Fe)O: A Mössbauer effect study with an alternative interpretation of x-ray emission spectroscopy data*, Phys. Rev. B **73**, 100101 (2006).

[48] J. Badro, J.-P. Rueff, G. Vankó, G. Monaco, G. Fiquet, and F. Guyot, *Electronic Transitions in Perovskite: Possible Nonconvecting Layers in the Lower Mantle*, Science **305**, 383 (2004).

[49] G. Vankó, J.-P. Rueff, A. Mattila, Z. Nemeth, and A. Shukla, *Temperature- and pressure-induced spin-state transitions in $LaCoO_3$*, Phys. Rev. B **73**, 024424 (2006).

[50] R. Lengsdorf, J.-P. R. G. Vankó, T. Lorenz, L. H.Tjeng, and M. M. Abd-Elmeguid, *Spin-state driven metal-insulator transition in (La,Sr)CoO_3 under high pressure*, In prep. (2007).

[51] M. d'Astuto, A. Barla, N. Kernavanois, J.-P. Rueff, F. Baudelet, R. Rüffer, L. Paolasini, and B. Couzinet, *Magnetism: A Synchrotron Radiation Approach* (Springer, 2006), chap. Magnetism under Pressure with Synchrotron Radiation, pp. 375–397.

[52] K. Tsutsumi, H. Nakamori, and K. Ichikawa, *X-ray Mn Kβ emission spectra of manganese oxides and manganates*, Phys. Rev. B **13**, 929 (1976).

[53] J. Kawai, M. Takami, and C. Satoko, *Multiplet structure in Ni Kβ x-ray fluorescence spectra of nickel compounds*, Phys. Rev. Lett. **65**, 2193 (1990).

[54] F. M. F. de Groot, A. Fontaine, C. C. Kao, and M. Krisch, *Charge transfer multiplet calculations of the Kβ x-ray emission spectra of divalent nickel compounds*, J. Phys. Condens. Matter **6**, 6875 (1994).

[55] G. Peng, X. Wang, C. R. Randall, J. A. Moore, and S. P. Cramer, *Spin selective x-ray absorption spectroscopy: Demonstration using high resolution Fe Kβ fluorescence*, Appl. Phys. Lett. **65**, 2527 (1994).

[56] X. Wang, F. M. F. de Groot, and S. P. Cramer, *Spin-polarized x-ray emission of* 3*d transition-metal ions : A comparison via Kα and Kβ detection*, Phys. Rev. B **56**, 4553 (1997).

[57] G. Vankó, T. Neisius, G. Molnar, F. Renz, S. Karpati, A. Shukla, and F. M. F. de Groot, *Probing the 3d Spin Momentum with X-ray Emission Spectroscopy: The Case of Molecular-Spin Transitions*, J. Phys. Chem. B **110**, 11647 (2006).

[58] T. Tsuchiya, R. M. Wentzcovitch, C. R. S. da Silva, and S. de Gironcoli, *Spin Transition in Magnesiowüstite in Earth's Lower Mantle*, Phys. Rev. Lett. **96**, 198501 (2006).

[59] A. E. Bocquet, T. Mizokawa, T. Saitoh, H. Namatame, and A. Fujimori, *Electronic structure of 3d transition metal compounds by analysis of the 2p core-level photoemission spectra*, Phys. Rev. B **46**, 3771 (1992).

[60] L. A. Taylor and H. K. Mao, *A high-pressure polymorph of troilite*, Science **170**, 850 (1970).

[61] Y. Fei, T. Prewitt, H.-K. Mao, and C. Bertka, *Structure and density of FeS at high pressure and high temperature and the internal structure of Mars*, Science **268**, 1892 (1995).

[62] D. Sherman, *Stability of possible Fe-FeS and Fe-FeO alloy phases at high pressure and the composition of the Earth's core*, Earth Planet. Sci. Lett. **132**, 87 (1995).

[63] R. Taylor, M. Pasternak, and R. Jeanloz, *Hysteresis in the High Pressure Transformation of Bcc- to Hcp Iron*, J. Appl. Phys. **69**, 6126 (1991).

[64] O. Mathon, F. Baudelet, J.-P. Itié, A. Polian, M. d'Astuto, J. C. Chervin, and S. Pascarelli, *Dynamics of the Magnetic and Structural alpha-epsilon Phase Transition in Iron*, Phys. Rev. Lett. **93**, 255503 (2004).

[65] M. P. Pasternak, G. K. Rozenberg, G. Y. Machvariani, O. Naanan, R. D. Taylor, and R. Jeanloz, *Breakdown of the Mott-Hubbard state in Fe_2O_3: A first order insulator-metal transition with collapse of magnetism at 50 GPa.*, Phys. Rev. Lett. **82**, 4663 (1999).

[66] J.-P. Rueff (2002), unpublished.

[67] R. Weiss, *The Origin of the "Invar" effect*, Proc. R. Soc. Lond. A **82**, 281 (1963).

[68] V. L. Moruzzi, *High-spin and low-spin states in Invar and related alloys*, Phys. Rev. B **41**, 6939 (1990).

[69] S. Odin, F. Baudelet, C. Giorgetti, E. Dartyge, J.-P. Itié, A. Polian, J.-C. Chervin, S. Pizzini, A. Fontaine, and J.-P. Kappler, *Magnetic phase transitions in $Fe_{72}Pt_{28}$ Invar compound studied by high-pressure X-ray magnetic circular dichroism and X-ray diffraction*, Europhys. Lett. **47**, 378 (1999).

[70] E. Duman, M. Acet, E. F. Wassermann, J. P. Itie, F. Baudelet, O. Mathon, and S. Pascarelli, *Magnetic Instabilities in Fe_3C Cementite Particles Observed with Fe K-Edge X-Ray Circular Dichroism under Pressure*, Phys. Rev. Lett. **94**, 075502 (2005).

[71] S. Speziale, A. Milner, V. E. Lee, S. M. Clark, M. P. Pasternak, and R. Jeanloz, *Iron spin transition in Earth's mantle*, PNAS **102**, 17918 (2005).

[72] J.-F. Lin, A. G. Gavriliuk, V. V. Struzhkin, S. D. Jacobsen, W. Sturhahn, M. Y. Hu, P. Chow, and C.-S. Yoo, *Pressure-induced electronic spin transition of iron in magnesiowustite-(Mg,Fe)O*, Phys. Rev. B **73**, 113107 (2006).

[73] M. A. Korotin, S. Y. Ezhov, I. V. Solovyev, V. I. Anisimov, D. I. Khomskii, and G. A. Sawatzky, *Intermediate-spin state and properties of $LaCoO_3$*, Phys. Rev. B **54**, 5309 (1996).

[74] C. Zobel, M. Kriener, D. Burns, J. Baier, M. Grüninger, T. Lorenz, P. Reutler, and A. Revcolevschi, *Evidence for a low-spin to intermediate-spin state in $LaCoO_3$*, Phys. Rev. B **66**, 020402(R) (2002).

[75] K. Asai, O. Yokokura, J. Tranquada, G. Shirane, and K. Kohn, *Two spin-state transitions in $LaCoO_3$*, J. Phys. Soc. Jpn. **67**, 290 (1998).

[76] T. Vogt, J. A. Hirljac, N. C. Hyatt, and P. Woodward, *Pressure-induced intermediate-to-low spin state transition in $LaCoO_3$*, Phys. Rev. B **67**, 140401 (R) (2003).

[77] R. Lengsdorf, M. Ait-Tahar, S. S. Saxena, M. Ellerby, D. I. Khomskii, H. Micklitz, T. Lorenz, and M. M. Abd-Elmeguid, *Pressure-induced insulating state in (La,Sr)CoO_3*, Phys. Rev. B **69**, 140403(R) (2004).

[78] S. Tsubouchi, T. Kyômen, M. Itoh, P. Ganguly, M. Oguni, Y. Shimojo, Y. Morii, and Y. Ishii, *Simultaneous metal-insulator and spin-state transitions in $Pr_{0.5}Ca_{0.5}CoO_3$*, Phys. Rev. B **66**, 052418 (2002).

[79] S. Hüfner, *Electronic structure of NiO and related 3d-transition-metal compounds*, Advances in Physics **43**, 183 (1994).

[80] A. Kotani and S. Shin, *Resonant inelastic x-ray scattering spectra of electrons in solids*, Rev. Mod. Phys. **73**, 203 (2001).

[81] F. M. F. de Groot, *High resolution x-ray emission and x-ray absorption spectroscopy*, Chem. Rev. **101**, 1779 (2001).

[82] J. Zaanen, C. Westra, and G. A. Sawatzky, *Determination of the electronic structure of transition-metal compounds: 2p x-ray photoemission spectroscopy of the nickel dihalides*, Phys. Rev. B **33**, 8060 (1986).

[83] T. Mizokawa, A. Fujimori, H. Namatame, K. Akeyama, and N. Kosugi, *Electronic structure of the local-singlet insulator $NaCuO_2$*, Phys. Rev. B **49**, 7193 (1994).

[84] T. A. Tyson, Q. Qian, C.-C. Kao, J.-P. Rueff, F. M. F. de Groot, M. Croft, S. W. Cheong, M. Greenblatt, and M. A. Subramanian, *Valence state of Mn in Ca-doped $LaMnO_3$ studied by high-resolution Mn Kβ emission spectroscopy*, Phys. Rev. B **60**, 4665 (1999).

[85] P. Glatzel, U. Bergmann, F. de Groot, and S. Cramer, *Influence of the core hole on the Kβ emission photoionizataion or orbital electron capture: A comparison using MnO and $^{55}Fe_2O_3$*, Phys. Rev. B **64**, 45109 (2001).

[86] P. Glatzel, U. Bergmann, J. Y. H. Visser, J. H. Robblee, W. Gu, F. M. F. de Groot, G. Christou, V. L. Pecoraro, S. P. Cramer, and V. K. Yachandra, *The Electronic Structure of Mn in Oxides, Coordination Complexes, and the Oxygen-Evolving Complex of Photosystem II Studied by Resonant Inelastic X-ray Scattering*, J. Am. Chem. Soc. **126**, 9946 (2004).

[87] C.-C. Kao, W. A. Caliebe, J. B. Hastings, and J.-M. Gillet, *X-ray resonant Raman scattering in NiO: resonant enhancement of the charge transfer excitations*, Phys. Rev. B **54**, 16361 (1996).

[88] A. Shukla, J.-P. Rueff, J. Badro, G. Vankó, A. Mattila, F. M. F. de Groot, and F. Sette, *Charge transfer at very high pressure in NiO*, Phys. Rev. B **67**, 81101 (2003).

[89] R. E. Cohen, I. I. Mazin, and D. G. Isaak, *Magnetic collapse in transition metal oxides at high pressure: Implications for the Earth*, Science **275**, 654 (1997).

[90] X.-B. Feng and N. M. Harrison, *Metal-insulator and magnetic transition of NiO at high pressures*, Phys. Rev. B **69**, 035114 (2004).

[91] P. Dufek, P. Blaha, and K. Schwarz, *Theoretical investigation of the pressure-induced metallization and the collapse of the antiferromagnetic state of NiI_2*, Phys. Rev. B **51**, 4122 (1995).

[92] Z.-X. Shen, J. W. Allen, P. A. P. Lindberg, D. S. Dessau, B. O. Wells, A. Borg, W. Ellis, J. S. Kang, S.-J. Oh, I. Lindau, et al., *Photoemission study of CoO*, Phys. Rev. B **42**, 1817 (1990).

[93] J.-P. Rueff, J.-P. Itié, M. Taguchi, C. F. Hague, J.-M. Mariot, R. Delaunay, J.-P. Kappler, and N. Jaouen, *Probing the γ-α Transition in Bulk Ce under Pressure: A Direct Investigation by Resonant Inelastic X-ray Scattering*, Phys. Rev. Lett. **96**, 237403 (2006).

[94] B. R. Maddox, A. Lazicki, C. S. Yoo, V. Iota, M. Chen, A. K. McMahan, M. Y. Hu, P. Chow, R. T. Scalettar, and W. E. Pickett, *4f Delocalization in Gd: Inelastic X-Ray Scattering at Ultrahigh Pressure*, Phys. Rev. Lett. **96**, 215701 (2006).

[95] E. Annese, A. Barla, C. Dallera, G. Lapertot, J.-P. Sanchez, and G. Vankó, *Divalent-to-trivalent transition of Sm in SmS: Implications for the high-pressure magnetically ordered state*, Phys. Rev. B **73**, 140409(R) (2006).

[96] I. Jarrige, J.-P. Rueff, S. R. Shieh, T. Matsumura, H. Ishii, N. Hiraoka, and Y. Q. Cai, *f-Level occupancy in TmTe under pressure investigated by high resolution X-ray absorption spectroscopy*, Physica B **378-380**, 1154 (2006).

[97] C. Dallera, O. Wessely, M. Colarieti-Tosti, O. Eriksson, R. Ahuja, B. Johansson, M. I. Katsnelson, E. Annese, J.-P. Rueff, G. Vankó, et al., *Understanding mixed valent materials: Effects of dynamical core-hole screening in high-pressure x-ray spectroscopy*, Phys. Rev. B **74**, 081101(R) (2006), in press.

[98] C. Dallera, E. Annese, J.-P. Rueff, A. Palenzona, G. Vankó, L. Braicovich, A. Shukla, and M. Grioni, *Determination of pressure-induced valence changes in $YbAl_2$ by resonant inelastic x-ray scattering*, Phys. Rev. B **68**, 245114 (2003).

[99] E. Annese, J.-P. Rueff, G. Vankó, M. Grioni, L. Braicovich, L. Degiorgi, R. Gusmeroli, and C. Dallera, *Valence of YbS under pressure: A resonant inelastic x-ray emission study*, Phys. Rev. B **70**, 075117 (2004).

[100] J.-P. Rueff, S. Raymond, A. Yaresko, D. Braithwaite, P. Leininger, G. Vankó, A. Huxley, J. Rebizant, and N. Sato, *Pressure-induced f-electron localization-delocalization in U-based heavy fermions*, In prep. (2007).

[101] J. Fuggle, F. Hillebrecht, J. Esteva, R. Karnatak, O. Gunnarsson, and K. Schönhammer, *f-count effects in x-ray absorption spectra of the 3d levels in Ce and its intermetallic compounds*, Phys. Rev. B **27**, 4637 (1983).

[102] J. Fuggle, F. Hillebrecht, Z. Zolnierek, R. Lässer, C. Freiburg, O. Gunnarsson, and K. Schönhammer, *Electronic structure of Ce and its intermetallic compounds*, Phys. Rev. B **27**, 7330 (1983).

[103] C. Dallera, M. Grioni, A. Shukla, G. Vankó, J. L. Sarrao, J.-P. Rueff, and D. Cox, *New Spectroscopy Solves an Old Puzzle: The Kondo Scale in Heavy Fermions*, Phys. Rev. Lett. **88**, 196403 (2002).

[104] G. Eliashberg and H. Capellmann, *On the nature of the γ-α phase transition in cerium*, JETP Lett. **67**, 125 (1998).

[105] B. Coqblin and A. Blandin, *Stability of localized magnetic moments in metals*, Adv. Phys. **17**, 261 (1968).

[106] B. Johansson, *The α-γ transition in cerium is a Mott transition*, Philos. Mag. **30**, 469 (1974).

[107] M. Lavagna, C. Lacroix, and M. Cyrot, *Volume collapse in the Kondo lattice*, Phys. Lett. **90A**, 210 (1982).

[108] J. W. Allen and R. M. Martin, *Kondo volume collapse and the γ to α transition in Cerium*, Phys. Rev. Lett. **49**, 1106 (1982).

[109] J.-P. Rueff, C. F. Hague, J.-M. Mariot, L. Journel, R. Delaunay, J.-P. Kappler, G. Schmerber, A. Derory, N. Jaouen, and G. Krill, *f-State occupancy at the γ-α phase transition in Ce-Th and Ce-Sc alloys*, Phys. Rev. Lett. **93**, 067402 (2004).

[110] C. Dallera, M. Grioni, A. Palenzona, M. Taguchi, E. Annese, G. Ghiringhelli, A. Tagliaferri, N. B. Brookes, T. Neisius, and L. Braicovich, *alpha-gamma transition in metallic Ce studied by resonant x-ray spectroscopies*, Phys. Rev. B **70**, 085112 (2004).

[111] E. Vesoco, L. Braichovich, B. D. Michelis, A. Fasana, R. Eggenhöffner, A. Iandelli, G. Olcese, and A. Palenzona, *Photoemission-spectroscopy investigation of the chemical-pressure effect in $Yb_{1-x}M_xAl_2$ (M= Ca, Sc)*, Phys. Rev. B **43**, 12281 (1991).

[112] B. Lengeler, G. Materlik, and J. Müller, *L-edge x-ray absorption spectra of γ- and α-Cerium*, Phys. Rev. B **28**, 2276 (1983).

[113] H. Ogasawara, A. Kotani, P. Le Fèvre, D. Chandesris, and H. Magnan, *3d resonant photoemission spectra at the Ce L_3 edge of $CeRh_3$*, Phys. Rev. B **62**, 7970 (2000).

[114] E. Wuilloud, H. R. Moser, W. D. Schneider, and Y. Baer, *Electronic structure of gamma- and alpha-Ce*, Phys. Rev. B **28**, 7354 (1983).

[115] L. Z. Liu, J. W. Allen, O. Gunnarsson, N. E. Christensen, and O. K. Andersen, *alpha-gamma transition in Ce: A detailed analysis of electron spectroscopy*, Phys. Rev. B **45**, 8934 (1992).

[116] M. Zölfl, I. Nekrasov, T. Pruschke, V. Anisimov, and J. Keller, *Spectral and magnetic properties of the α- and γ-Ce from dynamical mean-field theory and local density approximation*, Phys. Rev. Lett. **87**, 276403 (2001).

[117] A. Murani, Z. Bowden, A. Taylor, R. Osborn, and W. Marshall, *Evidence for localized $4f$ states in alpha-Ce*, Phys. Rev. B **48**, 13981 (1993).

[118] K. Syassen, G. Wortmann, J. Feldhaus, K. Frank, and G. Kaindl, *Mean valence of Yb metal in the pressure range 0 to 340 kbar*, Phys. Rev. B **26**, 4745 (1982).

[119] M. Colarieti-Tosti, M. I. Katsnelson, M. Mattesini, S. I. Simak, R. Ahuja, B. Johansson, C. Dallera, and O. Eriksson, *First-Principles Theory of Intermediate-Valence f-electron Systems*, Phys. Rev. Lett. **93**, 096403 (2004).

[120] O. Gunnarsson and K. Schönhammer, *The dynamic susceptibility of Ce compounds in the $1/N_f$ expansion*, J. Magn. Magn. Mater. **52**, 227 (1985).

[121] R. Eggenhöffner, M. Sancrotti, I. Abbati, E. Puppin, Z. Shen, I. Lindau, A. Iandelli, and G. Olcese, *Yb valence in $Yb_{1-x}Ca_xAl_2$ pseudobinary alloys via Yb L_{III} X-ray absorption spectroscopy*, Solid State Commun. **74**, 1009 (1990).

[122] P. Strange, A. Svane, W. M. Temmerman, Z. Szotek, and H. Winter, *Understanding the valency of rare earths from first-principles theory*, Nature **399**, 756 (1999).

[123] W. Temmerman, Z. Szotek, A. Svane, P. Strange, H. W. anad A. Delin, B. Johansson, O. Eriksson, L. Fast, and J. Wills, *Electronic configuration of Yb compounds*, Phys. Rev. Lett. **83**, 3900 (1999).

[124] A. Svane, W. M. Temmerman, Z. Szotek, L. Petit, P. Strange, and H. Winter, *Ab initio theory of valency in ytterbium compounds*, Phys. Rev. B **62**, 13394 (2000).

[125] A. Svane, P. Strange, W. Temmerman, Z. Szotek, H. Winter, and L. Petit, *Pressure induced valence transitions in rare earth chalcogenides and pnictides*, Phys. Stat. Sol. (B) **223**, 105 (2001).

[126] K. Syassen, H. Winzen, H. Zimmer, H. Tups, and J. Leger, *Optical response of YbS and YbO at high pressures and the pressure-volume relation of YbS*, Phys. Rev. B **32**, 8246 (1985).

[127] A. Georges, G. Kotliar, W. Krauth, and M. Rozenberg, *Dynamical mean-field theory of strongly correlated fermion systems and the limit of infinite dimensions*, Rev. Mod. Phys. **68**, 13 (1996).

[128] A. Jayaraman, A. K. Singh, A. Chatterjee, and S. U. Devi, *Pressure-volume relationship and pressure-induced electronic and structural transformations in Eu and Yb monochalcogenides*, Phys. Rev. B **9**, 2513 (1974).

[129] T. Matsumura, T. Kosaka, J. Tang, T. Matsumoto, H. Takahashi, N. Môri, and T. Suzuki, *Pressure Induced Semiconductor to Metal Transition in TmTe*, Phys. Rev. Lett. **78**, 1138 (1997).

[130] P. Link, I. Goncharenko, J. Mignot, T. Matsumura, and T. Susuki, *Ferromagnetic mixed-valence and Kondo-lattice state in TmTe at high pressure*, Phys. Rev. Lett. **80**, 173 (1998).

[131] J. Tang, T. Kosaka, T. Matsumura, T. Matsumoto, N. Mori, and T. Suzuki, *The valence state of TmTe at high pressure*, Solid State Comm **100**, 571 (1996).

[132] I. Jarrige, J.-P. Rueff, S. R. Shieh, M. Taguchi, Y. Ohishi, T. Matsumura, C.-P. Wang, H. Ishii, N. Hiraoka, and Y. Q. Cai, *Volume collapse transitions and f hybridization in TmTe at high pressure*, In prep. (2007).

[133] J. M. Mignot, I. N. Goncharenko, T. Matsumura, and T. Suzuki, *Stabilization of type-I antiferromagnetism in mixed-valence TmTe at P=6 GPa*, J. Magn. Magn. Mat. **226-230**, 211 (2001).

[134] A. Barla, J. P. Sanchez, Y. Haga, G. Lapertot, B. P. Doyle, O. Leupold, R. Ruffer, M. M. Abd-Elmeguid, R. Lengsdorf, and J. Flouquet, *Pressure-Induced Magnetic Order in Golden SmS*, Phys. Rev. Lett. **92**, 066401 (2004).

[135] S. Raymond, J.-P. Rueff, M. D'Astuto, D. Braithwaite, M. Krisch, and J. Flouquet, *Phonon anomalies at the valence transition of SmS: An inelastic x-ray-scattering study under pressure*, Phys. Rev. B **66**, 220301(R) (2002).

[136] J. Röhler, G. Krill, J.-P. Kappler, M. F. Ravet, and D. Wohlleben, *Valence Instabilities* (North-Holland, Amsterdam, 1982), p. 215.

[137] F. H. Ellinger and W. H. Zachariasen, *Structure of Cerium Metal at High Pressure*, Phys. Rev. Lett. **32**, 773 (1974).

[138] W. J. L. Buyers and T. M. Holden, *Handbook on the physics and chemistry of the actinides* (Elsevier, New York, 1987), p 289.

[139] T. Ito, H. Kumigashira, S. Souma, T. Takahashi, Y. Haga, Y. Tokiwa, and Y. Onuki, *Band structure of UPd_3 studied by ultrahigh-resolution angle-resolved photoemission spectroscopy*, Phys. Rev. B **66**, 245110 (2002).

[140] L. Petit, A. Svane, W. M. Temmerman, and Z. Szotek, *5f electron localization-delocalization transition from UPd_3 to UPt_3*, Phys. Rev. Lett. **88**, 216403 (2002).

[141] S. Heathman, M. Idiri, J. Rebizant, P. Boulet, P. Normile, L. Haleva, V. Sechovský, and T. L. Bihan, *UPd_3 under high pressure: Lattice properties*, Phys. Rev. B **67**, 180101 (2003).

[142] A. Krimmel, A. Loidl, K. Knorr, B. Buschinger, C. Geibel, C. Wassvilew, and M. Hanfland, *High-pressure structural study of UM_2Al_3 (M=Pd, Ni): evidence for a pressure-iduced electronic transition in UPd_2Al_3*, J. Phys. Condens. Matter **12**, 8801 (2000).

[143] G. Zwicknagl and P. Fulde, *The dual nature of $5f$ electrons and the origin of heavy fermions in U compounds*, J. Phys. Condens. Matter **15**, S1911 (2003).

[144] G. Zwicknagl, A. N. Yaresko, and P. Fulde, *Microscopic description of origin of heavy quasiparticles in UPt_3*, Phys. Rev. B **65**, 081103 (2002).

[145] J. W. Allen, *Resonant Photoemission of Solids with Strongly Correlated Electrons*, vol. 1 of *Synchrotron Radiation Research : Advances in Surface and Interface Science* (Plenum Press, New York, 1992), chap. 6, p. 253.

[146] A. N. Yaresko, V. N. Antonov, and P. Fulde, *Localized U 5f electrons in UPd_3 from LDA + U calculations*, Phys. Rev. B **67**, 155103 (2003).

[147] L. Petit, A. Svane, W. M. Temmerman, Z. Szotek, and R. Tyer, *Ab initio determination of the localized/delocalized f-manifold in UPd_2Al_3*, Europhys. Lett. **62**, 391 (2003).

[148] J. Custers, P. Gegenwart, H. Wilhelm, K. Neumaier, Y. Tokiwa, O. Trovarelli, C. Geibel, F. Steglich, C. Pepin, and P. Coleman, *The break-up of heavy electrons at a quantum critical point*, Nature **424**, 524 (2003).

[149] N. D. Mathur, F. M. Grosche, S. R. Julian, I. R. Walker, D. M. Freye, R. K. W. Haselwimmer, and G. G. Lonzarich, *Magnetically mediated superconductivity in heavy fermion compounds*, Nature **394**, 6688 (1998).

[150] S. S. Saxena, P. Agarwal, K. Ahilan, F. M. Grosche, R. K. W. Haselwimmer, M. J. Steiner, E. Pugh, I. R. Walker, S. R. Julian, P. Monthoux, et al., *Superconductivity on the border of itinerant-electron ferromagnetism in UGe_2*, Nature **406**, 587 (2000).

[151] R. Lengsdorf, Ph.D. thesis, Universität zu Köln (2005).

[152] J.-F. Lin, V. V. Struzhkin, S. D. Jacobsen, G. Shen, V. B. Prakapenka, H.-K. Mao, and R. J. Hemley, *X-ray emission spectroscopy with a laser-heated diamond anvil cell: a new experimental probe of the spin state of iron in the EarthŠs interior*, J. Synchrotron Rad. **12**, 637 (2005).

[153] E. Schultz, M. Mezouar, W. Crichton, S. Bauchau, G. Blattmann, D. Andrault, G. Fiquet, R. Boehler, N. Ramber, B. Sitaud, et al., *Double-sided laser heating system for in situ high pressureÛhigh temperature monochromatic X-ray diffraction at the ESRF*, High Pressure Research **25**, 71 (2005).

[154] A. Shukla, M. Calandra, M. Taguchi, A. Kotani, G. Vankó, and S.-W. Cheong, *Polarized resonant inelastic x-ray scattering as an ultra-fine probe of excited states in La_2CuO_4*, Phys. Rev. Lett. **96**, 077006 (2006).

[155] L. de' Medici, A. Georges, G. Kotliar, and S. Biermann, *Mott Transition and Kondo Screening in f-Electron Metals*, Phys. Rev. Lett. **95**, 066402 (2005).

[156] B. Amadon, S. Biermann, A. Georges, and F. Aryasetiawan, *The alpha-gamma Transition of Cerium Is Entropy Driven*, Phys. Rev. Lett. **96**, 066402 (2006).

List of Figures

List of Tables